The Astrophysical Journal, 923:264 (42pp), 2021 December 20 https://doi.org/10.3847/1538-4357/ac29bc

A Comparative Study of Atmospheric Chemistry with VULCAN

Shang-Min Tsai[1], Matej Malik[2], Daniel Kitzmann[3], James R. Lyons[4], Alexander Fateev[5], Elspeth Lee[6], and Kevin Heng[6]
[1] Atmospheric, Ocean, and Planetary Physics, Department of Physics, University of Oxford, UK
[2] Department of Astronomy, University of Maryland, College Park, MD 20742, USA
[3] University of Bern, Center for Space and Habitability, Switzerland
[4] Arizona State University, School of Earth and Space Exploration, Bateman Physical Sciences, Tempe, USA
[5] Technical University of Denmark, Department of Chemical and Biochemical, Denmark
[6] University of Bern, Center for Space and Habitability, Switzerland
Received 2021 May 6; revised 2021 September 13; accepted 2021 September 22; published 2021 December 28

Abstract

We present an update of the open-source photochemical kinetics code VULCAN to include C–H–N–O–S networks and photochemistry. The additional new features are advection transport, condensation, various boundary conditions, and temperature-dependent UV cross sections. First, we validate our photochemical model for hot Jupiter atmospheres by performing an intercomparison of HD 189733b models between Moses et al., Venot et al., and VULCAN, to diagnose possible sources of discrepancy. Second, we set up a model of Jupiter extending from the deep troposphere to upper stratosphere to verify the kinetics for low temperature. Our model reproduces hydrocarbons consistent with observations, and the condensation scheme successfully predicts the locations of water and ammonia ice clouds. We show that vertical advection can regulate the local ammonia distribution in the deep atmosphere. Third, we validate the model for oxidizing atmospheres by simulating Earth and find agreement with observations. Last, VULCAN is applied to four representative cases of extrasolar giant planets: WASP-33b, HD 189733b, GJ 436b, and 51 Eridani b. We look into the effects of the C/O ratio and chemistry of titanium/vanadium species for WASP-33b, we revisit HD 189733b for the effects of sulfur and carbon condensation, the effects of internal heating and vertical mixing (K_{zz}) are explored for GJ 436b, and we test updated planetary properties for 51 Eridani b with S_8 condensates. We find that sulfur can couple to carbon or nitrogen and impact other species, such as hydrogen, methane, and ammonia. The observable features of the synthetic spectra and trends in the photochemical haze precursors are discussed for each case.

Unified Astronomy Thesaurus concepts: Exoplanets (498); Hot Jupiters (753); Earth atmosphere (437); Atmospheric composition (2120); Planetary atmospheres (1244); Solar system planets (1260); Open source software (1866)

Supporting material: tar.gz file

1. Introduction

Understanding the chemical compositions has been a central aspect in the atmospheric characterization of planets within and beyond the solar system. Photochemical kinetics models establish the link between our knowledge of chemical reactions and various planetary processes (e.g., atmospheric dynamics, radiative transfer, outgassing process, etc.), which provides a theoretical basis for interpreting observations and addressing habitability.

Hot Jupiters are the first discovered and best characterized class of exoplanets. Transit and eclipse observations have made various initial detections of chemical species in their atmospheres, such as Na, K, H_2O, CH_4, CO, CO_2 (e.g., see the review of Kreidberg 2018). An extreme class of exceedingly irradiated hot Jupiters around bright stars have an equilibrium temperature higher than 2000 K. They are prime targets for emission observations, and recent high-resolution spectroscopic measurements reveal atomic and ionic features that make their atmospheres resemble low-mass stars (e.g., Birkby et al. 2013; Brogi et al. 2014; Hoeijmakers et al. 2018).

The majority of discovered exoplanets have sizes between those of Earth and Neptune. Their heavy elemental abundances (i.e., metallicity) can vary considerably, as is often inferred by the water detection (e.g., Wakeford et al. 2017; Chachan et al. 2019). While CH_4 is expected to be more abundant in cooler ($T_{eq} \lesssim 1000$ K) atmospheres, understanding how disequilibrium chemistry and other processes alter the CH_4/CO abundance ratio remains an ongoing task.

The direct imaging technique provides a complementary window to resolve young planets at a far orbit (e.g., see the reviews of Crossfield 2015; Pueyo 2018). The new generation of instruments, such as GPI and SPHERE (Chauvin 2018), have identified a number of interesting young Jupiter analogs. These young planets are self-luminous from their heat of formation and receive UV fluxes from the star at the same time, giving insights on the planet-forming conditions outside the snow lines and the transition between planets and brown dwarfs.

Across the various types of these planetary atmospheres, photochemical kinetics and atmospheric transport are the dominant mechanisms that control the major chemical abundances. Photodissociation occurs when molecules are split into reactive radicals by high-energy photons, while atmospheric transport shapes the abundance distribution. Disequilibrium processes can drive abundances considerably away from the chemical equilibrium state and are best studied in chemical kinetics models.

Kinetics models stem from simulating the atmospheric compositions in solar system planets (e.g., Kasting et al. 1979; Yung et al. 1984; Nair et al. 1994; Wilson & Atreya 2004;

Lavvas et al. 2008; Hu et al. 2012; Krasnopolsky 2012), which focus on photochemistry and radical reactions. The low-temperature regime makes thermochemistry less relevant in most cases. Liang et al. (2003) first applied a photochemical kinetics model, Caltech/JPL KINETICS (Allen et al. 1981), to the hot Jupiter HD 209458b and identified the photochemical source of water for producing atomic H. However, some reaction rates in their study are extrapolated from measurements at low temperatures and are not suitable for hot Jupiter conditions. Line et al. (2010) adopt the high-temperature rate coefficients for the major molecules and use the lower boundary to mimic mixing from the thermochemical equilibrium region. A new group of models incorporating kinetics data valid at high temperatures have since started to emerge. Zahnle et al. (2009) reverse the reactions to ensure kinetics consistent with thermodynamic calculations and consider sulfur chemistry on hot Jupiters. Moses et al. (2011) implement high-temperature reactions in KINETICS to model hot Jupiters HD 189733b and HD 209458b with detailed pathway analysis. Venot et al. (2012) adopt the combustion mechanisms validated for industrial applications to model the same canonical hot Jupiters but find different quenching and photolysis profiles from Moses et al. (2011). Hobbs et al. (2021) recently extend Zahnle et al. (2009) to include sulfur photochemistry and find that the inclusion of sulfur can impact other nonsulfur species on HD 209458b and 51 Eridani b. As the discovery of diverse exoplanets progresses, more kinetics models have been applied to study a wide range of aspects, such as the compositional diversity within an atmospheric-grid framework (Moses et al. 2013; Miguel & Kaltenegger 2014; Molaverdikhani et al. 2019), atmospheric evolution with loss and/or outgassing processes (Hu et al. 2015; Lincowski et al. 2018; Wordsworth et al. 2018), prebiotic chemistry driven by high-energy radiation (Rimmer & Helling 2016; Rimmer & Rugheimer 2019), and detectability of habitable planets (Schwieterman et al. 2018; Arney 2019).

A number of recent attempts to make atmospheric composition measurements have been hindered by aerosol layers (Kreidberg et al. 2014; Parviainen et al. 2018). Aerosol particles are possibly ubiquitous, with diverse compositions (Gao et al. 2020), including cloud particles formed from condensation or produced by photolysis at high altitudes. Microphysics models (Helling & Woitke 2006; Lavvas & Koskinen 2017; Gao & Benneke 2018; Kawashima & Ikoma 2018; Ohno et al. 2020) have investigated the trends and properties of aerosols for various environments. One particularly interesting candidate of aerosols is the sulfur family, such as sulfuric clouds (Hu et al. 2013; Misra et al. 2015; Loftus et al. 2019) in an oxidizing atmosphere or elemental sulfur in a reducing atmosphere (Hu et al. 2013; Gao et al. 2017). Photochemistry generally sets off the initial steps in the gas phase. The condensable species can then form particles when saturated in a broad range of altitudes (Gao et al. 2017). The relatively simple sulfur particles in H_2-dominated atmospheres allow a consistent photochemical-aerosol kinetics modeling, which we will conduct in this work. Although the formation pathways of organic haze particles are highly complex, we will focus on a group of haze precursors and investigate their photochemical stability in the hope of providing complementary insights on the haze-forming conditions.

The exclusive access to often proprietary chemical models motivated us to develop VULCAN, which is an open-source, chemical kinetics code (Tsai et al. 2017). The initial version of VULCAN includes a reduced-size C–H–O thermochemical network and treats eddy diffusion. In Tsai et al. (2017), VULCAN is validated by comparing the quench behavior with ARGO (Rimmer & Helling 2016) and Moses et al. (2011). Since then, VULCAN has been continuously updated and applied to several studies, such as Zilinskas et al. (2020), who identify key molecules of hot super-Earths with nitrogen-dominated atmospheres, and Shulyak et al. (2020), who explore the effects of extreme ultraviolet (XUV) for different stellar types.

In this work, we present the new version of one-dimensional photochemical model VULCAN, with embedded chemical networks now including hydrogen, oxygen, carbon, nitrogen, and sulfur. The chemical network is customizable and does not require fast and slow species to be separated. The major updates of VULCAN from Tsai et al. (2017) are as follows:

1. C–H–N–O–S chemical networks with about 100 species, including a simplified benzene-forming mechanism.
2. Photochemistry with options for temperature-dependent UV cross-section input.
3. Condensation and particle settling included.
4. Advection, eddy diffusion, and molecular diffusion included for the transport processes.
5. Choice of various boundary conditions.

In Section 2, we describe model details that have been updated since Tsai et al. (2017). In Section 3, we validate photochemistry and various new features of VULCAN with simulations of HD 189733b, Jupiter, and Earth. A comprehensive model comparison for HD 189733b between Moses et al. (2011), Venot et al. (2012), and VULCAN is given. In Section 4, we perform case studies that focus on the effects of sulfur chemistry and haze precursors. We discuss caveats, implications, and opportunities for future work in Section 5. We summarize the highlights in Section 6.

2. Kinetics Model

2.1. Basic Equations and Numerics

The one-dimensional photochemical kinetics model solves a set of Eulerian continuity equations,

$$\frac{\partial n_i}{\partial t} = \mathcal{P}_i - \mathcal{L}_i - \frac{\partial \phi_i}{\partial z}, \tag{1}$$

where n_i is the number density (cm^{-3}) of species i and t denotes the time. $\mathcal{P}_i$ and $\mathcal{L}_i$ are the production and loss rates (cm^{-3} s^{-1}) of species i, from both thermochemical and photochemical reactions. The system of Equation (1) has the same form as that in Tsai et al. (2017), except that only eddy diffusion is considered for the transport flux ϕ_i in Tsai et al. (2017). The transport flux including advection, eddy diffusion, and molecular and thermal diffusion, while assuming hydrostatic balance, is now written as (e.g., Chamberlain & Hunten 1987)

$$\phi_i = n_i\, v - K_{zz} n_{\rm tot} \frac{\partial X_i}{\partial z} - D_i \left[\frac{\partial n_i}{\partial z} + n_i \left(\frac{1}{H_i}, +, \frac{1+\alpha_T}{T}, \frac{dT}{dz} \right) \right], \tag{2}$$

where v is the vertical wind velocity; K_{zz} and D_i are the eddy diffusion and molecular diffusion coefficient, respectively; H_i is the molecular scale height for species i with molecular mass m_i, i.e., $H_i = \frac{m_i g}{k_B T}$ (g: gravity; T: temperature; k_B: the Boltzmann constant); and α_T is the thermal diffusion factor. While advection is commonly ignored in one-dimensional models, we keep the advection term and distinguish it from eddy diffusion with respect to their intrinsic differences. For example, a plume of smoke transports the initial abundance along the direction of wind until diffusion becomes important and dissipates the smoke to the surrounding air.

Physically, the first term of the transport flux (2) describes advection in the direction of the wind. The second term is an eddy diffusion that acts to smear out the compositional gradient. The molecular diffusion in the third term becomes important at low pressure and drives each constituent toward diffusive equilibrium, which is different for each species based on its individual scale height. The direction of thermal diffusion depends on the sign of the thermal diffusion factor. A positive sign means that the component will diffuse toward colder regions, and vice versa. Thermal diffusion is often a secondary effect compared to eddy diffusion or molecular diffusion, except for the light species in the thermosphere with large temperature gradients (Nicolet 1968). The molecular diffusion coefficient has the expression of b/N from the gas kinetic, where b is a parameter for binary gas mixtures. The binary parameter b and the thermal diffusion factor α_T are ideally determined experimentally for each binary mixture. In practice, we simplify the atmosphere to a binary system with the dominant gas as the main constituent and the rest of the gases as the minor constituents. Specifically, we adopt the molecular diffusion coefficient of a binary mixture that is available from the experimental data and scale that of other mixtures based on the fact that b is proportional to the mean relative speed of two gases, i.e., given D_{1-2} for the dominant gas 1 and minor gas 2, the molecular diffusion coefficient for gas 1 and any other minor gas i can be scaled as

$$D_{1-i} = D_{1-2}\sqrt{m_2/m_i((m_1+m_i)/(m_1+m_2))}. \tag{3}$$

The molecular diffusion coefficient and the thermal diffusion factor for atmospheres dominated by H_2, N_2, and CO_2 are listed in Appendix A.

A second-order central difference is used to discretize the spatial derivative of diffusion flux, as in Tsai et al. (2017), except that a first-order upwind scheme (Brasseur & Jacob 2017) is applied for advection. The finite difference form for the derivative of the transport flux of layer j is

$$\frac{\phi_{i,j+1/2} - \phi_{i,j-1/2}}{\Delta z_j}, \tag{4}$$

with the upper and lower interfaces of layer j labeled as $j+1/2$ and $j-1/2$, respectively, in the staggered structure. The full expression for the transport flux in Equation (2) at the upper and lower interfaces is then

$$\begin{aligned}
\phi_{i,j+1/2} &= \phi^{\rm adv}_{i,j+1/2} \\
&\quad - (K_{zz,j+1/2} + D_{i,j+1/2}) n_{{\rm tot},j+1/2} \\
&\quad \times \frac{X_{i,j+1} - X_{i,j}}{\Delta z_{j+1/2}} - D_{j+1/2} X_{i,j+1/2}\left(\frac{1}{H_i} - \frac{1}{H_0}\right. \\
&\quad \left. + \frac{\alpha_T}{T_{j+1/2}} \frac{T_{j+1} - T_j}{\Delta z_{j+1/2}}\right) \\
\phi_{i,j-1/2} &= \phi^{\rm adv}_{i,j-1/2} \\
&\quad - (K_{zz,j-1/2} + D_{i,j-1/2}) n_{{\rm tot},j-1/2} \\
&\quad \times \frac{X_{i,j} - X_{i,j-1}}{\Delta z_{j-1/2}} - D_{j-1/2} X_{i,j-1/2}\left(\frac{1}{H_i} - \frac{1}{H_0}\right. \\
&\quad \left. + \frac{\alpha_T}{T_{j-1/2}} \frac{T_j - T_{j-1}}{\Delta z_{j-1/2}}\right) \\
\phi^{\rm adv}_{i,j+1/2} &= \begin{cases} v_{j+1/2} n_{i,j}, & \text{for } v_{j+1/2} > 0 \\ v_{j+1/2} n_{i,j+1}, & \text{for } v_{j+1/2} < 0 \end{cases} \\
\phi^{\rm adv}_{i,j-1/2} &= \begin{cases} v_{j-1/2} n_{i,j-1}, & \text{for } v_{j-1/2} > 0 \\ v_{j-1/2} n_{i,j}, & \text{for } v_{j-1/2} < 0 \end{cases},
\end{aligned} \tag{5}$$

where H_0 is the atmospheric scale height with altitude-dependent gravity and we have approximated the physical quantities at the interface by the average of two adjacent layers $n_{{\rm tot},j\pm1/2} = \frac{n_{{\rm tot},j} + n_{{\rm tot},j\pm1}}{2}$, $X_{ij\pm1/2} = \frac{X_{i,j} + X_{i,j\pm1}}{2}$, and $T_{{\rm tot},j\pm1/2} = \frac{T_{{\rm tot},j} + T_{{\rm tot},j\pm1}}{2}$. The advection flux $\phi^{\rm adv}$ in Equation (5) only depends on the property of the upstream layer in the upwind scheme. Equation (1) can be reduced to a system of ordinary differential equations (ODEs) after replacing the spatial derivative of transport flux in Equation (1) with Equations (4) and (5) and assigning proper boundary conditions. The numerical scheme using the Rosenbrock method to integrate the "stiff" system (1) forward in time until steady state is achieved is described in detail in Tsai et al. (2017).

2.2. Boundary Conditions

The solutions to the system of ODEs derived from Equation (1) need to satisfy the given boundary conditions. The boundary conditions encompass various planetary processes that are crucial in regulating the atmosphere. Three basic quantities are commonly used to describe the boundary conditions (e.g., Hu et al. 2012): flux, velocity, and mixing ratio. We will elucidate their corresponding implications for the lower and upper boundaries.

The flux term in Equation (5) depends on the layers above and below. Hence, the fluxes at the top and bottom are unspecified. Assigning constant fluxes is common to represent surface emission at the lower boundary for rocky planets and inflow/outflow at the upper boundary. For example, CO and CH_4 surface sources play a key role to Earth's troposphere; meteoritic inflow or hydrodynamic escape outflow can be prescribed as constant flux at the upper boundary (e.g., Wordsworth et al. 2018). Alternatively, diffusion-limited flux can be assigned at the upper boundary, which assumes that the escape flux is limited by the diffusion transport into the exosphere. The diffusion-limited flux reads

$$\phi_{i,\rm top} = -D_{i,\rm top} n_i \left(\frac{1}{H_i} - \frac{1}{H_0}\right) \tag{6}$$

Table 1
Model Validation Setup

Planet	P–T Profile	Network[a]	Stellar UV	Gravity[b] ($cm^2\ s^{-1}$)	Upper Boundary	Lower Boundary
HD 189733b	Moses et al. (2011)	N–C–H–O	Eps Eri[c]	2140	H escape[d]	zero flux
Jupiter	Moses et al. (2005) + dry adiabat	N–C–H–O–lowT	Gueymard (2018)	2479	H_2O, CO, CO_2 inflow	zero flux
Earth	COSPAR	S–N–C–H–O–full	Gueymard (2018)	980	H, H_2 escape	Table 2

Notes.
[a] Files available in supplementary material.
[b] At the surface for Earth and defined at 1 bar for a gaseous planet.
[c] From the StarCat database (https://casa.colorado.edu/~ayres/StarCAT) (Ayres 2010) and following the same scaling adjustment as Moses et al. (2011).
[d] Assuming diffusion-limited escape rate.

and can be applied to any set of light species in the code. Without additional constraints, we often simply assume the flux to be zero, which means that there is no net material exchange. This zero-flux boundary condition is generally suited for the lower boundary conditions, while placed at a sufficient depth of most gas giants (Moses et al. 2011; Rimmer & Helling 2016; Tsai et al. 2017). While not specifying the boundary condition, zero flux is implied as default in VULCAN.

In addition to the flux, velocity is useful to represent sources and sinks that scale with the species abundance. For example, (dry/wet) deposition velocity is conventionally used to parameterize removal processes, such as gas absorption or uptake into the surface (Hu et al. 2012; Seinfeld & Pandis 2016). At the upper boundary, upward velocity can be assigned to account for escape velocity or for any process producing inflow/outflow (Krasnopolsky 2012). The flux and velocity can also be assigned together to describe the final boundary condition of a single species.

Constant mixing ratios are prescribed for the boundary condition when the detail exchange is complex but the knowledge of precise abundance is available. For example, water vapor at the surface is expected to be set by saturation according to relative humidity on an ocean planet with a substantial reservoir of water. Assigning constant mixing ratios is also practical for regional models, such as the composition around the cloud layers for the Venus model with lower boundary placed at the cloud layer (Krasnopolsky 2012). Since constant mixing ratio does not allow changes of the composition at the boundary, this boundary condition should not be used in conjunction with flux or velocity boundary conditions.

2.3. Chemical Networks

We have extended the previous C–H–O network in Tsai et al. (2017) to include nitrogen and sulfur in a hierarchical manner (e.g., C–H–O,[7] C–H–N–O, C–H–N–O–S networks). Each network is provided with a reduced version and a full version, where "reduced" is referred to both oxidation state and network size. The reduced version has species and mechanisms (e.g., the ozone cycle) that are only important in oxidizing conditions that are stripped off, which are more computationally efficient and suited for the general hydrogen-dominated atmospheres. The full version of networks is designed for a wide range of main atmospheric constituents, from reducing to oxidizing. Hydrocarbon species are truncated at two carbons, while some higher-order hydrocarbons are present as necessary sinks for the two-carbon species or hazy precursors. The chemical network files with rate coefficients for the forward reactions can be found at https://github.com/exoclime/VULCAN/tree/master/atm.

The full version of C–H–N–O–S network includes 96 species, H, H_2, O, ^1O, O_2, O_3, OH, H_2O, HO_2, H_2O_2, CH, C, CH_2, $^1CH_2$, CH_3, CH_4, C_2, C_2H_2, C_2H, C_2H_3, C_2H_4, C_2H_5, C_2H_6, C_4H_2, C_3H_3, C_3H_2, C_3H_4, C_6H_5, C_6H_6, C_4H_3, C_4H_5 CO, CO_2, CH_2OH, HCO, H_2CO, CH_3O, CH_3OH, CH_3CO, H_2CCO, HCCO, CH_3O_2, CH_3OOH, N, $N(^2D)$, N_2, NH, CN, HCN, NH_2, NH_3, NO, N_2H_2, N_2H, N_2H_3, N_2H_4, HNO, H_2CN, HC_3N, CH_3CN, CH_2CN, C_2H_3CN, HNCO, NO_2, N_2O, CH_2NH_2, CH_2NH, CH_3NH_2, CH_3CHO, NO_3, HNO_3, HNO_2, NCO, N_2O_5, S, S_2, S_3, S_4, S_8, SH, H_2S, HS_2, SO, SO_2, SO_3, CS, OCS, CS_2, NS, HCS, HSO, HSO_3, H_2SO_4, CH_3S, CH_3SH, and S_2O, as well as about 570 forward thermochemical reactions and 69 photodissociation branches. All of the thermochemical reactions are reversed using the equilibrium constant derived from the NASA polynomials as described in Tsai et al. (2017) to ensure that chemical equilibrium can be kinetically achieved.[8] We also provide an option for customizing modular networks. A subgroup of species can be freely picked, and only reactions that involve the selected species will form a new modular chemical network. Unlike minimizing Gibbs free energy for equilibrium chemistry, caution is required in this process to incorporate trace species that are important intermediates to set up a sensible network.

We have incorporated a simplified benzene mechanism into the generally two-carbon based kinetics, with the motivation of considering it in the context of haze precursors, as will be discussed in Section 2.8. The intention is to capture the main formation pathways at minimum cost in terms of the size of the network. We adopt one of the possible benzene-forming pathways through propargyl (C_3H_3) recombination $C_3H_3 + C_3H_3 \xrightarrow{M} C_6H_6$ (Frenklach 2002), whereas C_3H_3 is produced by

[7] We have updated the C–H–O network from Tsai et al. (2017) by adding HO_2 and H_2O_2.

[8] We report a significant discrepancy in the new NASA 9-polynomials of CH_2NH (http://garfield.chem.elte.hu/Burcat/NEWNASA.TXT) compared to the early NASA 7-polynomials and other sources, which can lead to errors of several orders of magnitude. We use the fit from the NASA 7-polynomials for CH_2NH instead.

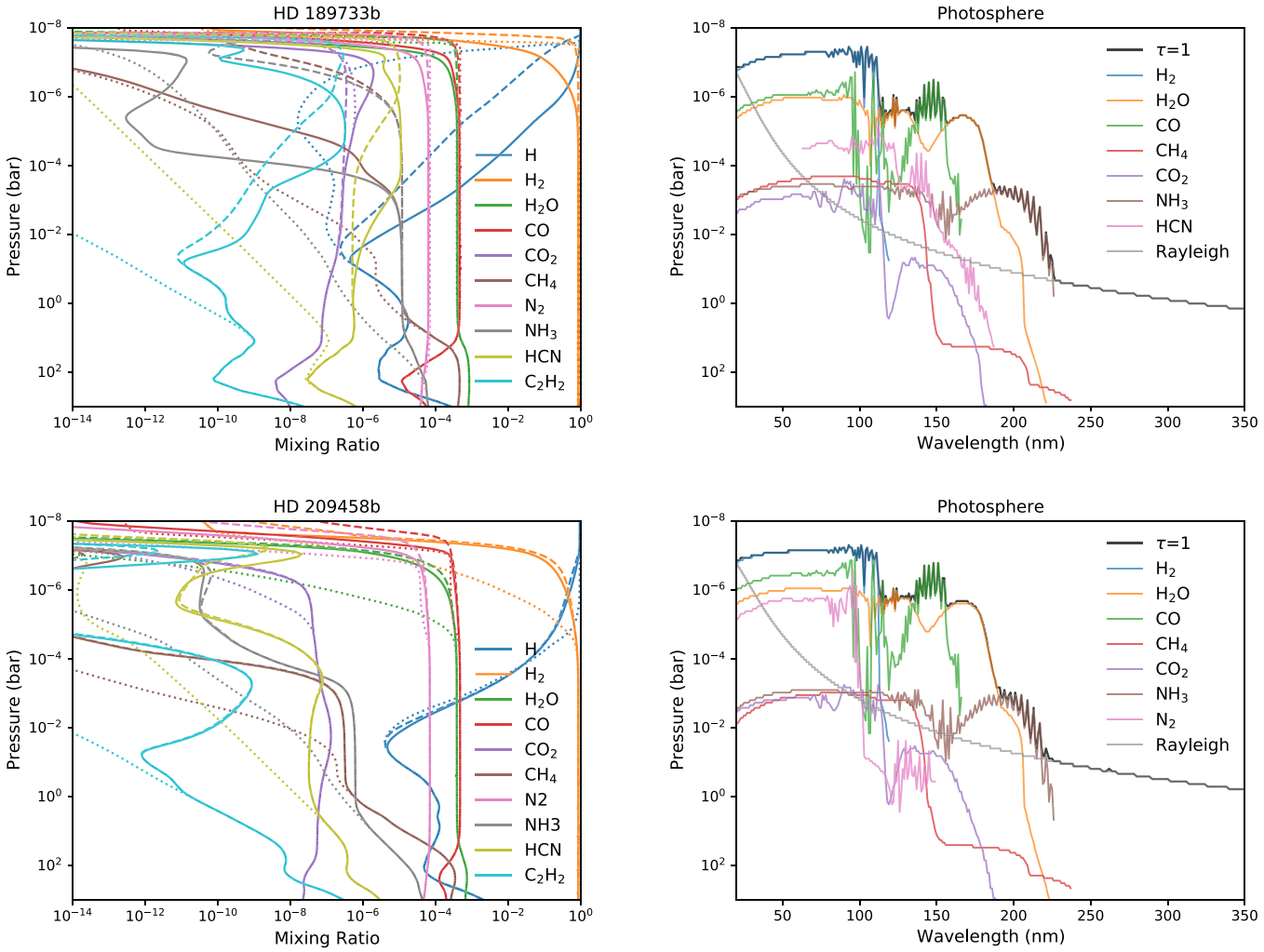

Figure 1. C–H–N–O photochemical kinetics results (top left panel) of HD 189733b (solid), compared with including vertical mixing but no photochemistry (dashed), and thermochemical equilibrium (dotted). The temperature–pressure structure and eddy diffusion (K_{zz}) profile are taken from the dayside-average profile in Moses et al. (2011, their Figures 1 and 2). In the top right panel, we show the pressure level where energetic photons are mostly absorbed, i.e., optical depth $\tau = 1$ (black), and decomposed into the main absorbers. The bottom panels show the same as the top panels, except for HD 209458b.

$CH_3 + C_2H \rightarrow C_3H_3 + H$. We then add hydrocarbons such as C_3H_2, C_3H_4, and C_6H_5 for the hydrogen abstraction reactions of C_3H_3 and C_6H_6 to complete the mechanism.

The rate coefficients of the reactions are broadly drawn from the following: (1) NIST database,[9] (2) KIDA database,[10] and (3) literature sources, including Moses et al. (2005), Lavvas et al. (2008), Moses et al. (2011), and Zahnle et al. (2016). Although most rate coefficients are chosen to be validated for as wide a range as possible (300–2500 K), some of the rate coefficients are still only measured at limited temperature ranges, which has been a long-standing issue in kinetics. The kinetics becomes even more uncertain while sulfur is involved. For example, elemental sulfur in the gas phase exists in many allotropic forms, but the chain-forming reactions between the allotropes were poorly constrained. The recombination rates of S that form the first sulfur bond $S + S \xrightarrow{M} S_2$ from two early measurements by Fair & Thrush (1969) and Nicholas et al. (1979) differ by four orders of magnitude. A recent calculation by Du et al. (2008) confirms the value by Fair & Thrush (1969), and we adopt the rate coefficient from Du et al. (2008) in our network. To address the uncertainties in sulfur kinetics, we perform sensitivity tests for selective key reactions in Section 4.

2.4. Computing Photochemistry

Stars are the ultimate energy source of disequilibrium chemistry. Stellar radiation interacting with the atmosphere can be converted into internal energy, or it can initiate chemical reactions. Photodissociation describes the process in which energetic photons break molecules apart, which is schematically written as a unimolecular reaction with photons ($h\nu$)

$$A \xrightarrow{h\nu} B + C. \quad (7)$$

Photodissociation typically produces active free radicals and initiates a chain of reactions that are essential to atmospheric chemistry (e.g., the ozone cycle on Earth or the organic haze formation on Titan).

The radiative flux that drives photolysis is conventionally defined by the number of photons *from all directions* per unit time per unit area per unit wavelength and is referred to as the

[9] https://kinetics.nist.gov
[10] http://kida.obs.u-bordeaux1.fr/

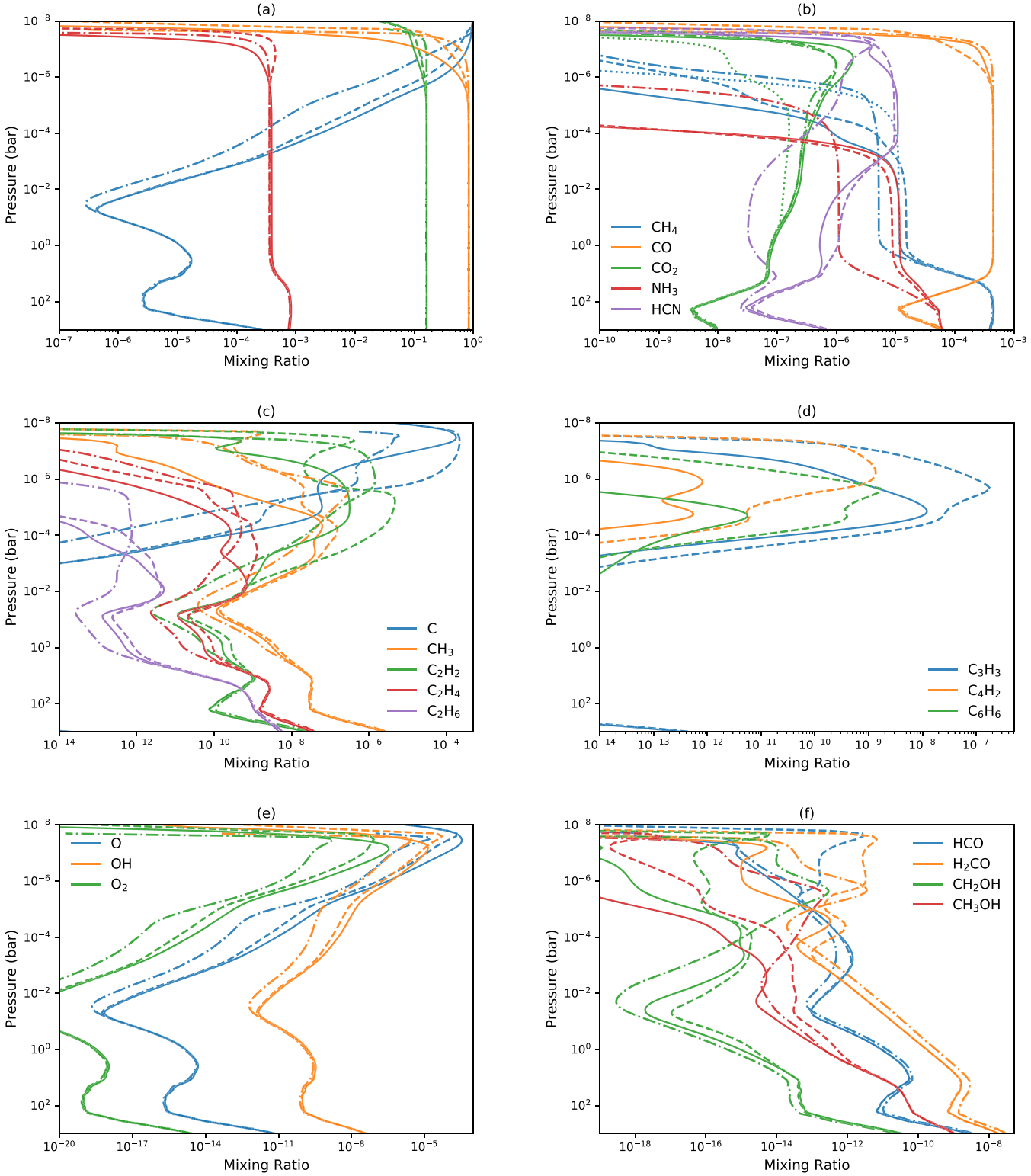

Figure 2. Comparison of atmospheric compositions on HD 189733b computed by VULCAN (solid), Moses et al. (2011) (dashed), and Venot et al. (2012) (dashed–dotted), showing volume mixing ratios of main species (a, b), carbon species (c, d), oxygen species (e, f), and nitrogen species (g, h; some species not included in V12). Additionally, dotted lines for CH_4 and CO_2 are from running VULCAN with the updated methanol scheme from Venot et al. (2020)

actinic flux, $J(z, \lambda)$, with z being altitude and λ being wavelength.

$J(z, \lambda)$ consists of two components, direct beam and diffuse radiation:

$$J(z, \lambda) = J(\infty, \lambda) e^{-\tau(z,\lambda)/\mu} + J_{\rm diff}(z, \lambda), \quad (8)$$

where τ is the optical depth and $\mu = \cos\theta$, with θ being the zenith angle of the incident beam. The first term of Equation (8) describes the attenuated actinic flux reaching the plane perpendicular to the direction of beam (there is no cosine pre-factor as for radiative heating because the number of

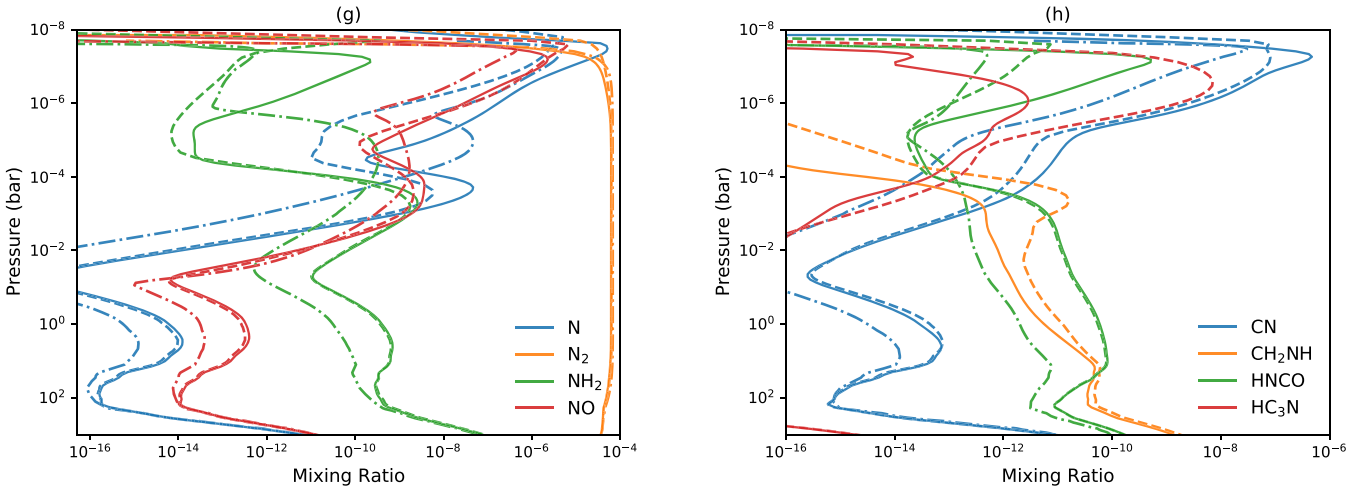

Figure 2. (Continued.)

intercepted molecules is randomly oriented and independent of the direction of the stellar beam).

The optical depth τ accounts for the extinction from both absorption and scattering and is calculated as

$$\tau = \int [\Sigma_i(\sigma_{a,i} + \sigma_{s,i})n_i]dz, \quad (9)$$

where $\sigma_{a,i}$ and $\sigma_{s,i}$ are the cross section of absorption and scattering, respectively. The absorption cross section $\sigma_{a,i}$ can differ from the photodissociation cross section because absorption is not necessarily followed by dissociation. The diffusive flux $J_{\rm diff}$ is the scattered radiation defined by integrating the diffuse specific intensity over all directions. We use the two-stream approximation in Malik et al. (2019) to first solve for the diffuse flux and then convert it to total intensity using the first Eddington coefficient (Heng et al. 2018):

$$J_{\rm diff}(z, \lambda) = F_{\rm diff}/\epsilon, \quad (10)$$

where $F_{\rm diff}$ is the total diffuse flux given by $F_{\rm diff} \equiv F_{\uparrow}^{\rm diff} + F_{\downarrow}^{\rm diff}$ and ϵ is the first Eddington coefficient with value 0.5 for isotropic flux. Although multiple scattering is not explicitly included in the expression in Malik et al. (2019), the process can be approached through iteration, and we find that the equilibrium state of multiple scattering can normally be achieved within 200 iterations for a strongly irradiated hot Jupiter. In the code, we have the option to update the actinic flux periodically to save computing time.

Once the actinic flux has been obtained, the photolysis rate coefficient can be determined by integrating the actinic flux and the absorption cross section over the wavelength

$$k = \int_{\lambda} q(\lambda)\sigma_a(\lambda)J(z, \lambda)d\lambda. \quad (11)$$

and the photolysis rate of Reaction (7) is

$$\frac{dn_{\rm A}}{dt} = -kn_{\rm A}, \quad (12)$$

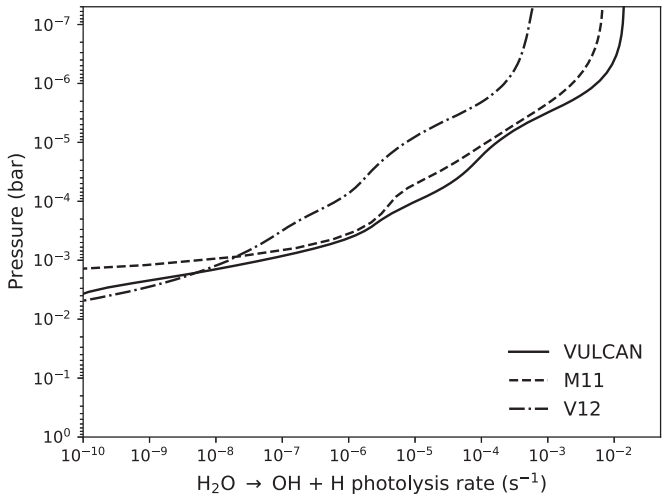

Figure 3. Comparison of the photodissociation rates (s^{-1}) of the main branch of H_2O in HD 189733b computed by VULCAN, M11 (Moses et al. 2011), and V12 (Venot et al. 2012).

where $q(\lambda)$ is the quantum yield (photons^{-1}), describing the probability of triggering a photolysis branch for each absorbed photon. In VULCAN, we adopt the cross sections from the Leiden Observatory database[11] (Heays et al. 2017) whenever possible, which provides tabulated data of photoabsorption, photodissociation, and photoionization cross sections with uncertainty ranking. The data have been benchmarked against other established databases, such as the PHIDRATES database[12] (Huebner et al. 1992; Huebner & Mukherjee 2015), which is detailed in Heays et al. (2017). The full lists of photolysis reactions and references are listed in Table A1.

The spectral resolution with respect to the stellar flux and cross sections can be important while computing Equation (11) numerically. The minimum resolution used in the model should be capable of resolving the line structures in the stellar spectra and cross sections. We discuss the errors from underresolving in Appendix B.

[11] http://home.strw.leidenuniv.nl/~ewine/photo
[12] http://phidrates.space.swri.edu

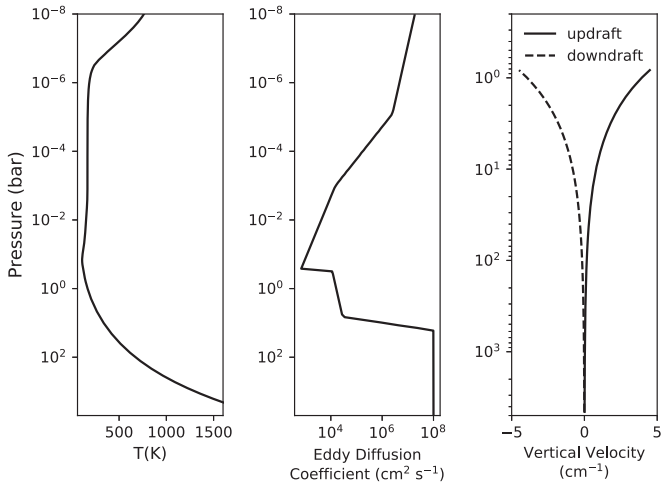

Figure 4. The temperature, eddy diffusion, and deep vertical velocities used for our Jupiter model. The temperature and eddy diffusion in the stratosphere are taken from Moses et al. (2005), while a dry adiabat and uniform eddy diffusion with $K_{zz} = 10^8$ (cm^2 s^{-1}) are assumed for the troposphere. The upward (positive) and downward (negative) vertical velocities are prescribed by Equation (24) with the maximum speed of 5 cm s^{-1} at 0.7 bar.

2.5. Temperature-dependent UV Cross Sections

Most laboratory measurements of UV cross sections are conducted at room temperature or lower, which might raise reliability issues with application to high-temperature atmospheres. Heays et al. (2017) suggested that as temperatures increased by a few hundred kelvin, the excitation of vibrational and rotational levels (limited to $v \leqslant 2$) in many cases only causes minor broadening of the cross sections and does not alter its wavelength integration. However, for molecules with a prominent transition between excited vibrational states (e.g., CO_2), the temperature dependence on the cross section and photolysis rate can be important.

Recent work has started to investigate the high-temperature UV cross sections of a few molecules (Venot et al. 2015, 2018). Given the available data, we have included temperature-dependent photoabsorption cross sections of H_2O (EXOMOL[13]), CO_2 (Venot et al. 2018; with 1160 K from EXOMOL), NH_3(EXOMOL), O_2 (Frederick & Mentall 1982; Vattulainen et al. 1997), SH (Gorman et al. 2019), H_2S (Gorman et al. 2019), COS (Gorman et al. 2019), and CS_2 (Gorman et al. 2019) in the current version of VULCAN. The temperature dependence of the UV cross sections of these molecules can be found in Figure 38. It is evident that both the absorption threshold and cross sections of CO_2 exhibit strong temperature dependence. For H_2O, we have incorporated the recent measurement for the cross section above 200 nm (Ranjan et al. 2020). We follow Ranjan et al. (2020) and take a log-linear fit for the noisy data above 216 nm. In addition, we have included measured data from Schulz et al. (2002) for temperatures above 1500 K.

A layer-by-layer interpolation for the temperature-dependent cross sections is implemented in the model, i.e., the cross section of one single species is allowed to vary across the atmosphere owing to the temperature variation. The interpolation is linear in the temperature space and logarithmic in the cross-section space. With limited data, we find that the linear interpolation in temperature generally underestimates the cross

[13] http://www.exomol.com/data/data-types/xsec_VUV/

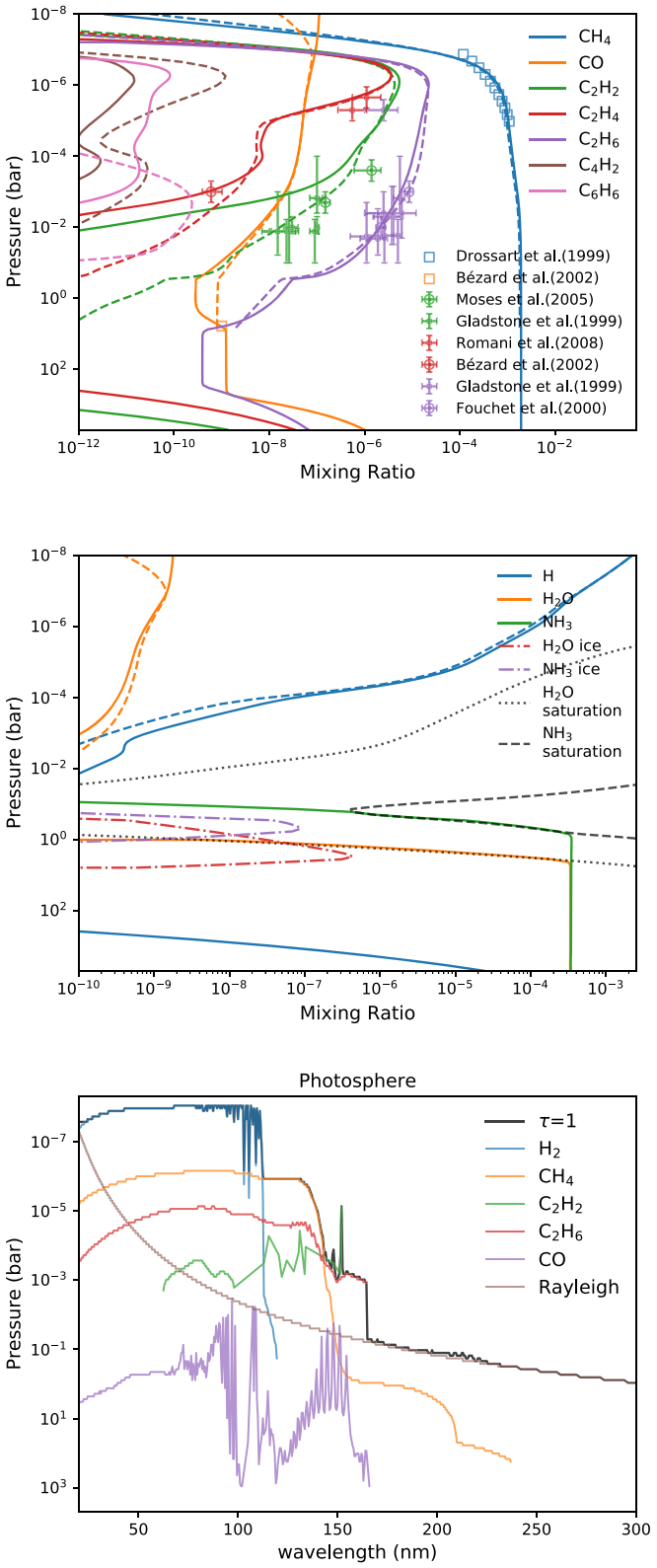

Figure 5. The top panel shows the vertical mixing profiles of important chemical species in our Jupiter model (solid), compared with various observations (data points) of hydrocarbons and the stratospheric distributions from Model A of Moses et al. (2005) (dashed). We follow Rimmer & Helling (2016), placing a factor of two error bars in pressure when they are not given in the observational data. The vapor mixing ratios and cloud densities (g cm^{-3}) of the condensable H_2O and NH_3 are displayed in the middle panel. The bottom panel illustrates the UV photosphere where $\tau = 1$ with decomposition of main absorbers.

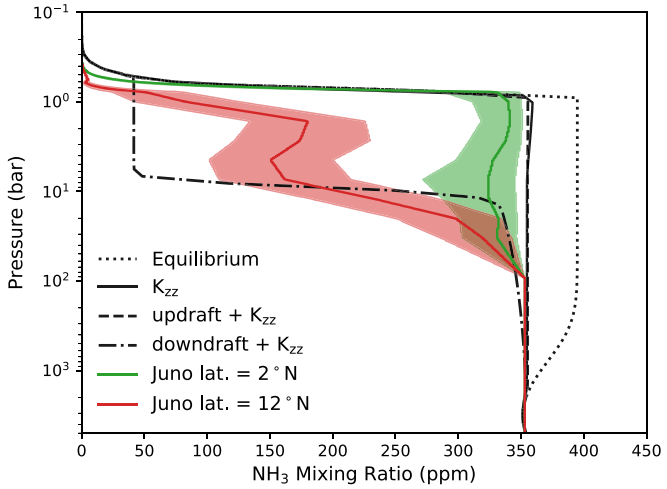

Figure 6. The deep ammonia distribution in parts per million (ppm) computed by our Jupiter model (black), while assuming chemical equilibrium, with eddy diffusion only, and including upward/downward advection for the updraft/downdraft branch (Figure 4), respectively. The red and green profiles show the inferred ammonia distribution at 2° N latitude and 12° N latitude based on Juno microwave measurement by Li et al. (2017), where the shaded areas enclose the 16th and 84th percentiles of the samples in their Markov Chain Monte Carlo runs.

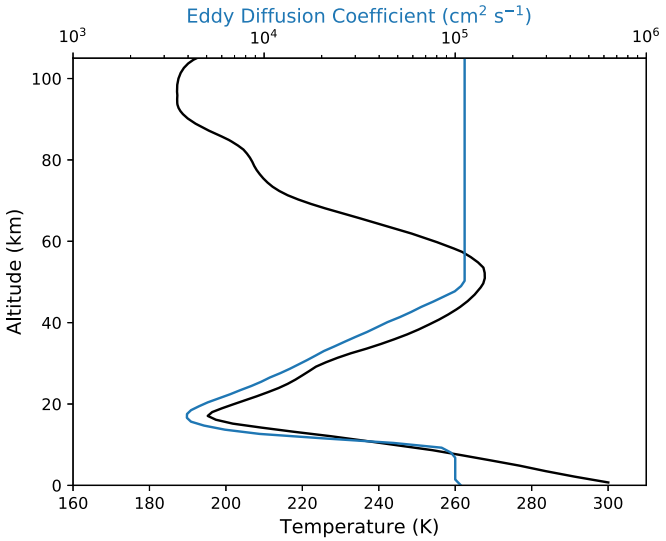

Figure 7. The temperature (at the equator in January from CIRA-86 with references described in the text) and eddy diffusion (K_{zz}) profiles (Massie & Hunten 1981) for the Earth model.

sections, and therefore our implementation is considered as a conservative estimate for how photolysis increases with temperature.

2.6. Condensation and Rainout

VULCAN handles condensation and evaporation using the growth rate of particles, assuming sufficient activated nuclei. For a schematic condensation/evaporation reaction

$$\mathrm{A_{(gas)} \leftrightarrow A_{(particle)}}, \tag{13}$$

the reaction rate is given by the mass balance equation (Seinfeld & Pandis 2016)

$$\frac{dn_\mathrm{A}}{dt} = -\frac{D_\mathrm{A} m_\mathrm{A}}{\rho_p r_p^2}(n_\mathrm{A} - n_\mathrm{A}^\mathrm{sat}) n_\mathrm{A}, \tag{14}$$

where D_A and m_A are the molecular diffusion coefficient and molecular mass of gas A, ρ_p and r_p are the density and radius of the particle, and n_A and $n_\mathrm{A}^\mathrm{sat}$ are the number density and saturation number density of gas A, respectively. Equation (14) describes the growth rate by diffusion for particles with size r_p in the continuum regime (particles larger than the mean free path, i.e., Knudsen number (K_n) smaller than 1). The negative value of Equation (14) corresponds to condensation when $n_\mathrm{A} > n_\mathrm{A}^\mathrm{sat}$, and the positive value corresponds to evaporation when $n_\mathrm{A} < n_\mathrm{A}^\mathrm{sat}$. Our condensation expression takes the same form as Hu et al. (2012) and Rimmer & Helling (2016), except that the growth rate of particles in the kinetic regime (particles smaller than their mean free path, i.e., Knudsen number (K_n) greater than 1) is used in Hu et al. (2012) and Rimmer & Helling (2016). When applying $K_n = \frac{\pi \mu v_\mathrm{th}}{4P}$ (where μ is the dynamic viscosity, v_th is the thermal velocity, and P is the pressure), an H_2 atmosphere enters the kinetics regime with $K_n > 10$ above 1 mbar for a temperature of 400 K and above 0.1 μbar for a temperature of 1000 K. We find that for most of the applications condensation occurs in the lower atmosphere, with micron-size or larger particles, and the continuum regime is more suitable. Since condensation typically operates in a relatively short timescale, we implement an option to switch off condensation, and we fix the abundances of condensing species and the condensates after the dynamic equilibrium has been reached. This approach is similar to the quasi-steady-state assumption method, which decouples the fast and slow reactions to ease the computational load.

After the gas condenses to particles, they fall following the terminal settling velocity (v_s) derived from Stoke's law (Seinfeld & Pandis 2016) as

$$v_s = \frac{2}{9}\frac{\rho_p r_p^2 g}{\mu}, \tag{15}$$

where μ is the atmospheric dynamic viscosity with value taken from Cloutman (2000) for the corresponding background gas. We have again assumed large particle size to simplify the slip correction factor (i.e., the correction for noncontinuum) to unity in Equation (15). In this work, we have implemented and will demonstrate the condensation of H_2O, NH_3, S_2, and S_8 in the following sections.

2.7. Chemistry of Ti and V Compounds

TiO (titanium oxide) and VO (vanadium oxide) are present in the gas phase in cool stars and brown dwarfs where the temperature exceeds 2000 K. The highly irradiated hot Jupiters have been suggested to manifest inverted temperature structures owing to the strong optical absorption of TiO and VO vapor (Hubeny et al. 2003) in the stratosphere. The pioneering work of Fortney et al. (2008) proposing the role of TiO and VO in an irradiated atmosphere is based on equilibrium chemistry, where the authors argue that the conversion between TiO and TiO_2 is fast enough for TiO to remain in chemical equilibrium. However, it is not clear for conversion reactions with Ti or other titanium species. For example, the interconversion of $CO \leftrightarrow CO_2$ is relatively fast, but the ultimate CO abundance is still controlled by the slower $CO \leftrightarrow CH_4$ interconversion. In

addition to TiO, Burrows et al. (2005) suggested that titanium hydride (TiH) is important in brown dwarfs. Since the thermodynamics data of TiH are not available in the literature or standard databases, Burrows et al. (2005) perform ab initio calculations of the Gibbs free energy of TiH (based on the partition function obtained from the spectroscopic constants). To explore the kinetics of titanium and vanadium, we expand the species list to include Ti, TiO, TiO_2, TiH, TiC, TiN, V, and VO. Given that only Ti, TiO, and TiO2 are available for titanium compounds in the NASA polynomials, we adopt the thermodynamics data of TiH from Burrows et al. (2005), TiC from Woitke et al. (2018), and the rest from Tsuji (1973).

While there are a few measurements for the reactions of titanium/vanadium species with laser vaporization at low temperature, the kinetics data at high temperature are nearly nonexistent. As a first step, we perform simple estimates on the unknown rate constants of titanium/vanadium species. First, we look for the kinetics data of analogous transition metals, such as Fe. We assume the same rate coefficient as the analogous reaction if it is measured at high temperature. When high-temperature data are not available, we estimate the temperature dependence based on transition state theory. For an endothermic reaction, we approximate the activation energy (i.e., the exponential term in the Arrhenius expression) by the enthalpy difference between the products and reactants, assuming that the energy increase of the transition state is small compared to the enthalpy difference for reactions involving radicals.[14] Once the activation energy is obtained, the pre-exponential factor is adjusted to fit the reference value at low temperature. The titanium/vanadium kinetics that we adopted are listed in Table B1. For photolysis, we include photodissociation of TiO, TiO_2, TiH, TiC, and VO. We estimate their UV cross sections from FeO (Chestakov et al. 2005) at 252.39 nm and scale the photolysis threshold according to their bond dissociation energy.

2.8. Photochemical Hazy Precursors

Observations have informed us that clouds or photochemical hazes are ubiquitous in a diverse range of planetary atmospheres. Microphysics models that include processes such as nucleation, coagulation, condensation, and evaporation of particles (e.g., Lavvas & Koskinen 2017; Gao & Benneke 2018; Kawashima & Ikoma 2019) simulate the formation and distribution of various-size aerosol particles. Given the complexity and uncertainty of the polymerizing pathways, a common approach is to select precursor species as a proxy and assume they will further grow into complex hydrocarbons (Morley et al. 2013; Kawashima & Ikoma 2018). Typical choices of haze precursors include C_2H_x and HCN, which is also limited by our kinetics knowledge and computing capacity.

In this work, we preferentially consider precursors that are more closely related to forming polycyclic aromatic hydrocarbon (PAH) or nitriles. PAH is a group of complex hydrocarbons made of multiple aromatic rings, which has been commonly found in the smog pollution on Earth and is expected to be associated with the organic haze on Titan (Zhao et al. 2018). In the polar region of Jupiter, where charged particles are the main energy source, ion chemistry has also been suggested to promote the formation of PAHs and organic haze (Wong et al. 2003). Once the first aromatic ring, benzene, has formed, the thermodynamics state (enthalpy and entropy) does not vary much with the processes of attaching and arranging the rings. From the kinetics point of view, the classic mechanism of making complex hydrocarbons, Hydrogen-Abstraction-Carbon-Addition, requires aromatic hydrocarbon and acetylene in the primary abstraction and addition steps (e.g., Frenklach & Mebel 2020). It is conceivable that benzene formation is the rate-limiting step in forming complex hydrocarbons as the growth rate increases downstream from benzene. In practice, while the fundamental pathways leading to PAH remain elusive (Wang 2011; Zhao et al. 2018), the combustion study can (to a certain degree) provide a good understanding of the formation of benzene. Therefore, we suggest considering benzene as an important haze precursor.

One important caveat about modeling benzene is that its photodissociation branches are poorly quantified across various branches (see, e.g., Lebonnois 2005). The main photolysis products are possibly phenyl radical (C_6H_5) and benzyne radical (C_6H_4) (Suto et al. 1992). If they further absorb photons again, then they could fragment into smaller, linear molecules, such as C_4H_3 and C_3H_3. We adopt the cross sections of C_6H_6 from Boechat-Roberty et al. (2004) and Capalbo et al. (2016). For simplicity, we assume that the main dissociation of benzene primarily goes into phenyl radical (C_6H_5), with a small fraction leading to C_3H_3 (~15%, based on Kislov et al. 2004).

Although HCN is the basic molecule for nitrile chemistry, it is unlikely that most of the HCN will convert into complex nitriles. The nitrile formation is more likely to be limited by the less abundant H_2CN, CH_2NH, or CH_3CN. Hence, we include

Table 2
Lower Boundary Conditions for the Earth Validation

Species	Surface Emission[a] (molecules cm^{-2} s^{-1})	V_{dep}[b] (cm s^{-1})
CO[c]	3.7×10^{11}	0.03
CH_4[d]	1.6×10^{11}	0
NO[d]	1.3×10^{10}	0.001
N_2O[d]	2.3×10^{9}	0.0001
NH_3[d]	1.5×10^{9}	1
NO_2	0	0.01
NO_3	0	0.1
SO_2[d]	9×10^{9}	1
H_2S[d]	2×10^{8}	0.015
COS[d]	5.4×10^{7}	0.003
H_2SO_4[d]	7×10^{8}	1
HCN[e]	1.7×10^{8}	0.13
CH_3CN[e]	1.3×10^{8}	0.13
HNO_3	0	4
H_2SO_4	0	1

Notes.
[a] Global emission typically measured in mass budget (Tg yr^{-1}), which is converted to molar flux with the surface area of Earth = 5.1×10^{18} cm^2 for our one-dimensional photochemical model.
[b] Adopted from Hauglustaine et al. (1994).
[c] Smithson (2001).
[d] Seinfeld & Pandis (2016).
[e] Li et al. (2003).

[14] To verify our approach, we compared the activation energy estimated from the enthalpy difference to that of well-measured reactions. For example, endothermic reactions $H_2O + H \rightarrow OH + H_2$ and $CO_2 + H \rightarrow CO + OH$ have activation energy 10,800 K (Davidson et al. 1989) and 13,300 K (Tsang & Hampson 1986), respectively, whereas our estimate yields 7200 and 10,300 K, respectively.

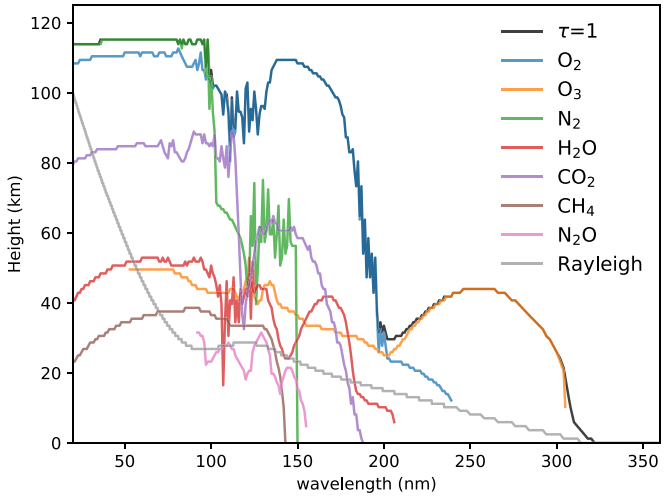

Figure 8. The UV photosphere, i.e., optical depth $\tau = 1$ (black) in our Earth model, overlaid with the composition-decomposed photosphere for several key molecules.

these species along with HC_3N to represent the nitrile family precursor. For sulfur gases, in addition to the condensation of sulfur allotropes (S_x), we also consider CS_2 according to the laboratory experiments by He et al. (2020b). Overall, we compose the following species as photochemical haze precursors: C_2H_2, C_2H_6, C_4H_2, C_6H_6, HCN, HC_3N, CH_2NH, CH_3CN, and CS_2.

3. Model Validation

3.1. HD 189733b

We have benchmarked our thermochemical kinetics results using a C–H–O network with vertical transport against Moses et al. (2011) for HD 189733b and HD 209458b in Tsai et al. (2017). In this work, we compare our results including N–C–H–O photochemistry to Moses et al. (2011, hereafter M11) and Venot et al. (2012, hereafter V12). V12 use a chemical kinetics scheme that is derived from combustion application and find different disequilibrium abundances of CH_4 and NH_3 from those in M11. A size-reduced network based on V11 has since been developed (Venot et al. 2019), with the motivation to support computationally heavy simulations. In particular, the controversial methanol mechanism, which has been identified to cause the differences in CH_4–CO conversion (Moses et al. 2011; Moses 2014), is further updated and analyzed in Venot et al. (2020). Therefore, to consolidate the model discrepancy, we run an additional model with VULCAN but implemented with the updated reduced network from Venot et al. (2020). The planetary parameters and model setting are listed in Table 1. Before moving into a detailed comparison, we provide an overview of the chemical profiles and absorption properties for HD 189733b and HD 209458b in Figure 1.

3.1.1. Disequilibrium Effects

The left panels of Figure 1 depict how vertical mixing and photochemistry drive the compositions out of equilibrium on HD 189733b by isolating the two effects. The underlying processes can be understood as a general property of hot Jupiters (as discussed in Moses et al. 2011; Venot et al. 2012; Moses 2014; Hobbs et al. 2019; Molaverdikhani et al. 2019). Equilibrium chemistry prevails in the deep, hot region, whereas energetic photons dissociate molecules and produce reactive radicals in the upper atmosphere. Between the two regions, the composition distribution is controlled by vertical transport, viz., species in equilibrium at depth are transported upward and become quenched when vertical mixing predominates chemical reactions. Meanwhile, photochemical products are also mixed downward and initiate a sequence of reactions.

The right panels of Figure 1 show the UV photosphere where the optical depth equals 1, with decomposition of contribution from the main molecules. Our photochemical model captures several general transmission properties of irradiated H_2-dominated atmospheres: H_2 provides the dominant absorption in extreme-ultraviolet (EUV; 10–120 nm), whereas H_2O and CO are the dominant absorbers in far-UV (FUV; 120–200 nm). The window around 160–200 nm is particularly important for water dissociation, which makes a catalytic cycle turning H_2 into atomic H (Liang et al. 2003; Moses et al. 2011). In the near-UV (NUV; 300–400 nm), radiation can penetrate deep down to ~1 bar until it is scattered. The photospheres in Figure 1 descend from about 1 μbar to 10 mbar (from the end of H_2 shielding to the tail of ammonia absorption), which denotes the photochemically active region in the atmosphere.

HD 209458b shares qualitatively similar results with HD 189733b. Because of its higher temperature and the inverted thermal structure (see Figure 1 in Moses et al. 2011), the quench level is lifted higher and the photolysis has little influence (as can be seen in Figure 1). The composition distribution on HD 209458b can be described by a lower equilibrium region and an upper quenched region. We will now only focus on HD 189733b for the model comparison because disequilibrium processes contribute more compared to the hotter HD 209458b (see Hobbs et al. 2019 for a model comparison of HD 209458b).

3.1.2. Model Comparison with Moses et al. (2011) and Venot et al. (2012)

The HD 189733b model comparisons between VULCAN, M11, and V12 are showcased in Figure 2, where the top row highlights the major species and the following rows are grouped into carbon, oxygen, and nitrogen species. For the major species, VULCAN produces profiles more consistent with M11, while there are notable differences with V12 in H, CH_4, NH_3, and HCN. CH_4 and NH_3 are quenched from below 1 bar level, until they are attacked by H around 1 mbar. Hence, the differences with V12 in the photospheric region (~1 bar–1 mbar) are due to thermochemical kinetics, rather than photochemical sources. Nitrogen species generally manifest higher variances, reflecting the kinetics uncertainties.

Quenching of CH_4 and NH_3.—The sharp gradients of the equilibrium distribution of CH_4 and NH_3 (Figure 1) imply that the abundances are sensitive to the quench levels, viz., small differences in the quench levels can lead to considerable differences. The key reactions responsible for the conversion at quench levels deserve a closer look.

The match of quenched CH_4 abundance between VULCAN and M11 has been discussed in Tsai et al. (2017), in which we identify a similar pathway of CH_4 destruction to that of M11. The inclusion of nitrogen does not change the fact since nitrogen does not participate in the CH_4–CO conversion. It can be seen that CH_4 is quenched at a higher level with lower mixing ratio in V12, as a result of faster CH_4–CO conversion. Moses (2014) identified the faster methanol decomposition

$H + CH_3OH \rightarrow CH_3 + H_2O$ measured by Hidaka et al. (1989) adopted in V12 as the key reaction that CH_4 exhibits a shorter timescale in V12. Moses (2014) suggested that the rate is overestimated by Hidaka et al. (1989) based on the high-energy barrier of the reaction. In response, Venot et al. (2019) removed the controversial reaction by Hidaka et al. (1989) and updated their chemical scheme with a newly validated CH_3OH combustion work (Burke et al. 2016), given the importance of methanol as an intermediate species for CH_4–CO conversion. Intriguingly, Venot et al. (2019) still find a methane abundance rather close to that in V12.

Attempting to resolve this mystery, we further run our model with the Venot et al. (2020) reduced scheme[15] integrated with the new CH_3OH mechanism. We did not incorporate the same photolysis scheme from V12, but here photolysis has no effects on the quenching comparison below 1 bar. Contrary to the findings in Venot et al. (2020), the new scheme of Venot et al. (2020) implemented in our model indeed shows a slower CH_4–CO conversion and brings the CH_4 profile closer to VULCAN and M11 (dotted line in Figure 2(b)). Our model implemented with the Venot et al. (2020) scheme predicts a quenched methane mixing ratio 1.13×10^{-5}, close to 1.51×10^{-5} in M11 and 1.26×10^{-5} in our nominal model, whereas V12 with the faster methanol decomposition from Hidaka et al. (1989) predicts 5.20×10^{-6}. We conclude that the methanol decomposition indeed results in faster CH_4–CO conversion and subsequently lowers the CH_4 abundance in V12.

For nitrogen chemistry, the high-temperature kinetics is more uncertain, and many reducing reactions relevant for H_2-dominated atmospheres are not available on the NIST database. We drew data from the combustion literature (Dean & Bozzelli 2000, same as M11) and the KIDA database. In particular, there are considerable uncertainties regarding the rates for the reactions that control the NH_3–N_2 conversion, as extensively discussed in Moses (2014). We follow the suggestions in Moses (2014) and adopt the rate coefficient of $NH_3 + NH_2 \rightarrow N_2H_3 + H_2$ from Dean et al. (1984) and that of $NH_2 + NH_2 \rightarrow N_2H_2 + H_2$ from Klippenstein et al. (2009), whereas Konnov & De Ruyck (2001) used in V12 is measured at low temperatures.

As NH_3 progressively becomes fully quenched in the region between a few hundreds of bar and 1 bar, there are more than a single pathway and a rate-limiting step for NH_3–N_2 conversion that effectively control the NH_3 abundance. For pressure greater than ~30 bar, we identify the pathway

$$\begin{aligned} NH_3 + H &\rightarrow NH_2 + H_2 \\ NH_3 + NH_2 &\rightarrow NH_2 + H_3 + H_2 \text{ (i)} \\ N_2H_3 &\xrightarrow{M} N_2H_2 + H \text{ (ii)} \\ N_2H_2 + H &\rightarrow N_2H + H_2 \\ N_2H &\xrightarrow{M} N_2 + H \\ \text{net: } 2NH_3 &\rightarrow N_2 + 3H_2, \end{aligned} \tag{16}$$

where the rate-limiting step switches from Equation (16)-(i) to Equation (16)-(ii) with increasing pressure. In the region with pressure between 30 and 1 bar, we find two pathways with close contribution:

$$\begin{aligned} 2(NH_3 + H &\rightarrow NH_2 + H_2) \\ NH_2 + H &\rightarrow NH + H_2 \\ NH + NH_2 &\rightarrow N_2H_2 + H \text{ (iii)} \\ N_2H_2 + H &\rightarrow N_2H + H_2 \\ N_2H &\xrightarrow{M} N_2 + H \\ H_2 &\xrightarrow{M} 2H \\ \text{net: } 2NH_3 &\rightarrow N_2 + 3H_2 \end{aligned} \tag{17}$$

and

$$\begin{aligned} NH_3 + H &\rightarrow NH_2 + H_2 \\ NH_2 + H &\rightarrow NH + H_2 \\ NH + H &\rightarrow N + H_2 \\ NH_3 + N &\rightarrow N_2H + H_2 \text{ (iv)} \\ N_2H &\xrightarrow{M} N_2 + H \\ H_2 &\xrightarrow{M} 2H \\ \text{net: } 2NH_3 &\rightarrow N_2 + 3H_2, \end{aligned} \tag{18}$$

where Equation (17)-(iii) and Equation (18)-(iv) are the rate-limiting steps.

Our pathways (16) and (17) are identical to those in M11 (Equations (5) and (6) in Moses et al. 2011), although we find that Equation (16)-(i) still plays a role for controlling NH_3 quenching, even with the high-energy barrier given by Dean et al. (1984). As we adopt the same rates for several key reactions relevant for NH_3–N_2 conversion, our model reproduces NH_3 very close to M11, whereas V12 with a faster NH_3–N_2 conversion predicts a higher quench level and lower abundance for NH_3 (Figure 2(b)). In all, we reiterate that further investigation for the key reactions (e.g., Equations (16)-(i), (16)-(ii), (17)-(iii), (18)-(iv)) at high temperatures is required to improve our ability to accurately model the NH_3–N_2 system.

Production of CO_2 and HCN.—Another unexpected change in Venot et al. (2020) is that CO_2 remains in chemical equilibrium across the atmosphere. Our model with the implementation of Venot et al. (2020) scheme confirmed the same result. This is remarkably different from all other models, including V12, where CO_2 is enhanced by photochemically produced OH:

$$CO + OH \rightarrow CO_2 + H. \tag{19}$$

This reaction with the OH radical is expected to rapidly convert CO into CO_2, while the reaction rate is well studied owing to its importance in the terrestrial atmosphere, as well as combustion kinetics. The rate coefficient of Reaction (19) adopted in Venot et al. (2020), $2.589 \times 10^{-16}\ (T/300)^{1.5}\ \exp(251.4/T)$, has a pre-exponential factor about two orders of magnitude smaller than the typical values listed on NIST, as compared in the Appendix C. The slow CO oxidation shuts off the CO_2 production and makes CO_2 retain chemical equilibrium in Venot et al. (2020). We are not sure if this rate constant is part of the updated methanol scheme from Burke et al. (2016) at this point, as to our knowledge the base network in Burke et al. (2016) takes the rate coefficient of Reaction (19) from Joshi & Wang (2006), which is consistent with the literature and faster than that in Venot et al. (2020).

The dissociation of CH_4 and NH_3 leads to the formation of HCN, the primary photochemical product that coupled carbon

[15] The reduced scheme captures the key reactions at work from V12 and has been benchmarked against V12 (Venot et al. 2019). The two schemes are approximately equivalent regarding the quenching of main species.

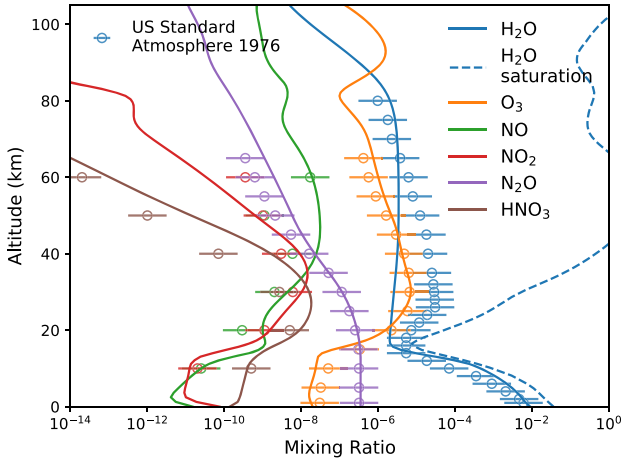

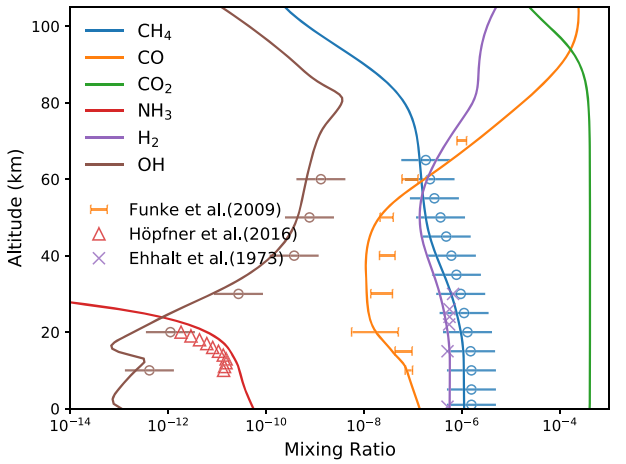

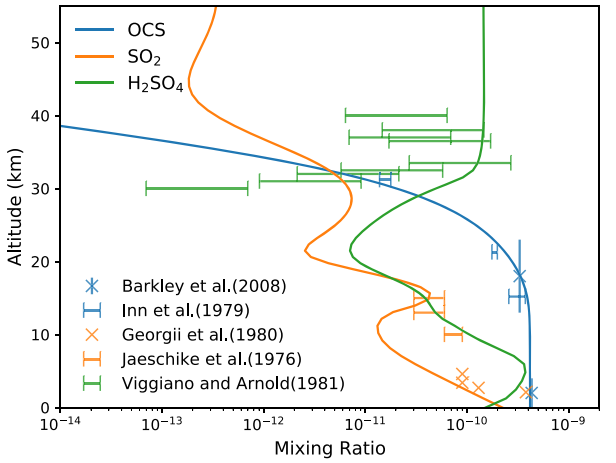

Figure 9. The global-average vertical distribution of key compositions in present-day Earth's atmosphere compared to observations. The H_2O mixing ratio is from the US Standard Atmosphere 1976[*]. Satellite observations of CO in the tropics and NH_3 within 30°–40° N and 70°–80° E in 2003 are measured by the Michelson Interferometer for Passive Atmospheric Sounding (MIPAS; Fischer et al. 2008). The rest of the unlabeled observational data are from Massie & Hunten (1981) and Hudson and Reed (1979). When errors are not included in the published observations, we follow Hu et al. (2012), placing one-order-of-magnitude error bars for the diurnal and spatial variations, e.g., https://www.digitaldutch.com/atmoscalc/help.htm.

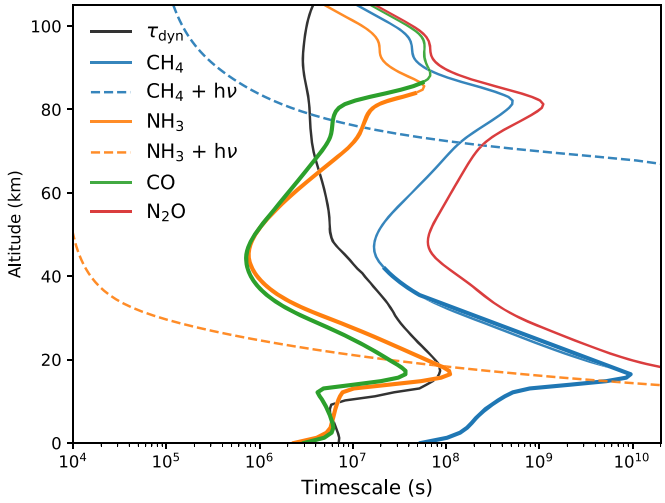

Figure 10. Calculated chemical timescales of some environmentally important gases compared to the dynamical timescale of eddy diffusion in the Earth validation model. The thick lines indicate the region where the oxidation is dominated by OH (i.e., $\tau_{OH} \simeq \tau_{chem}$).

and nitrogen on HD 189733b. HCN becomes the most abundant carbon-bearing molecule next to CO in the upper atmosphere. We identify the pathway in the HCN-dominated region between 1 mbar and 1 μbar as

$$\begin{aligned}
CH_4 + H &\rightarrow CH_3 + H_2\\
NH_3 + H &\rightarrow NH_2 + H_2\\
NH_2 + H &\rightarrow NH + H_2\\
NH + H &\rightarrow N + H_2\\
CH_3 + N &\rightarrow H_2CN + H\\
H_2CN + H &\rightarrow HCN + H_2\\
2(H_2O &\xrightarrow{h\nu} OH + H)\\
2(OH + H_2 &\rightarrow H_2O + H)\\
\text{net: } CH_4 + NH_3 &\rightarrow HCN + 3H_2, \qquad (20)
\end{aligned}$$

which is identical to Equation (14) of Moses et al. (2011). HCN in V12 naturally follows the more scarce CH_4 and NH_3 and presents a lower abundance. We note that Pearce et al. (2019) have run simulations and discovered previous unknown rate coefficients, e.g., the destruction of HCN by reacting with the excited N(^{2}D) could be an important sink of HCN.

Photolysis Effects.—In the upper stratosphere above 1 mbar, the model differences most likely come from photochemical sources. However, it is less straightforward to compare model discrepancy originating from photochemistry, as each step in converting photon fluxes into photolysis rates can give rise to deviation, including stellar fluxes, cross sections, branching ratios, radiative transfer, etc. For simplicity, we will directly inspect the computed photolysis rates from M11, V12, and VULCAN. We limit our comparison to water photolysis, owing to its importance of producing H radicals and the frontline role of H in reacting with molecules such as CH_4 and NH_3 (Liang et al. 2003; Moses et al. 2011).

Figure 3 compares the photodissociation rates of the main branch $H_2O \xrightarrow{h\nu} OH + H$ computed by three models. The water photodissociation rate in VULCAN is about twice as large as

that in M11 and around one order of magnitude larger than that in V12. The H_2O photolysis rates evidently correlate with the H and OH profiles in Figures 2(a) and (e), and molecules in V12 (e.g., CH_4) generally tend to survive toward higher altitude. The disagreement started even from the top of the models, with the same deviation also found across other photolytic species, such as CH_4 and NH_3. This implies that the model implementation of stellar fluxes is the first-order contribution to photochemical differences. However, according to Venot et al. (2012), they found no differences in switching to the same stellar flux from M11 and suggested that Rayleigh scattering could be the source of disagreement. We have tested switching off Rayleigh scattering and found negligible changes, since Rayleigh scattering only dominates in the deep region where photochemistry has ceased (see Figure 1). We note that potential errors with insufficient spectral resolution can contribute to the photolysis rates as well (see Appendix B). Overall, more attention should be paid to calibrating the stellar irradiation for future photochemical model benchmarks, and we suggest using H_2O photolysis as a baseline.

Carbon Species Comparison.—Panels (c) and (d) of Figure 2 show the same comparison for other important carbon-bearing species. Atomic carbon is liberated from CO photodissociation near the top of the atmosphere. CO photolysis appears to be stronger in M11 and generates more atomic carbon around μbar level. The carbon vapor exceeds saturation and can potentially condense in the upper atmosphere. We will examine the implication of C condensation in Section 4.2.3. In the lower stratosphere, various hydrocarbon production is initiated by methane abstraction, i.e., H being successively stripped from CH_4 to form more reactive unsaturated hydrocarbons. The hydrocarbon profiles predicted by M11, V12, and our model are consistent with the divergence of parent CH_4, except that acetylene (C_2H_2) is also governed by atomic C in the upper atmosphere.

C_2H_2 is the most favored unsaturated hydrocarbon on HD 189733b. In the CO-photolysis region, atomic C can couple with nitrogen into CN and eventually produce C_2H_2 by dissociation of HC_3N. Yet we find CH_4 to still be the dominant source for producing C_2H_2 below 1 μbar via a pathway such as

$$\begin{aligned} 2(CH_4 + H &\rightarrow CH_3 + H_2)\\ CH_3 + H &\rightarrow CH_2 + H_2\\ CH_2 + H &\rightarrow CH + H_2\\ CH + H &\rightarrow C + H_2\\ CH_3 + C &\rightarrow C_2H_2 + H\\ 2(H_2O &\xrightarrow{h\nu} H + OH)\\ 2(OH + H_2 &\rightarrow H_2O + H\\ \text{net: } 2CH_4 &\rightarrow C_2H_2 + 3H_2. \end{aligned} \quad (21)$$

Our scheme predicts C_2H_2 with the maximum abundance a factor of a few smaller than V12 and about an order of magnitude smaller than M11.

Ethylene (C_2H_4) is the next most abundant hydrocarbon after acetylene and peaks around 10 mbar. C_2H_4 and other C_2H_x production stems from CH_3 association reaction via the pathway

$$\begin{aligned} H_2O &\xrightarrow{h\nu} H + OH\\ OH + H_2 &\rightarrow H_2O + H\\ 2(CH_4 + H &\rightarrow CH_3 + H_2)\\ CH_3 + CH_3 &\xrightarrow{M} C_2H_6\\ C_2H_6 + H &\rightarrow C_2H_5 + H_2\\ C_2H_5 &\xrightarrow{M} C_2H_4 + H\\ \text{net: } 2CH_4 &\rightarrow C_2H_4 + 2H_2, \end{aligned} \quad (22)$$

where forming C_2H_6 is usually the rate-limiting step. The abundances of C_2H_4 and C_2H_6 in our model are in agreement with M11 within an order of magnitude.

The kinetics beyond C_2 hydrocarbons becomes less constrained (Moses et al. 2011; Venot et al. 2015). As discussed in Section 2.3, we intended to capture the major pathways of producing C_6H_6 as a proxy for haze precursors without invoking an exhaustive suite of hydrocarbons. In our model, C_6H_6 is formed by the pathway

$$\begin{aligned} 9(H_2O + h\nu &\rightarrow H + OH)\\ 9(OH + H_2 &\rightarrow H_2O + H)\\ 6(CH_4 + H &\rightarrow CH_3 + H_2)\\ 4CH_3 + H &\rightarrow CH_2 + H_2)\\ 4(CH_2 + H &\rightarrow CH + H_2)\\ 4(CH + H &\rightarrow C + H_2)\\ 2(CH_3 + C &\rightarrow C_2H_2 + H)\\ 2(C + C_2H_2 &\rightarrow C_3H_2)\\ 2(C_3H_2 + H + M &\rightarrow C_3H_3 + M)\\ C_3H_3 + C_3H_3 + M &\rightarrow C_6H_6 + M\\ \text{net: } 6CH_4 &\rightarrow C_6H_6 + 9H_2, \end{aligned}$$

where the recombination of C_3H_3 is the rate-limiting step (akin to the cooler atmosphere of Jupiter; Moses et al. 2005). Figure 2(d) shows that C_4H_2 and C_6H_6 predicted by our reduced scheme have considerably lower abundances than those in M11. Given the agreement of C_3H_3 up until 10^{-5} bar, we suspect that the differences of C_6H_6 between VULCAN and M11 are due to photodissociation effects from C_6H_6, as well as other species such as CO. Given all the uncertainties and complexity as we mentioned in Section 2.8, we do not consider the predicted abundances of C_4H_2 and C_6H_6 to be accurate, but it should rather serve the purpose for accessing the haze precursors.

Oxygen Species Comparison.—Panels (e) and (f) of Figure 2 compare oxygen-bearing species. The deviation of O, OH, and O_2 again follows the discrepancy in H_2O photolysis, similar to H. There is a minor shift of the equilibrium abundance of H_2CO in V12, possibly from the thermodynamic data difference between JANAF and the NASA polynomial, as pointed out in Tsai et al. (2017). All three models exhibit somewhat different quench levels and profiles for CH_2OH and CH_3OH, which are generally important intermediates for CH_4–CO interconversion (Moses et al. 2011; Tsai et al. 2018; Venot et al. 2020). Nevertheless, this is not reflected in the CH_4 abundance since CH_4 has already quenched in the deeper region. The updated methanol scheme in

Table 3
Parameters of the Planetary Systems

Parameter	WASP-33b	HD 189733b	GJ 436b	51 Eri b
a[a] (au)	0.02558	0.03142	0.02887	11.1
$T_{\rm int}$ (K)	200	⋯	100/400	760
R_s ($R_\odot$)	1.51	0.805	0.464	1.45
R_p (R_J)	1.603	1.138	0.38	1.11
g[b] (cm^2 s^{-1})	2700	2140	1156	18197
$\bar{\theta}$[c]	58	48	58	67
Stellar type	A5	K1-K2	M2.5	F0

Notes.
[a] Orbital distance.
[b] Gravity at 1 bar level.
[c] Mean stellar zenith angle.

Venot et al. (2020) also provides more consistent CH_2OH and CH_3OH distributions with M11 and VULCAN. Since VULCAN adopted the same rate coefficients from the ab initio calculation from M11 for the three methanol reactions, the difference between VULCAN and M11 is more likely associated with reactions involving CH_2OH.

Nitrogen Species Comparison.—Panels (g) and (h) of Figure 2 compare nitrogen-bearing species. N and NH_2 follow the same quench level as NH_3 (panel (b)), since they are part of the NH_3–N_2 conversion. A considerable amount of atomic N is produced above the mbar level by hydrogen abstraction of ammonia, similar to that of methane. Atomic N is oxidized by OH into NO in the upper atmosphere. NO reacts rapidly with atomic C into CN, as the C–N bond is stronger than the N–O bond. CN is an important source of nitrile production, e.g., CN reacts with C_2H_2 to form HC_3N. Our model shows a slower HC_3N production and predicts HC_3N with a peak value about two orders of magnitude lower than M11.

The carbon-nitrogen-bearing species are grouped in Figure 2(h). Since NH_3 quenched first in the deeper layers than CH_4, the quench levels of general carbon-nitrogen-bearing species also follow NH_3. Despite being in trace abundance, CH_2NH and HNCO participate in the HCN-forming mechanism and become important at high pressures. We find HCN formed around 10 mbar via CH_2NH and CH_3NH_2 in a pathway identical to Equation (7) in Moses et al. (2011).

We conclude that we validate our model of HD 189733b by thoroughly reproducing composition distribution within the uncertainty range enclosed by M11 and V12. The kinetics data we employed generally yield quenching behavior close to M11, while our model appeared to predict lower C_2H_2, C_4H_2, C_6H_6, and HC_3N than M11 in the upper atmosphere. Contrary to what has been reported in Venot et al. (2020), we find that the updated methanol scheme in fact increases the quenched CH_4 abundance and is more consistent with that in M11 and this work. The photochemical part of the atmosphere is more complex to diagnose, but we suggest that the implementation of stellar fluxes is the main factor in the discrepancy between M11, V12, and VULCAN.

3.2. Jupiter

The modeling work for Jovian chemistry broadly falls into two categories addressing two main regions: the stratosphere and the deep troposphere. The stratospheric compositions are governed by photochemical kinetics, with the main focus on

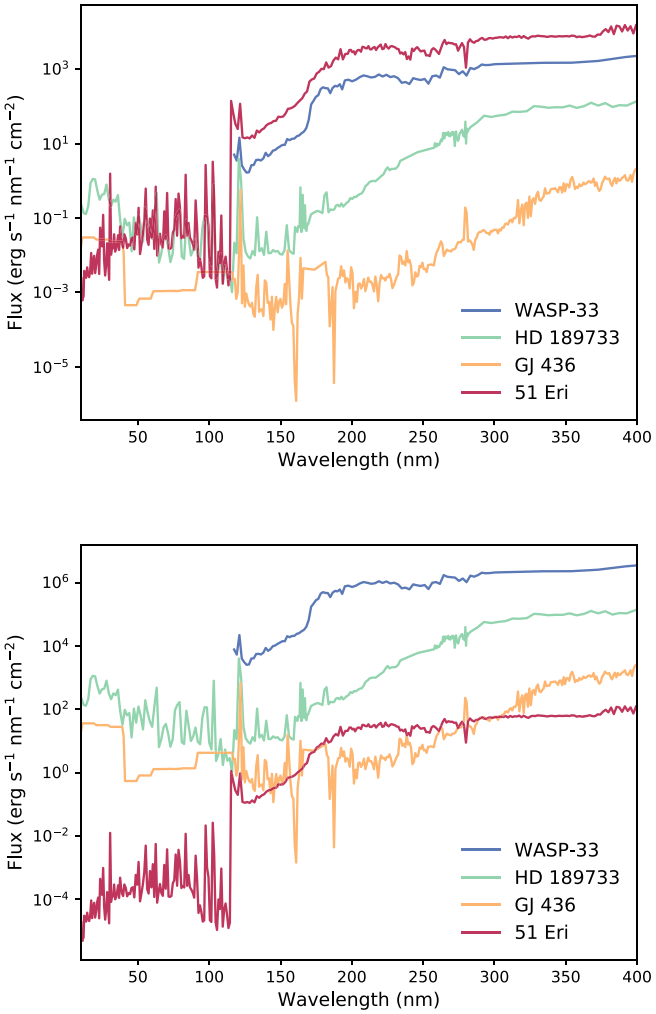

Figure 11. Stellar UV fluxes normalized at 1 au (top) and at the top of the planet's atmosphere (bottom) adopted in our case study models.

understanding the formation of various hydrocarbons. For stratospheric models, fixed mixing ratios or fluxes at the lower boundary need to be specified (Yung & Strobel 1980; Moses et al. 2005). As for the deep tropospheric compositions below the clouds with sparse observational constraints, kinetics models attempt to infer the interior water content based on other quenched species (Visscher et al. 2010; Wang et al. 2016). Since chemical equilibrium is expected to hold in the deep interior, the elemental ratio essentially controls the reservoir of gases and vertical mixing determines the quenched compositions in the upper troposphere.

In this validation, our objective is to validate the chemical scheme at low temperatures with observed hydrocarbons and verify the condensation scheme. We take a general approach by connecting the deep troposphere to the stratosphere and solve the continuity equations consistently. Our lower boundary at 5 kbar is far down in the region ruled by equilibrium chemistry, and zero flux can be applied to the lower boundary. In this setup, fixed-abundance lower boundary conditions are not required as in the stratosphere models (e.g., Moses et al. 2005; Hue et al. 2018). The compositions at the lower stratosphere are physically determined by condensation and transport from the troposphere in the model.

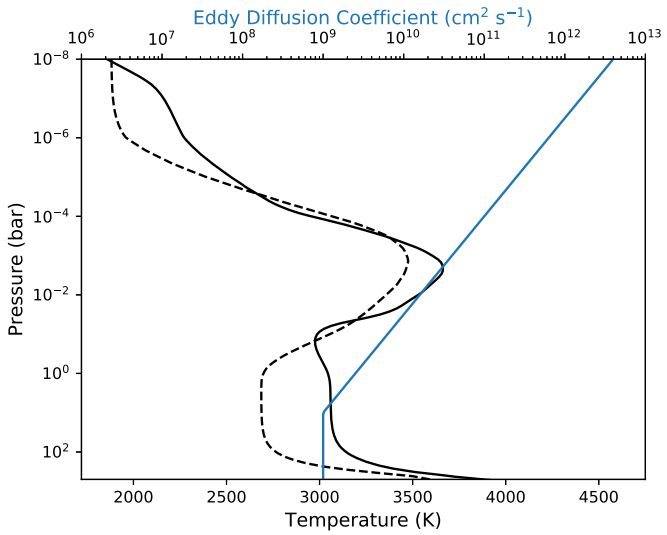

Figure 12. The temperature–pressure and eddy diffusion (K_{zz}) profiles for WASP-33b. Solar elemental abundance (solid) and C/O = 1.1 (dashed) are assumed for calculating the temperature structure.

3.2.1. Model Setup

The temperature profile in the stratosphere and top of the troposphere (above 6.7 bar) is taken from Moses et al. (2005) and extended to 5000 bar following the dry adiabat, with $T = 427.71$ K at 22 bar measured by the Galileo probe as the reference point. We use the same eddy diffusion profile for the stratosphere as Model A of Moses et al. (2005), which is derived from multiple observations. The eddy diffusion is assumed to be constant with 10^8 (cm^2 s^{-1}) in the convective region below 6.7 bar. The temperature and eddy diffusion profiles adopted for our Jupiter model are shown in Figure 4.

Heavy elements in Jupiter are enhanced compared to solar metallicity, except that the oxygen abundance is still unclear. We assign the elemental abundances for the Jupiter model as He/H = 0.0785 (Atreya et al. 2020), C/H = 1.19×10^{-3} (Atreya et al. 2020), O/H = 3.03×10^{-4} (0.5 times solar), and N/H = 2.28×10^{-4} (Li et al. 2017). Sulfur is not included in our Jupiter validation for simplicity. We include condensation of H_2O and NH_3, assuming a single particle size with average radius equal to 0.5 μm for the cloud condensates. Oxygen sources from micrometeoroids are prescribed at the upper boundary at 10^{-8} bar following Moses et al. (2005), with influx (molecules cm^{-2} s^{-1}) of $H_2O = 4 \times 10^4$, CO = 4×10^6, and $CO_2 = 1 \times 10^4$.

3.2.2. Comparing to Stratospheric Observations and Moses et al. (2005)

The top panel of Figure 5 displays the vertical distribution of key species computed by our model, compared to Moses et al. (2005) and various observations. First, CH_4 is the major carbon-bearing species across the atmosphere. It is well mixed until photolysis and separation by molecular diffusion take place at low pressure. The CH_4 distribution in our model matches well with the observation (Drossart et al. 1999). We verify that our treatment of molecular diffusion accurately reproduces the decrease of CH_4 due to molecular diffusion above the homopause.

Second, our model successfully predicts the major C_2 hydrocarbons, which stem from CH_4 photolysis in the stratosphere. Our model tends to predict lower abundances for the unsaturated hydrocarbons C_2H_2 and C_2H_4 than Moses et al. (2005) in the lower stratosphere, but both profiles are within the observational constraints. The UV photosphere in Figure 5 indicates that CH_4 predominates the absorption from Lyα to about 150 nm. We find that the main scheme of converting CH_4 to C_2H_6 in the upper atmosphere is

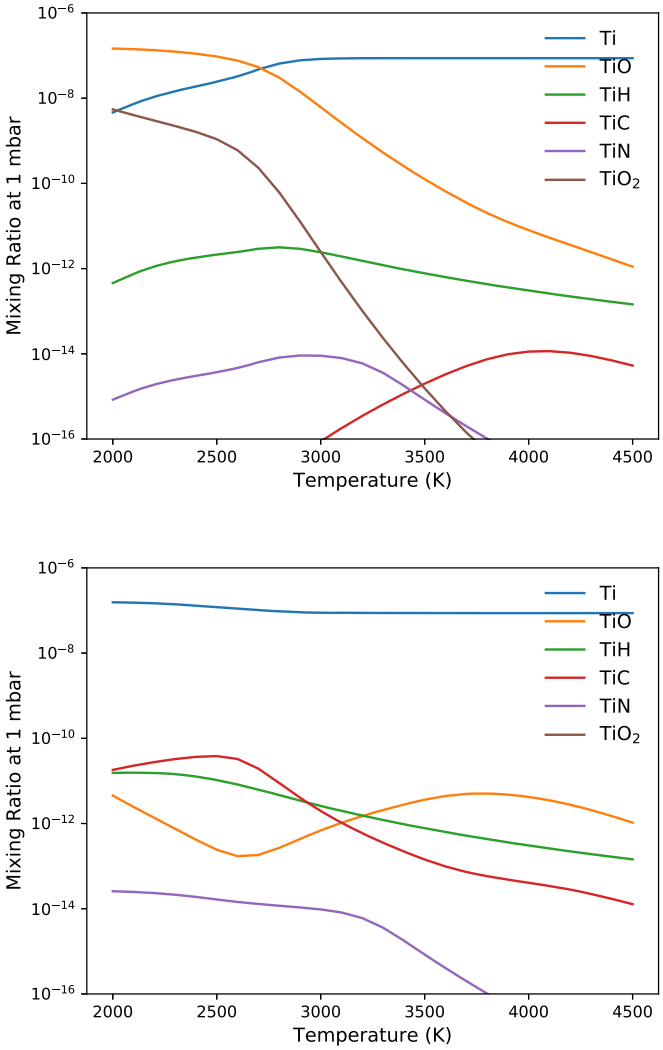

Figure 13. The equilibrium mixing ratios of several gas phase titanium species at 1 mbar as a function of temperature for solar elemental abundance (top) and C/O = 1.1 (bottom).

$$\begin{aligned} 2(CH_4 &\xrightarrow{h\nu} CH_3 + H) \\ 2(CH_3 + CH_3 &\xrightarrow{M} C_2H_6) \\ 2H &\xrightarrow{M} H_2 \\ \text{net: } 2CH_4 &\rightarrow C_2H_6 + H_2 \end{aligned} \quad (23)$$

and the photodissociation branch of methane is replaced by $CH_4 \xrightarrow{h\nu}{}^1CH_2 + H_2$, followed by ${}^1CH_2 + H_2 \rightarrow CH_3 + H$ at higher pressures. We confirm that hydrogen abstraction and three-body association reactions are sensitive to the formation of hydrocarbons on Jupiter as discussed in detail in Moses et al. (2005). Particularly in the lower stratosphere, where temperature drops below 200 K, the rate constants fall out of the valid temperature range or are not well constrained.

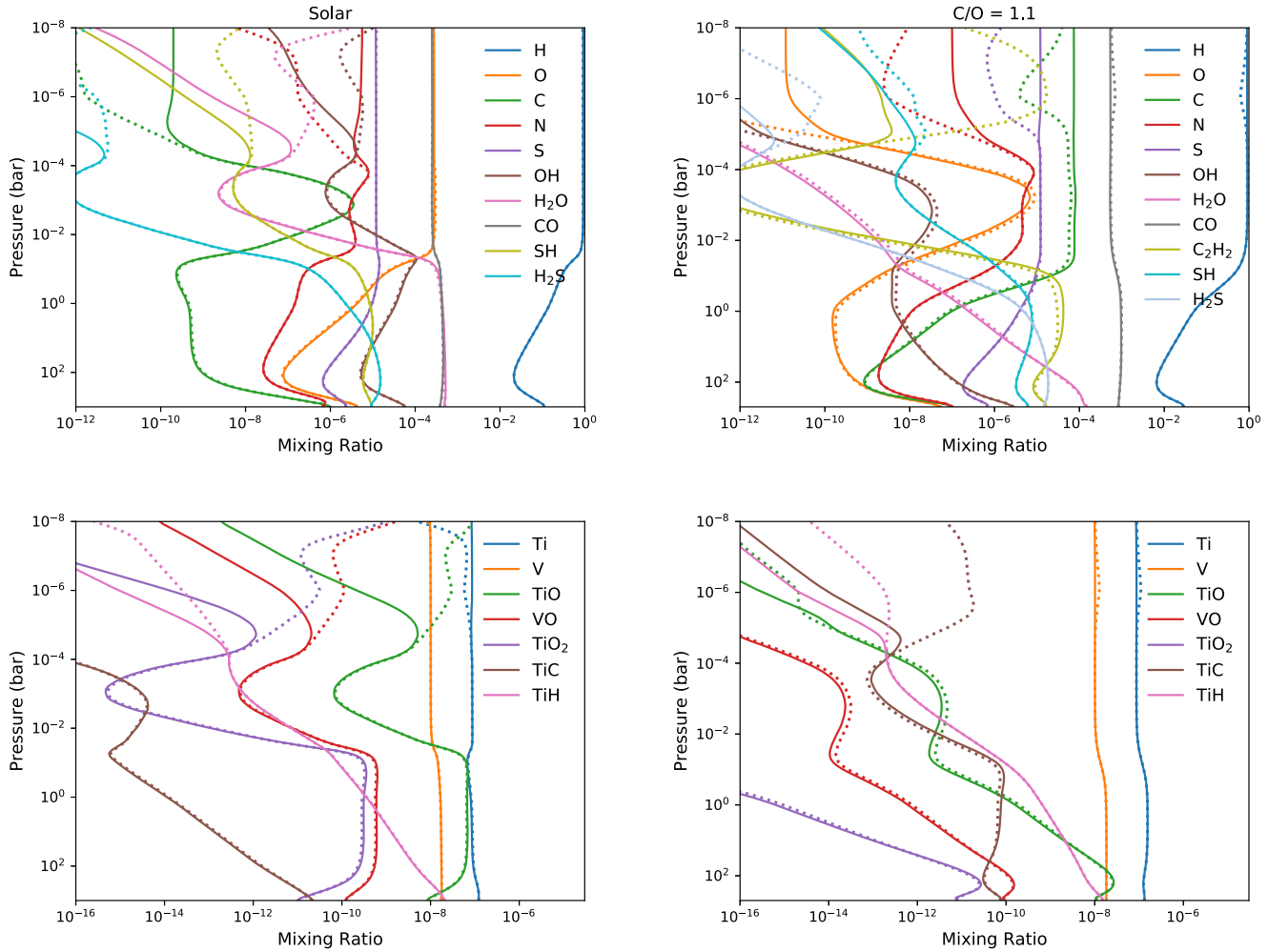

Figure 14. The composition profiles for the main species of interest for WASP-33b, assuming solar C/O (left) and C/O = 1.1 (right). The equilibrium abundances are plotted in dotted lines.

We find that it is particularly important to adopt the low-temperature rate constants for CH_4 and C_2H_x recombination reactions, i.e., $CH_3 + H \xrightarrow{M} CH_4$, $H + C_2H_2 \xrightarrow{M} C_2H_3$, $H + C_2H_3 \xrightarrow{M} C_2H_4$, $H + C_2H_4 \xrightarrow{M} C_2H_5$, and $H + C_2H_5 \xrightarrow{M} C_2H_6$. We also adopt the limit of rate constants below certain threshold temperatures derived by Moses et al. (2005).

Third, our condensation scheme predicts that the location of water-ice clouds starts at 3.6 bar and ammonia clouds at 0.7 bar as shown in Figure 5, consistent with the thermodynamics prediction with 0.5 solar O/H (Atreya et al. 2005; Weidenschilling & Lewis 1973). The ammonium hydrosulfide (NH_4SH) is not considered since sulfur is not included. Last, our model produces lower abundances of C_4H_2 and C_6H_6 at higher altitude compared to those in Moses et al. (2005), which reflects the uncertainties in high-order hydrocarbons and the photolysis branches of C_6H_6.

3.2.3. Spatial Variation of Ammonia due to Vertical Advection

During the Juno spacecraft's first flyby in 2016, the microwave radiometer on Juno measured the thermal emission below the clouds, which was inverted to global distribution of ammonia from the cloud level down to a level of a few hundred bar. A plume-like feature was curiously seen associated with latitudinal variation of ammonia (Bolton et al. 2017). To explore the local impact of advection, we test how the upward and downward motion in a plume can shape the deep ammonia distribution in Jupiter.

Although the Galileo probe has provided constraints on the structure of Jupiter's deep zonal wind (Atkinson et al. 1997) and Juno also sheds light on the vertical extension of the zonal wind (Stevenson 2020), we do not have observational constraints on the deep vertical wind. Hence, we consider a simple but physically motivated (mass-conserving) vertical wind structure without tuning to fit the data. We assume updraft and downdraft plumes starting from the bottom of NH_3-ice clouds at 0.7 bar, in addition to eddy diffusion, as depicted in the right panel of Figure 4. For the nondivergent advection to conserve mass in a one-dimensional column, the vertical velocity at layer j with number density n_j follows

$$v_j n_j = v_{\rm top} n_{\rm top} = \text{constant} \tag{24}$$

such that the net flux remains zero at each layer. For this test, we arbitrarily choose the maximum wind velocity at the top to be 5 cm s^{-1}. This choice has advection timescale shorter than diffusion timescale in the lower-pressure region, i.e., $v_j \gtrsim K_{zz}/H$, which allows us to see the influence of advection. Figure 6 compares the computed distribution of ammonia to

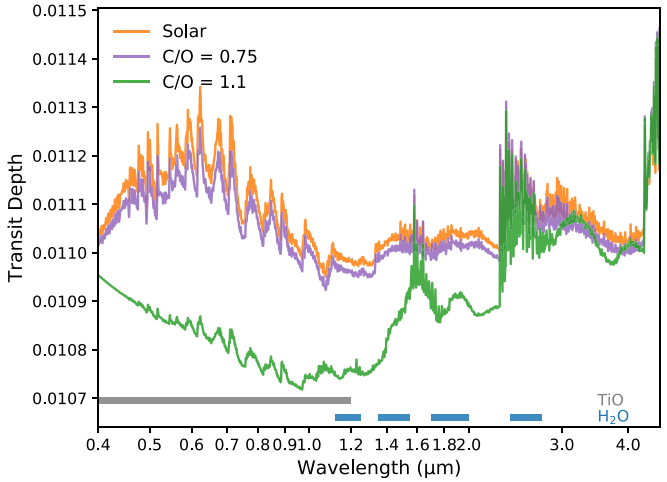

Figure 15. Synthetic transmission spectra for WASP-33b computed from modeled compositions assuming solar elemental abundance, C/O = 0.75, and C/O = 1.1. The absorption features of TiO and H_2O are indicated by the color bands.

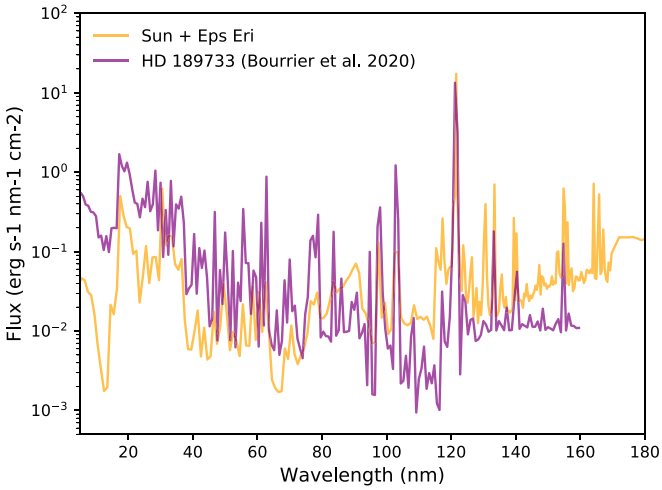

Figure 16. The UV flux of HD 189733 received at 1 au derived from recent observations by Bourrier et al. (2020) compared to the previously adopted spectrum, which consists of solar EUV and epsilon Eridani following the same approach as in Moses et al. (2011) and used in Section 3.1. The spectra are binned for clarity.

that retrieved from Juno measurements (Li et al. 2017; also see updates in Li et al. 2020) at two different latitudes. First, the ammonia distribution predicted by chemical equilibrium is rather uniform with depth, only slightly increasing from 350 to 400 ppm. Next, vertical mixing by eddy diffusion alone makes ammonia quenched from the deep interior below 1000 bar and thus brings ammonia to a slightly lower but uniform concentration of 300 ppm. There is almost no visible difference while including the upward advection since ammonia has already been quenched by eddy diffusion from the deep region. Last, the uniform distribution of ammonia is altered in the downdraft, where the downward motion transports the lower concentration of NH_3 from the condensing region. Our NH_3 distribution is qualitatively consistent with the NH_3-depleted branch at 12° N from Li et al. (2017), where NH_3 reaches a local minimum around 7 bar. We emphasize that this shape cannot be reproduced by eddy diffusion alone.

Although eddy diffusion is probably still essential in practice for parameterizing a range of mixing processes, we demonstrate that including vertical advection can be useful. The advection processes can especially play a bigger part in 2D systems (Zhang et al. 2013; Hue et al. 2015).

3.3. Present-day Earth

Our chemical network has only been applied to hydrogen-dominated, reducing atmospheres so far. In this section, we validate our full S–N–C–H–O network with the oxidizing atmosphere of present-day Earth. The interaction with the surface is particularly crucial in regulating the composition for the terrestrial atmosphere. Surface emission and deposition via biological and geological activities have to be taken into account. Our implementation of the top boundary fluxes and condensation scheme has been validated for Jupiter in the previous section. We will proceed to verify the lower boundary with surface emission and deposition in the Earth model.

3.3.1. Model Setup

We follow Hu et al. (2012), taking the monthly mean temperature at the equator in January 1986 (CIRA-86) from the empirical model COSPAR International Reference Atmosphere[16] (Rees 1988; Rees et al. 1990) as the background temperature profile and the eddy diffusion coefficients from Massie & Hunten (1981), as shown in Figure 7. The winter atmosphere has a colder and hence drier tropopause and better represents the global-averaged water vapor content (see Chiou et al. 1997 and the discussion in Hu et al. 2012).

Unlike gas giants, terrestrial atmospheres typically do not extend to a thermochemical equilibrium region. Instead, biochemical (e.g., plants and anthropogenic pollution) and geological (e.g., volcanic outgassing) fluxes provide surface sources and sinks that are key to regulate the atmosphere. For the lower boundary condition, the global emission budget provides estimates for the surface fluxes, which are conventionally recorded in the units of mass rate (Tg yr^{-1}) and needed to convert to flux (molecules cm^{-2} s^{-1}) in our one-dimensional model.

For Earth and any ocean worlds with large bodies of surface-water reservoir, the standard setup is to fix the surface-water mixing ratio (Kasting & Donahue 1980; Hu et al. 2012; Lincowski et al. 2018). We set the surface mixing ratio of water to 0.00894, corresponding to 25% relative humidity. Surface CO_2 is also fixed at 400 ppm for simplicity, since we did not consider several major sources and sinks of CO_2 at the surface, such as respiration, photosynthesis, ocean uptake, weathering, etc. The specific emission fluxes and deposition velocities for the lower boundary are listed in Table 2, while zero-flux boundary is assumed for all remaining species. We initialize the atmospheric composition with well-mixed (constant with altitude) 78% N_2, 20% O_2, 400 ppm CO_2, 934 ppm Ar, and 0.2 ppb SO_2.

For the solar flux, we adopt a recently revised high-resolution spectrum (Gueymard 2018), which is derived from various observations and models (see Table 1 of Gueymard 2018). The solar radiation was cut from 100 nm in Hu et al. (2012) for the missing absorption from the thermosphere. We do not find it necessary, as we set the top layer to the lower thermosphere around 110 km and the EUV absorption is naturally accounted for. We have also tried including the absorption from atomic

[16] https://ccmc.gsfc.nasa.gov/pub/modelweb/atmospheric/cira/cira86ascii

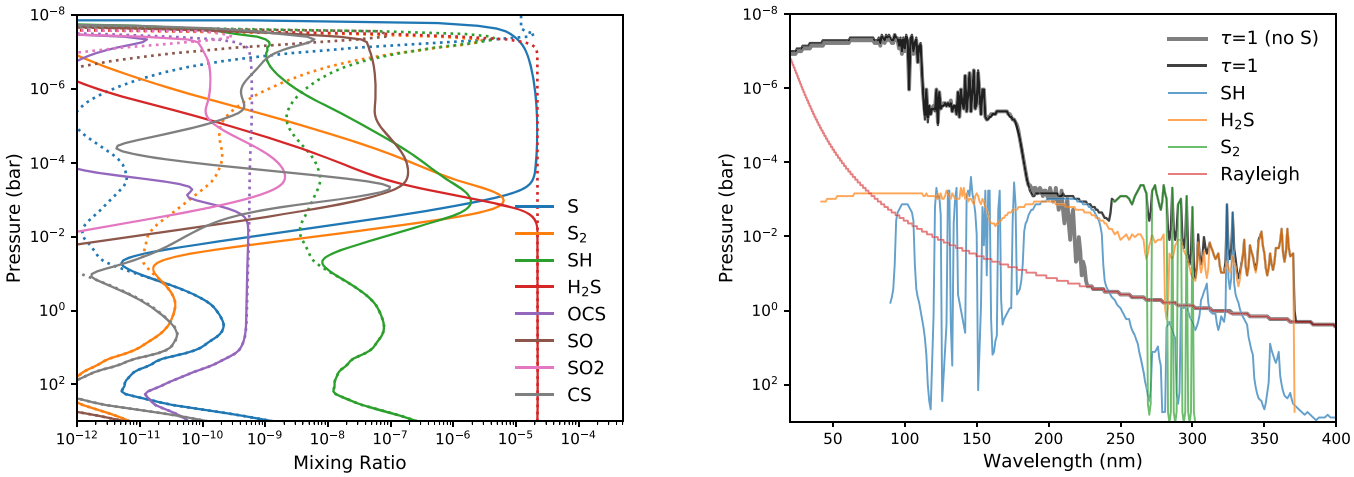

Figure 17. Left: mixing ratios of the major sulfur species computed in the model of HD 189733b. The photochemical kinetics results are shown with solid lines, and equilibrium abundances are shown with dotted lines. Right: the pressure level of optical depth $\tau = 1$ as a function of wavelength while including (black) and excluding (gray) sulfur chemistry, along with the main individual contribution from sulfur species.

oxygen and nitrogen and found no differences regarding the neutral chemistry in the lower atmosphere, since N_2 and O_2 have already screened out the bulk EUV. The chlorine chemistry and lightning sources for odd nitrogen are not included in this validation.

3.3.2. Results

Molecular oxygen (O_2) and ozone (O_3) are the main players in Earth's photochemistry. O_2 absorbs vacuum ultraviolet (VUV) below 200 nm, and O_3 takes up the radiation longward of about 200 nm, which blocks the harmful UV from life on the surface. The penetration level of solar UV flux shown in Figure 8 indicates that ozone absorbs predominately between 20 and 50 km. The basics of the oxygen–ozone cycle are described by the Chapman mechanism (e.g., Yung & DeMore 1999; Jacob 2011). Our full chemical network encompasses the catalytic cycles involving hydrogen oxide and nitrogen oxide radicals that are responsible for the ozone sinks in the stratosphere. Although the catalytic cycle of chlorine that accounts for additional ozone loss is not included, we are able to reproduce the observed global-average ozone distribution in Figure 9.

Our condensation scheme captures the cold trap of water in the troposphere, i.e., the water vapor entering the stratosphere is set by the tropopause temperature. Above the tropopause, water is supplied by diffusion transport from the troposphere and oxidation of CH_4. We find that the conversion in the stratosphere goes through the steps

$$\begin{aligned}
CH_4 + OH &\rightarrow H_2O + CH_3\\
2(O3 &\xrightarrow{h\nu} O_2 + O(^1D))\\
2(O(^1D) + N_2 &\rightarrow O + N_2)\\
CH_3 + O &\rightarrow H_2CO + H\\
O + H_2CO &\rightarrow HCO + OH\\
HCO + O_2 &\rightarrow CO + HO_2\\
CO + OH &\rightarrow CO_2 + H\\
HO_2 + OH &\rightarrow H_2O + O_2\\
2(H + O_2 &\xrightarrow{M} HO_2)\\
\text{net: } CH_4 + 2OH + 2O_3 &\rightarrow CO_2 + 2H_2O + 2HO_2, \quad (25)
\end{aligned}$$

effectively turning one CH_4 molecule into two H_2O molecules (Noël et al. 2018). H_2O eventually photodissociated in the mesosphere and produced H_2, as indicated by the profiles in Figure 9. Overall, our model produces water distribution consistent with observations considering the diurnal and spatial variations.

The two oxides of nitrogen, NO and NO_2, cycle rapidly in the presence of ozone:

$$\begin{aligned}
NO + O_3 &\rightarrow NO_2 + O_2\\
NO_2 + O &\rightarrow NO + O_2\\
\text{net: } O_3 + O &\rightarrow 2O_2.
\end{aligned}$$

Thus, NO and NO_2 are conventionally grouped as NO_x. The burning of fossil fuel accounts for about half of the global tropospheric emission (e.g., Table 2.6 of Seinfeld & Pandis 2016). NO_x is mainly lost by oxidation into nitric acid (HNO_3): $NO_2 + OH \xrightarrow{M} HNO_3$. Our model reproduces the distribution of NO_x, whereas our higher HNO_3 in the upper stratosphere is seemingly attributed to missing the hydration removal in the actual atmosphere.

Nitrous oxide (N_2O) is mainly emitted by soil bacteria, prescribed by the surface emission at the lower boundary. There are no efficient N_2O removal reactions in the troposphere, and N_2O remains well mixed as one of the important greenhouse gases. N_2O is predominantly removed by photodissociation in the stratosphere. Our calculated N_2O is in agreement with the observations for the troposphere and stratosphere. Although similar to Hu et al. (2012), our model slightly overpredicts its abundance above 50 km, which is likely due to missing the photolysis branch of N_2O that produces excited oxygen $O(^1S)$.

CH_4 is the most abundant hydrocarbon in Earth's atmosphere, with the surface emission largely coming from human activities (e.g., agriculture), as well as natural sources (e.g., wetlands). CH_4 is oxidized into CO and eventually CO_2 by OH through multiple steps similar to Equation (25) in the stratosphere. CO is produced by combustion activities with about 0.1 ppm concentration near the surface (Seinfeld & Pandis 2016), as a result of the balance among the emission flux, OH oxidization, and dry deposition. CO is continuously

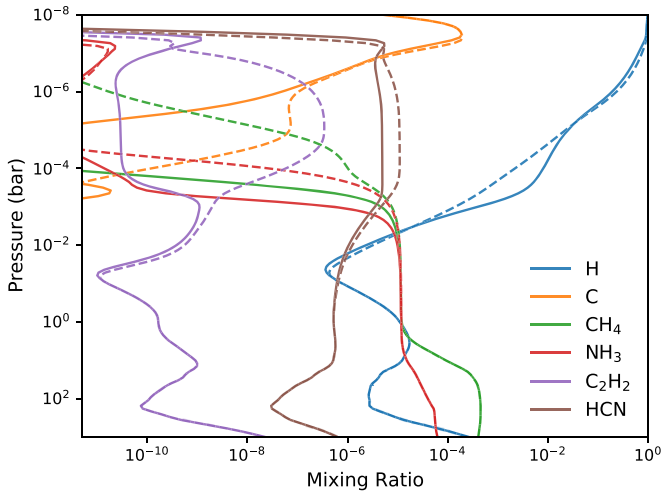

Figure 18. Mixing ratio profiles of main species on HD 189733b that exhibit differences from models including sulfur kinetics (solid) and without sulfur kinetics (dashed).

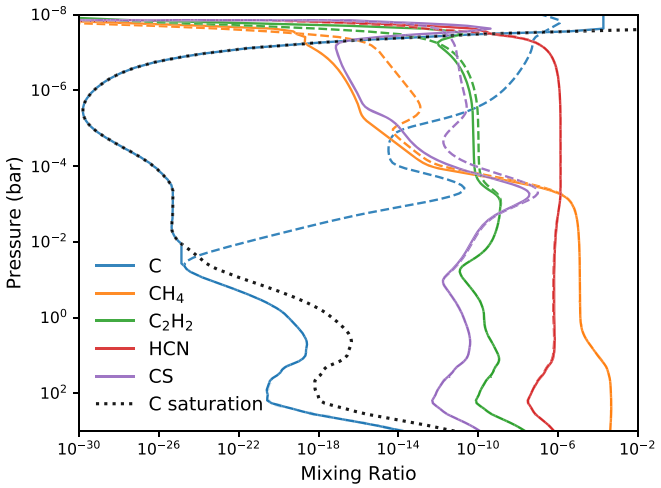

Figure 19. Several carbon-containing species from the nominal model (dashed) compared to those from the model with limited C due to instantaneous condensation. The saturation mixing ratio of C is shown with the dotted curve.

removed by OH through the troposphere and generated by photodissociation of CO_2 in the thermosphere and mesosphere, as depicted by their distributions in Figure 9. As the major oxidizing agent, OH is an important diagnostic species for Earth's photochemical model. It is mainly produced in the stratosphere during daytime initiated by ozone photolysis and regenerated in the troposphere by NO_x (see, e.g., Jacob 2011). The OH distribution in our model is consistent with that in Massie & Hunten (1981). We will further discuss using calculated OH concentration to estimate the chemical timescale of long-lived species against oxidation in the next section.

Carbonyl sulfide (OCS) is the main sulfur species in the troposphere, emitted by direct outgassing or oxidation of carbon disulfide (CS_2) and dimethyl sulfide (DMS) released by the ocean (Barkley et al. 2008; Seinfeld & Pandis 2016). OCS is rather stable in the troposphere until entering the stratosphere, where it is photodissociated or oxidized by OH and ultimately turned into sulfuric acid. Sulfur dioxide (SO_2) is another important sulfur-containing pollutant from fossil fuel combustion. SO_2 oxidation begins from the troposphere with

$$SO_2 + OH \xrightarrow{M} HSO_3.$$

HSO_3 radical rapidly reacts with oxygen to form SO_3,

$$HSO_3 + O_2 \rightarrow SO_3 + HO_2,$$

followed by sulfuric acid formation

$$SO_3 + H_2O \rightarrow H_2SO_4.$$

The sulfur-containing gases in our model generally agree with the global distribution, while the mismatch of H_2SO_4 is expected, as our model does not include H_2SO_4 photodissociation and heterogeneous reactions that efficiently remove H_2SO_4 from the gas phase.

3.3.3. Chemical Lifetime

The oxidizing capacity of Earth's atmosphere is important for decontaminating toxic and greenhouse gases, such as CO, CH_4, and various volatile organic compounds. The oxidizing power is not only essential for regulating habitable conditions but also key to address the stability of biosignature gases for other terrestrial planets. Here we present a brief overview of the key timescales for some important trace gases from our Earth model.

OH radical is the primary daytime oxidizing agent in our biosphere. The chemical timescale of species A against oxidization (τ^{A}_{OH}) can be estimated by the computed OH concentration as

$$\tau^{A}_{OH} = \frac{[A]}{k_{A-OH}[A][OH]} = \frac{1}{k_{A-OH}[OH]}, \quad (26)$$

where $k_A - OH$ is the rate coefficient of the oxidizing reaction of A + OH. In the upper atmosphere, where molecular collision is less frequent, the excited $O(^1D)$ produced by ozone photolysis is not immediately stabilized and becomes the main oxidant. We consider the two major oxidizing paths across the atmosphere and write the chemical timescale against oxidation as

$$\tau^{A}_{chem} = \frac{1}{k_{A-OH}[OH] + k_{A-O(^1D)}[O(^1D)]}. \quad (27)$$

Figure 10 illustrates the chemical timescales (τ_{chem}) along with photolysis timescales ($1/k_{photo}$) for several trace gases, where τ_{OH} (thick lines) inversely correlates with temperature in general. We can gain some insights by comparing τ_{chem} to the dynamical timescale of vertical mixing ($\tau_{dyn} = H^2/K_{zz}$): in the troposphere, CH_4 and N_2O display rather well-mixed abundances owing to their longer chemical lifetime. CO and NH_3 have comparable τ_{chem} with τ_{dyn} and exhibit a negative gradient with altitude from oxidation removal. In the stratosphere, NH_3 is rapidly photodissociated, while CH_4 is transported from the troposphere and oxidized into CO. In the thermosphere above ~80 km, the oxidation by $O(^1D)$ takes over for most species, but mixing processes with a shorter timescale here control the chemical distribution. For example, CO abundance starts to increase with altitude from about 60 km as a result of downward transport of CO produced by CO_2 photodissociation in the upper atmosphere.

In summary, we validate our photochemical model with HD 189733b, Jupiter, and Earth, for a wide range of temperatures and oxidizing states. The inclusion of nitrogen and sulfur

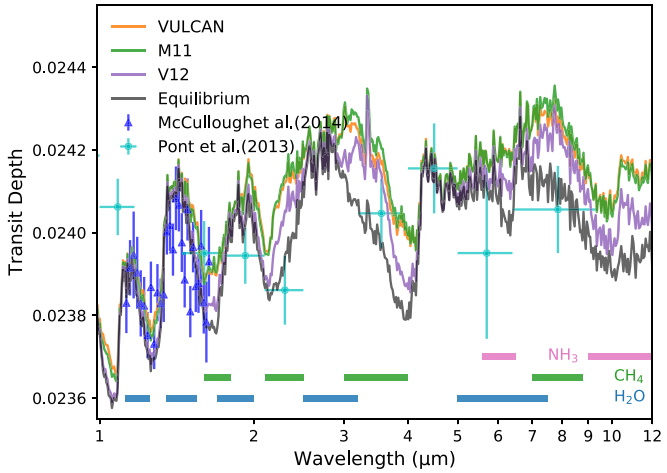

Figure 20. Synthetic transmission spectra for HD 189733b generated from chemical abundances computed by VULCAN, Moses et al. (2011), and Venot et al. (2012), and when assuming chemical equilibrium. Transit observations from Pont et al. (2013) and McCullough et al. (2014) are shown as data points with error bars. The absorption features for the main molecules are indicated by the color bands.

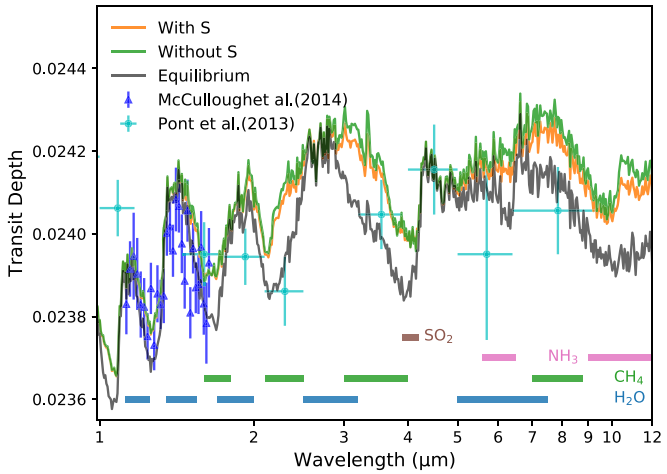

Figure 21. Same as Figure 20, but with abundances computed from our model while including or excluding sulfur species.

chemistry and the implementation of advection, condensation, and boundary conditions are verified by comparing with models and/or observations. The discrepancies in previous models of HD 189733b are identified for future investigation.

4. Case Study

In this section, we select WASP-33b (ultrahot Jupiter), HD 189733b (hot Jupiter), GJ 436b (warm Neptune), and 51 Eridani b (young Jupiter) to perform case studies. Each case represents a distinctive class among gas giants with H_2-dominated atmospheres. The effective temperatures of these objects span 700–3000 K, while having host stars of various stellar types. We investigate how disequilibrium processes play a part for these cases, with additional attention on the effects of sulfur chemistry and photochemical haze precursors.

All the P–T profiles in this section are generated using the open-source radiative transfer model, HELIOS, except we keep the same P–T profile of HD 189733b as in Section 3.1 for comparative purposes. HELIOS employs a two-stream approximation and correlated-k method to solve for the radiative

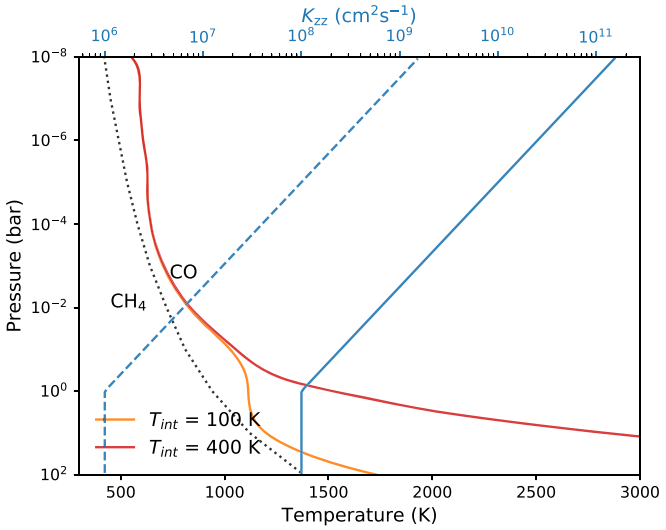

Figure 22. The temperature−pressure and eddy diffusion (K_{zz}) profiles for GJ 436b, showing low ($T_{\rm int}$ = 100 K) and high ($T_{\rm int}$ = 400 K) internal heating and weak (dashed) and strong (solid) vertical mixing. The [CH_4]/[CO] = 1 equilibrium transition curve for 100 times solar metallicity is shown by the dotted curve.

−convective equilibrium temperature consistent with thermochemical equilibrium abundances. The gaseous opacities include H_2O, CH_4, CO, CO_2, NH_3, HCN, C_2H_2, NO, SH, H_2S SO_2, SO_3, SiH, CaH, MgH, NaH, AlH, CrH, AlO, SiO, CaO, $CIA_{H_2-H_2}$, CIA_{H_2-He}, and additionally TiO, VO, Na, K, and H- for WASP-33b. The P–T profiles are fixed without taking into account the radiative feedback from disequilibrium chemistry (but see Drummond et al. 2016 for the effects on HD 189733b). The astronomical parameters used are listed in Table 3. The dayside-average stellar zenith angle is used for WASP-33b and GJ 436b, and the global-average stellar zenith angle is used for 51 Eri b (see Appendix C), except that we keep the same value for HD 189733b to compare with the results in Section 3.1. The stellar UV fluxes adopted for each system are compared in Figure 11, with a detailed description in each section.

For the eddy diffusion (K_{zz}) profiles in our case studies (except that we again retain the same profile for HD 189733b from Moses et al. 2011), we assume K_{zz} to be constant in the convective region and increasing roughly with inverse square root of pressure in the stratosphere (Lindzen 1981; Parmentier et al. 2013). The expression as a function of pressure in bar ($P_{\rm bar}$) takes a similar form to that in Charnay et al. (2015) or Moses et al. (2016):

$$K_{zz} = K_{\rm deep}\left(\frac{P_{\rm tran}}{P_{\rm bar}}\right)^{0.4}, \quad (28)$$

where $P_{\rm tran}$ is the transition pressure level informed by the radiative transfer calculation. The more irradiated atmospheres have deeper radiative−convective transition levels and greater $P_{\rm tran}$. A common way of estimating $K_{\rm deep}$ in the convective region is applying the mixing length theory with the knowledge of convective heat flux. For WASP-33b, most of the modeled atmosphere is in the radiative region. We choose $K_{\rm deep}$ such that the overall pressure-dependent K_{zz} profile matches that derived from the vertical wind in the general circulation model (GCM). For GJ 436b, $K_{\rm deep}$ is treated as a loosely constrained

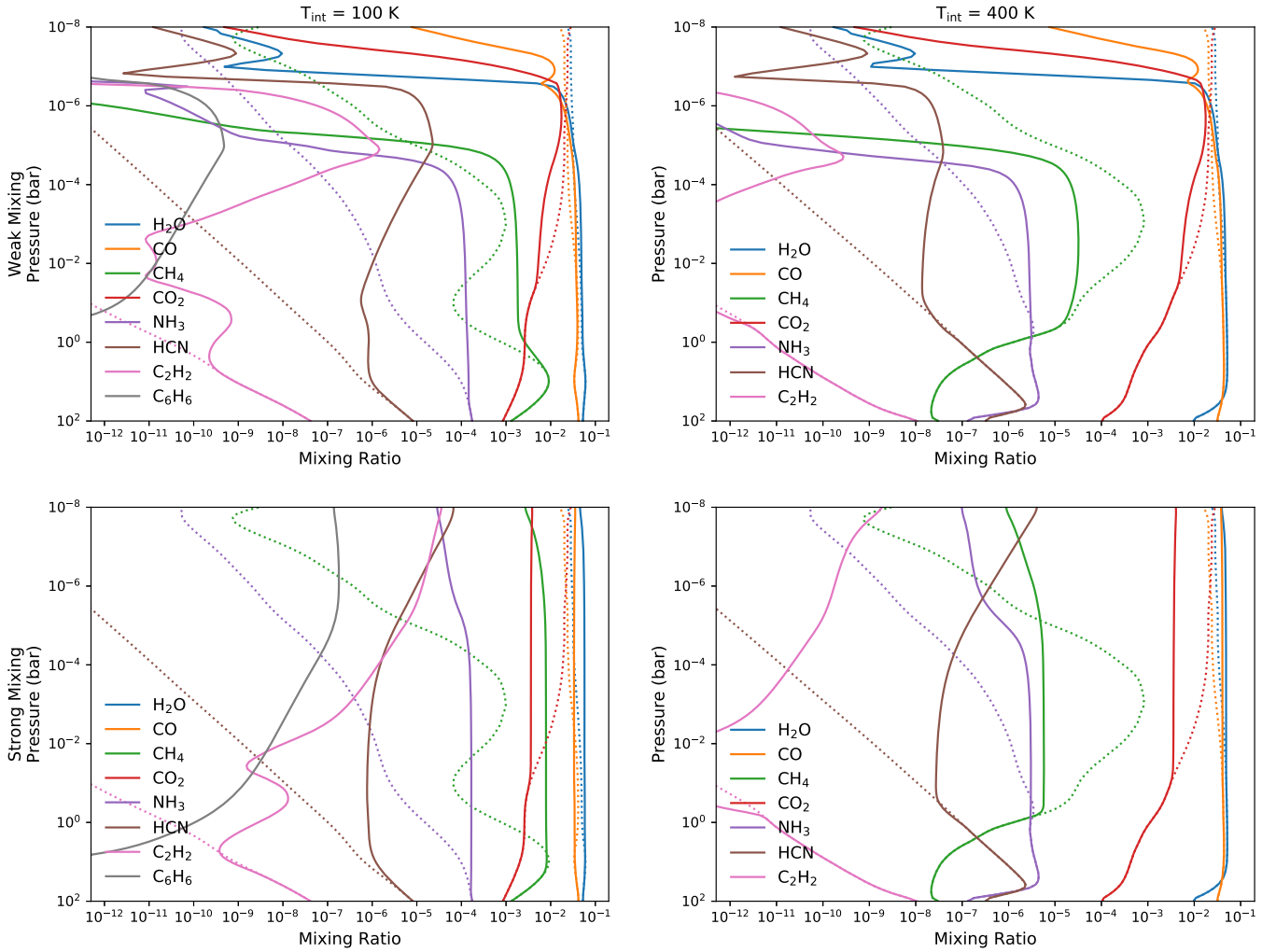

Figure 23. The mixing ratio profiles (solid) along with equilibrium profiles (dotted) of several main species on GJ 436b for different assumptions of internal temperature and vertical mixing. The left/right columns correspond to low/high ($T_{\rm int}$ = 100 K/$T_{\rm int}$ = 400 K) internal heating, and the top/bottom rows correspond to weak/strong vertical mixing.

free parameter along with the internal heating we explored (Section 4.3.1). $K_{\rm deep}$ is likely more important in controlling the quenched species for cooler planets, such as 51 Eri b, where we adopted a value of $K_{\rm deep}$ that can produce quenched CH_4 consistent with the observations.

We run nominal models for all planets in this section with the S–N–C–H–O chemical network.[17] We recognize that there are considerable uncertainties in sulfur kinetics, as discussed in Section 2.3. In order to gauge the uncertainty effects of our sulfur scheme, we explore the sensitivity to sulfur chain-forming reactions for GJ 436b and OCS recombination for 51 Eridani b. After chemical abundances are obtained, we use the open-source tool PLATON (Zhang et al. 2019, 2020) to generate transmission spectra and HELIOS for the emission spectra.

4.1. WASP-33b

WASP-33b is among the hottest gas giants discovered, with dayside temperature around 3000 K (von Essen et al. 2020). To date it remains the only case showing evidence of both temperature inversion and TiO features (Serindag et al. 2021), which makes WASP-33b an interesting target for testing the stability of TiO/VO along with other molecules. Previous work on ultrahot Jupiters is limited by the assumption of chemical equilibrium chemistry (Kitzmann et al. 2018; Parmentier et al. 2018; Zhang et al. 2018). Here, we will verify the equilibrium assumption by exploring how disequilibrium processes affect the titanium and vanadium compounds with different C/O ratios.

4.1.1. Stellar UV Flux and Eddy Diffusion

The host star WASP-33 is an A5-type star with effective temperature about 7400 K. We use the UV spectrum of HD 40136 (F0 type) merged with a 7000 K atlas spectrum from Rugheimer et al. (2013) as an analog. The star is fast rotating and exhibits pulsations, which might add more uncertainties to the UV flux. Nevertheless, as we will see in Section 4.1.3, photodissociation solely converts more molecules to atoms at this high temperature, and the results should be qualitatively robust.

Vertical wind generally correlates with the planet's effective temperature (Komacek et al. 2019; Tan & Komacek 2019; Baxter et al. 2021). We assume the value of K_{zz} based on the

[17] included in the supplementary material

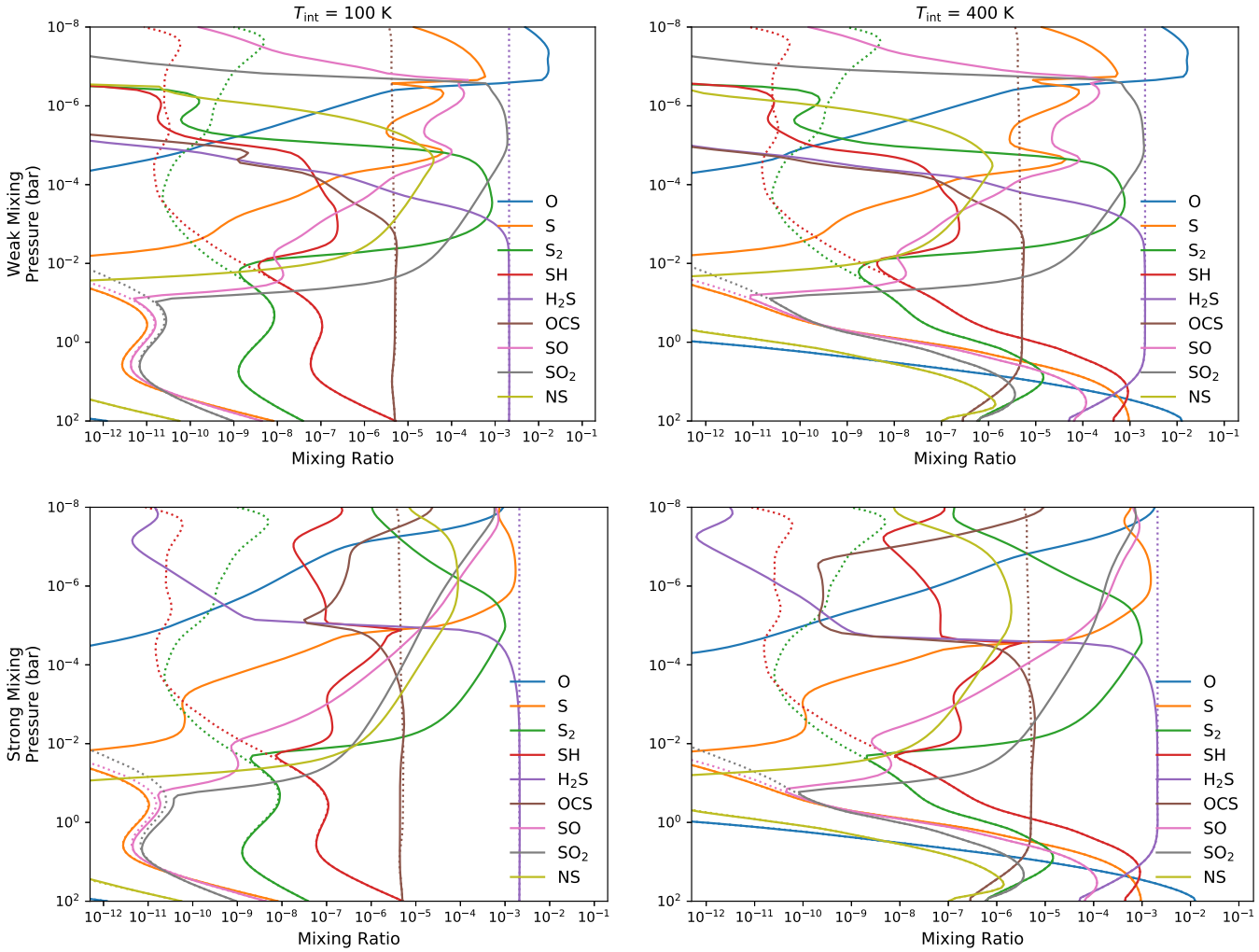

Figure 24. Same as Figure 23, but for atomic O and sulfur species.

simulations in Tan & Komacek (2019), where the global rms vertical wind increases with decreasing pressure and reaches about 100 m s^{-1} at 1 mbar (personal communication). The vertical wind translates to $K_{zz} \sim 10^{11}$ cm^2 s^{-1} around 1 mbar. The temperature and eddy diffusion profiles for WASP-33b are shown in Figure 12.

4.1.2. Chemical Equilibrium

We first look at the trends associated with thermal dissociation governed by thermochemical equilibrium under carbon-poor and carbon-rich conditions, for which we assume a solar C/O and C/O = 1.1, respectively. Figure 13 illustrates how titanium compounds vary with temperature in equilibrium at 1 mbar. For solar C/O, titanium mainly exists in the form of Ti and TiO. As temperature exceeds about 2500 K, TiO becomes unstable against thermal dissociation and its abundance falls with temperature. For C/O = 1.1, TiO is depleted owing to the scarcity of oxygen, as oxygen preferably combines with the excess carbon to form CO (Madhusudhan 2012). Atomic titanium is the major species across this temperature range, and TiC, TiH, and TiO have close abundances.

The effects of thermal dissociation on WASP-33b are clearly visible in the equilibrium profiles in Figure 14. The blistering heat of WASP-33b makes all elements predominantly exist in the atomic form above 0.1 bar, where temperature starts to increase with altitude and exceeds 3000 K, while CO with the strong C–O bond is the only molecule that survives the high temperature. For solar C/O ratio, as the majority of C is locked in CO, atomic C tracks the temperature structure, whereas oxides such as H_2O, TiO, VO, and TiO_2 display inverse trends with temperature. For C/O = 1.1, atomic O swaps place with C, and TiO and VO are significantly depleted.

4.1.3. The Effects of Disequilibrium Chemistry

For a typical hot Jupiter (e.g., HD 189733b), vertical mixing plays a major role controlling the chemical distribution in the photosphere. However, it is not the case for WASP-33b, as we compare the equilibrium and disequilibrium mixing ratio profiles in Figure 14. Although the strength of eddy diffusion also increases with temperature, faster thermochemical reactions still prevail upon vertical mixing. The deviation of disequilibrium profiles above the temperature-inverted region ($\sim 10^{-4}$ bar) is due to photodissociation, which reduces molecular species and produces more atoms. In the absence of vertical quenching, the depleted TiO in a carbon-rich condition is unable to be replenished by vertical transport from the deep region, as

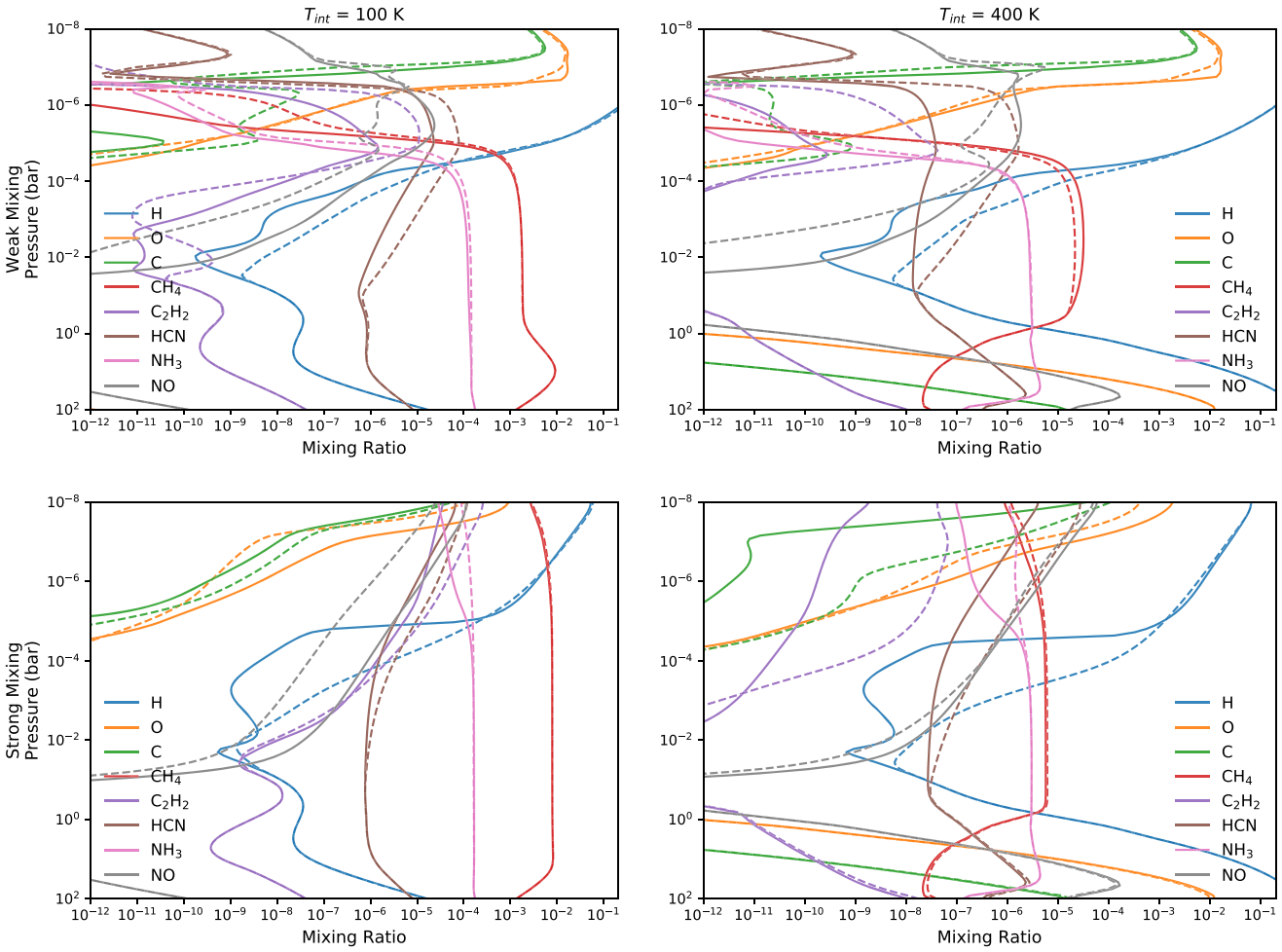

Figure 25. The abundances of several main species that show differences from models including sulfur kinetics (solid) and without sulfur kinetics (dashed). Each panel corresponds to the same internal heating and vertical mixing as in Figure 23.

seen in Figure 14. In the photodissociation region, in principle, stronger vertical mixing can transport more molecules upward against photodissociation. We have performed additional tests with eddy diffusion profile varied by a factor of 10. Yet we found that the change is minor and our results are not too sensitive to K_{zz}.

For sulfur species, sulfur atom S is also the favored form, followed by hydrogen sulfide (SH). The formation of S_2 and other polysulfurs (S_x) is entirely shut down at this extremely high temperature. Sulfur does not couple to oxygen, carbon, or nitrogen since it mostly remains in the atomic form. Lastly, because the adopted stellar spectrum is truncated around Lyα, we have further extended the stellar spectrum to include the EUV flux shorter than Lyα using the synthetic spectra by PHOENIX.[18] Apart from more C atoms from CO photodissociation above 10^{-5} bar, we find no notable differences in all other species. Overall, the composition distribution of WASP-33b resembles that of a hot Jupiter, except without a vertical quench region. The atmosphere of WASP-33b can be divided into a photochemically influenced region and a thermochemical equilibrium region, with the transition at the top of the temperature-inverted layer around 10^{-4} bar.

[18] http://phoenix.astro.physik.uni-goettingen.de/

4.1.4. Transmission Spectra

We have computed the synthetic spectra from equilibrium and disequilibrium abundances and found no observable differences in both transmission and emission spectra. The photochemical region above the temperature-inverted region is too optically thin, even when molecules like H_2O and TiO are strongly photodissociated here. High-resolution spectroscopy might be more sensitive to probe the atomic species in this region.

Alternatively, the equilibrium abundances of TiO/VO are sensitive to the change of elemental abundance. Figure 15 demonstrates that the opacity in the optical is most sensitive to the change of TiO/VO as C/O is close to unity, which shows even greater variation than H_2O absorption between 1.2 and 2 μm.

In conclusion, we find that photodissociation only impacts the upper atmosphere of WASP-33b, where $P < 0.1$ mbar, and chemical equilibrium is generally a valid assumption, as has been found for KELT9-b (Kitzmann et al. 2018) and ultrahot Jupiters with dayside temperatures above 3000 K. Atmospheric mixing might still play an important role in an atmosphere with temperature lower than WASP-33b. Our first attempt to solve the kinetics of titanium species can provide an interesting

avenue for investigating other transition metals such as Fe and Ca for future study of ultrahot Jupiters.

4.2. HD 189733b

We have benchmarked our model of HD 189733b in Section 3.1, where we attempt to keep the astronomical and chemical setup as close to Moses et al. (2011) and Venot et al. (2012) as possible for comparison. In this section, we include the following updates and aspects that have not been considered in previous work:

1. Recently observed stellar UV flux of HD 189733 (Bourrier et al. 2020).
2. Sulfur chemistry.
3. Condensation of carbon vapor.

4.2.1. Stellar UV Flux

Bourrier et al. (2020) combine HST and XMM-Newton observations and derive semisynthetic UV spectra up to 160 nm. For our model benchmark in Section 3.1, solar flux is used for wavelengths below 115 nm, and the observed spectrum of epsilon Eridani (a K2-type analog) is adopted for 115–283 nm. The previously adopted and newly observed stellar fluxes are compared in Figure 16. The EUV flux of HD 189733 is modestly higher than that of the Sun, but the photochemically important FUV ($\lambda > 122$ nm) flux appears to be weaker. Nevertheless, the change in the UV flux turns out to only slightly decrease the atomic H (by about 20%). The overall impact of the updated EUV flux on neutral chemistry is in fact insignificant.

4.2.2. Sulfur Chemistry

We next run the same model except including sulfur kinetics. The sulfur species from our photochemical calculation are illustrated in Figure 17 and are broadly consistent with previous work (Zahnle et al. 2009). Hydrogen sulfide (H_2S) is the thermodynamically stable form of sulfur in a hydrogen-dominated atmosphere. H_2S is mostly destroyed by hydrogen abstraction

$$H_2S + H \rightarrow SH + H_2 \tag{29}$$

and restored by the reverse reaction of Equation (29). The forward and backward reactions of Equation (29) essentially dictate the level where H_2S starts to lose its stability. On HD 189733b, H_2S is dissociated above 1 mbar and predominantly turned into S. SH and S_2 also reach maximum values at the level where H_2S dissociation kicks off. The implication is that both SH and S_2 absorb shortwave radiation and could potentially provide stratospheric heating, especially with the supersolar metallicity condition as discussed in Zahnle et al. (2009).

We find SO accumulated in the upper atmosphere from the oxidation of $S + OH \rightarrow SO + H$. The highly reactive SO is known to self-react into SO dimer ((SO)2) and may facilitate formation of S_2O and S_2 (Pinto et al. 2021) or back into S and SO_2. What actually happened in our model is that SO either photodissociated or reacted with atomic H back to S in the low-pressure region. The elemental S might be subject to photoionization, as we will discuss in Section 5.

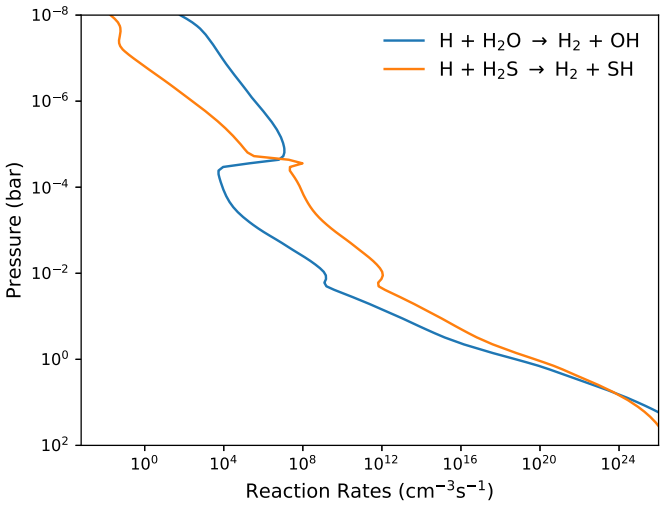

Figure 26. The rates of reactions that are key to recycle H back to H_2 in the GJ 436b model including sulfur kinetics with $T_{int} = 400$ K and weak vertical mixing (corresponding to the bottom right panel of Figure 25).

One notable effect of photochemistry with sulfur is that several sulfur species absorb in the mid-UV/NUV. As illustrated in Figure 17, sulfur species raised the UV photosphere above ~230 nm, compared to that without sulfur, where there is no efficient absorption beyond the ammonia bands. We find H_2S responsible for the dominant absorption in the NUV (300–400 nm), rather than SH as reported in Zahnle et al. (2009), which might be caused by the isothermal atmosphere at 1400 K used in Zahnle et al. (2009). The absorption of S_2 between 250 and 300 nm and the SH peaks around 325 nm can make prospective observable features.

Figure 18 highlights the compositional differences when sulfur is present. Sulfur species can play an interesting role in catalyzing conversion schemes that take multiple steps. In particular, CH_4 is more diminished down to about 1 mbar. We find that sulfur provides a catalytic pathway for CH_4–CO conversion. As CH_4 and H_2S react with atomic H to liberate carbon and sulfur, they couple to form carbon monosulfide (CS). Carbon in CS is further oxidized into OCS and eventually ends up in CO through H abstraction, via a pathway such as

$$\begin{aligned}
CH_4 + H &\rightarrow CH_3 + H_2 \\
CH_3 + H &\rightarrow CH_2 + H_2 \\
CH_2 + S &\rightarrow HCS + H \\
HCS + H &\rightarrow CS + H_2 \\
SH + H &\rightarrow S + H_2 \\
S + OH &\rightarrow SO + H \\
CS + SO &\rightarrow OCS + S \\
OCS + H &\rightarrow CO + SH \\
H_2O &\xrightarrow{h\nu} OH + H \\
SH &\xrightarrow{h\nu} S + H \\
S + H_2 &\rightarrow SH + H \\
\text{net: } CH_4 + H_2O &\rightarrow CO + 3H_2.
\end{aligned} \tag{30}$$

Note that there is no net change of sulfur species in the cycle. The rate-limiting reaction in pathway (32) is the carbon-sulfur step $CH_2 + S \rightarrow HCS + H$, which is about three orders of magnitude faster than the pathway without sulfur around

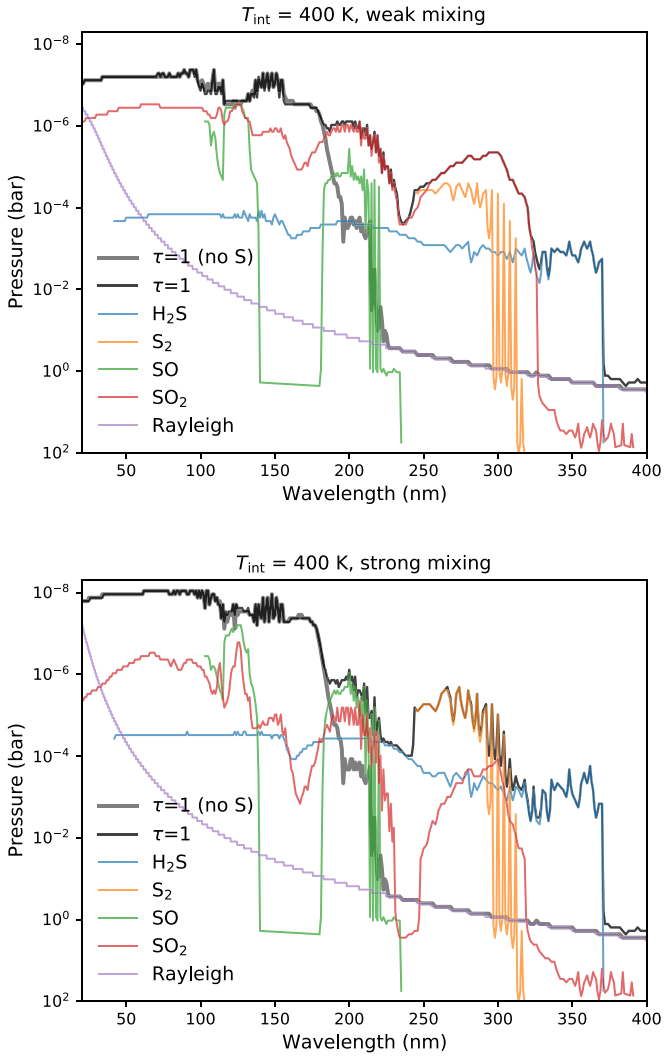

Figure 27. The pressure level of optical depth $\tau = 1$ for GJ 436b with high internal heating ($T_{\rm int}$ = 400 K) while including (black) and excluding (gray) sulfur chemistry, along with the main contribution from sulfur species. The top and bottom panels are for weak and strong vertical mixing.

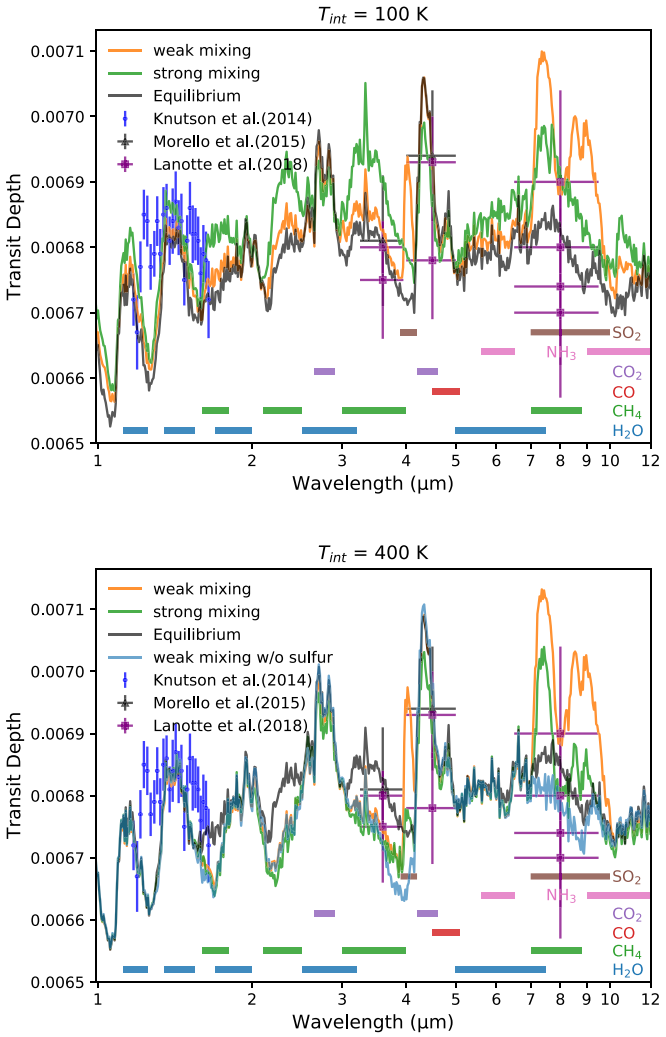

Figure 28. Synthetic transmission spectra computed for our GJ 436b model assuming $T_{\rm int}$ = 100 K (top) and 400 K (bottom) with weak and strong vertical mixing. The model without sulfur chemistry (for $T_{\rm int}$ = 400 K and weak vertical mixing) is also plotted for comparison. The HST/WFC3 points from Knutson et al. (2014) have been shifted down by 200 ppm, following Lothringer et al. (2018). The wave bands of main molecular absorption are indicated.

1 mbar. Interestingly, we find that SH plays an analogous role to H_2O in catalytically converting H_2 to H, causing the minor H increase in Figure 18.

The presence of sulfur species enhances the destruction of methane and might partly contribute to the scarcity of methane detection on hot Jupiters (e.g., Baxter et al. 2021, and references within). H_2S has also been reported to speed up the oxidation of methane in combustion experiments (Gersen et al. 2017), in the oxidizing and high-pressure conditions of gas engines. The decreasing of CH_4 naturally reduces its offspring products to a great extent. The column density shown in Figure 37 reflects the reduction of haze precursors with the participation of sulfur. Based on our fiducial analysis on HD 189733b, we suggest that organic haze formation is likely to be partly suppressed by sulfur kinetics on a hot Jupiter, as opposed to enhanced by sulfur kinetics in a CO_2-rich condition suggested by experimental simulations (He et al. 2020b).

4.2.3. Condensation of Carbon Vapor

Atomic carbon vapor (C) is produced by CO dissociation (including both photodissociation and thermal dissociation in the thermosphere) or the reaction $N + CN \rightarrow C + N_2$ above ~0.1 mbar and also by H abstraction with CH_x species in the lower region. The saturation vapor of C falls off rapidly with decreasing temperature in the upper atmosphere, as shown in Figure 19. In fact, the disequilibrium abundance of C starts to exceed the saturation concentration above 10 mbar. The realistic timescale for graphite growth by condensation involves detailed microphysics and is beyond the scope of this study. As a simple test, we explore the kinetic effects after carbon vapor is fully condensed. We run our HD 189733b model including sulfur chemistry and do not allow C to become supersaturated but simply fix the abundance of C in the gas phase to its saturation mixing ratio. This is physically equivalent to assuming instantaneous condensation and unlimited condensation nuclei.

Figure 19 demonstrates the consequences when C is instantaneously condensed, which mainly impacts the region above 0.1 mbar. Without the condensation of C, CH_4 can be replenished by the hydrogenation sequence of C (i.e., $C \rightarrow CH \rightarrow CH_2 \rightarrow CH_3 \rightarrow CH_4$). This channel is closed as C condensed out and CH_4 is further depleted in the upper atmosphere. CS is reduced

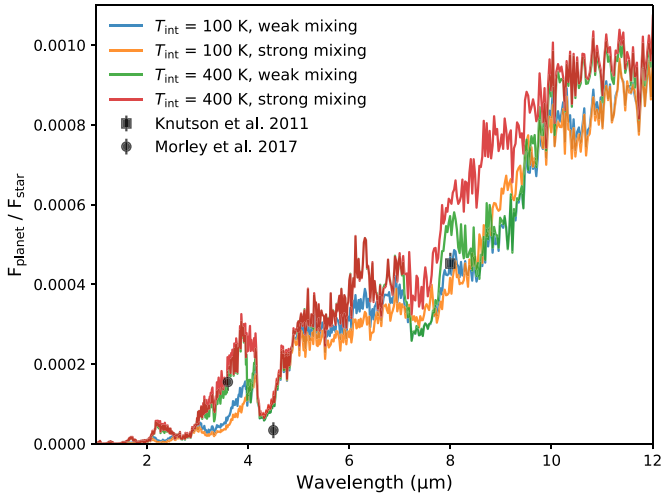

Figure 29. Synthetic emission spectra computed for our GJ 436b models including sulfur chemistry, in comparison with Spitzer secondary-eclipse data.

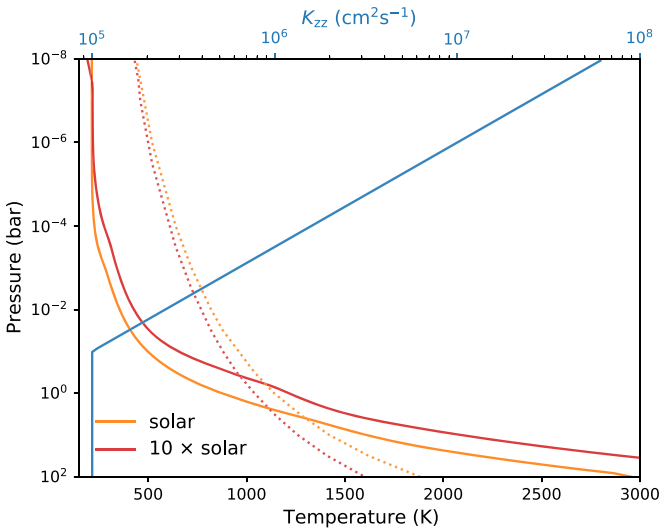

Figure 30. The temperature–pressure and eddy diffusion (K_{zz}) profiles for 51 Eri b, assuming solar and 10 times solar metallicity. The $[CH_4]/[CO] = 1$ equilibrium transition curves corresponding to two metallicities are shown by the dotted curves.

in the same way, but C_2H_2 and HCN remain almost unaffected (they are already reduced compared to the model without sulfur). In the end, we find that the condensation of C has limited effects on other gas compositions in the upper atmosphere.

4.2.4. Transmission Spectra

Here we first take a look at the observational consequences due to model uncertainties among Moses et al. (2011), Venot et al. (2012), and VULCAN that we examined in Section 3.1. Figure 20 showcases the transmission spectra of HD 189733b generated from the compositions computed by VULCAN, Moses et al. (2011), and Venot et al. (2012). The lower quenched abundances of CH_4 and NH_3 in Venot et al. (2012) are responsible for the primary spectral differences, while the spectra from VULCAN and Moses et al. (2011) are fairly close. The ammonia absorption around 8–12 μm could be a useful diagnosis for the quenching mechanism of nitrogen chemistry. Overall, we find that the model uncertainties lead to about half of the spectral deviation caused by disequilibrium chemistry.

We then examine the effects of including sulfur chemistry on the transmission spectra in Figure 21. While the features from sulfur-containing species are almost obscured by other molecules such as H_2O and CH_4 in the near-IR, there are still visible differences due to sulfur's impact on CH_4 and NH_3. Since the coupling to sulfur reduces the abundances of CH_4 and NH_3, the transit depth is smaller in the presence of sulfur. The differences caused by sulfur chemistry are smaller than those between equilibrium and disequilibrium CH_4 and NH_3 abundances but not trivial. Current observations are not capable of placing conclusive constraints, and we need to rely on future facilities with higher resolving power (e.g., JWST, ARIEL).

4.3. GJ 436b

GJ 436b is a Neptune-sized planet in a close orbit around an M dwarf star. This warm Neptune has received tremendous attention since its first discovery (Butler et al. 2004), including multiple primary transit and secondary eclipse observed with Spitzer (Stevenson et al. 2010; Madhusudhan & Seager 2011; Morley et al. 2017 and references within), as well as a transmission spectroscopic study with HST WFC3 (Demory et al. 2007; Knutson et al. 2014). Spitzer 3.6 and 4.5 μm emission indicates that the atmosphere is rich in CO/CO_2 and poor in CH_4. Yet precise constraint and the mechanism on the CO/CH_4 ratio still remain inconclusive. Forward models have suggested that high metallicity (Moses et al. 2013; Morley et al. 2017) and hot interior from tidal heating (Agúndez et al. 2014) can explain the observed CO/CH_4 but are inconsistent with the low water content (less than 10^{-4}) obtained by the retrieval model in Madhusudhan & Seager (2011). Hu et al. (2015) propose that a remnant helium-dominated atmosphere as a result of hydrogen escape can naturally deplete CH_4 and H_2O. However, the Lyα absorption still appears to indicate a hydrogen-dominated atmosphere for GJ 436b (Khodachenko et al. 2019). For this work, we restrict ourselves to 100 times solar metallicity (Neptune-like) and explore the effects of vertical mixing and internal heat with the presence of sulfur.

4.3.1. Model Input

Following the best-fit parameters in Morley et al. (2017), we set up a low and a high internal heating scenario by running HELIOS assuming $T_{int} = 100$ and 400 K, respectively. The stellar UV flux of GJ 436 is adopted from the MUSCLES survey (version 2.2; France et al. 2016; Youngblood et al. 2016; Loyd et al. 2016). The eddy diffusion profile is prescribed by Equation (28) with $P_{tran} = 1$ bar, as where the radiative−convective transition is located in our radiative transfer calculation. We also explore the weak and strong vertical mixing scenarios, based on the GCM simulation by Lewis et al. (2010). The average vertical wind from Lewis et al. (2010) translates to an effective eddy diffusion coefficient from 10^8 cm^2 s^{-1} at 100 bar to 10^{11} cm^2 s^{-1} at 0.1 mbar, assuming the mixing length to be the atmospheric scale height. Since this choice of mixing length generally overestimates the strength of eddy diffusion (Smith 1998; Parmentier et al. 2013; Bordwell et al. 2018), we consider it as the upper limit and set it for the strong vertical mixing scenario. We correspondingly have $K_{deep} = 10^8$ cm^2 s^{-1} for the strong

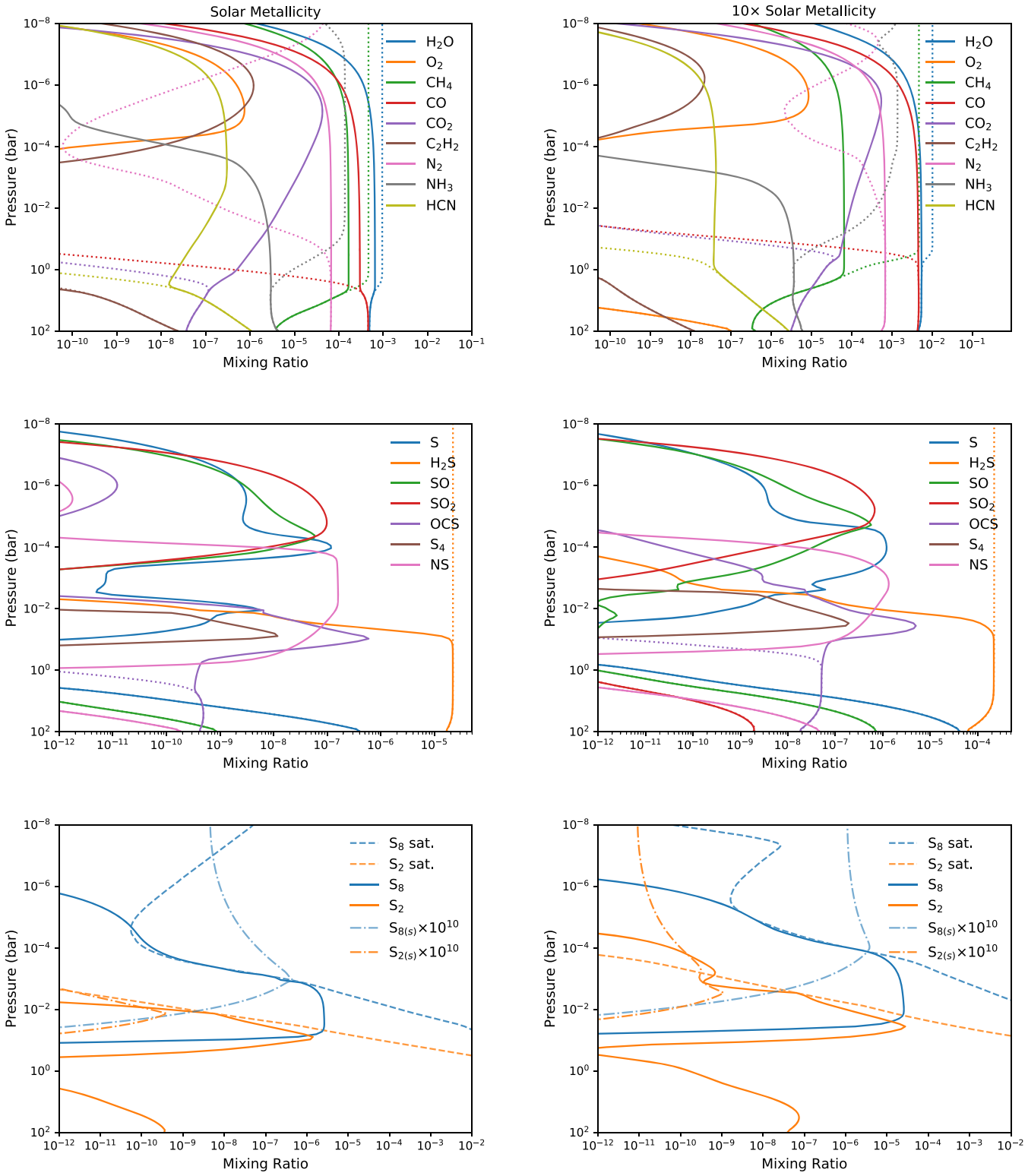

Figure 31. The computed abundance profiles of 51 Eri b, assuming solar (left panels) and 10 times solar (right panels) metallicity. The top row presents the main species, with equilibrium profiles shown in dotted lines. The middle row shows the main sulfur species, and the bottom has S_2/S_8 vapor (solid), S_2/S_8 condensate particles (dashed–dotted), and the saturation mixing ratios of S_2/S_8 (dotted). The particles are plotted in the ratio of the number density of particles to the total number density of gas molecules and multiplied by 10^{10}.

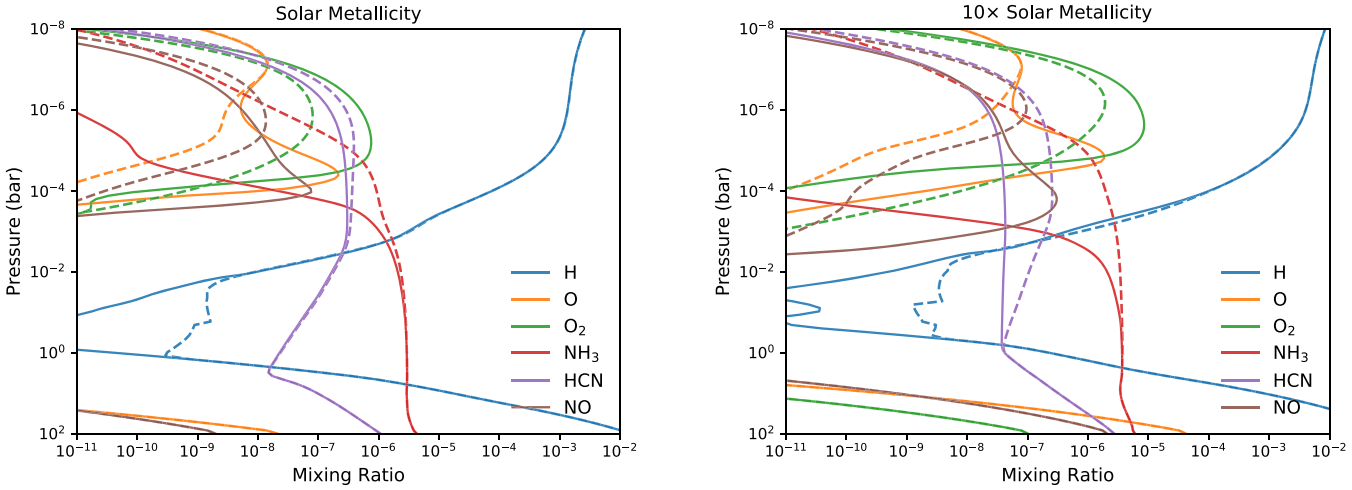

Figure 32. The abundances of several main species that show differences from models including sulfur kinetics (solid) and without sulfur kinetics (dashed) for 51 Eri b.

mixing scenario and assume $K_{\rm deep} = 10^6$ cm^2 s^{-1} for the weak mixing scenario.

4.3.2. Effects of Vertical Mixing and Internal Heating

Resolving the CO/CH$_4$ abundance ratio is the leading question for the atmospheric compositions of GJ 436b. Since we did not vary the elemental abundance, the photospheric abundance of CH$_4$ primarily depends on the quench level, which is controlled physically by the strength of vertical mixing and thermal structures. Figure 22 shows that the 100 times solar metallicity constrains both temperature profiles within the CO-dominated region. As illustrated by the equilibrium profiles in Figure 23, for low internal heating ($T_{\rm int} = 100$ K), the temperature is close to the CH$_4$/CO transition and the equilibrium CH$_4$ abundance oscillates below 10^{-4} bar, whereas the equilibrium CH$_4$ abundance decreases monotonically with increasing pressure from about 10^{-4} bar for high internal heating ($T_{\rm int} = 400$ K). The twisting variation of CH$_4$ with depth was pointed out by Molaverdikhani et al. (2019), suggesting that it can lead to a nonmonotonic correlation with increasing K_{zz} for low internal heating. However, in the physically motivated range of K_{zz} we explored, CH$_4$ is always quenched in the confined region below 1 bar where CH$_4$ increases with depth, as shown in Figure 23. Therefore, stronger vertical mixing produces higher quenched CH$_4$ abundance for low internal heating and conversely produces lower quenched CH$_4$ abundance for high internal heating.

For low internal heating, CH$_4$ remains in considerable amounts in both weak and strong mixing cases, with photospheric CO/CH$_4$ ratio about 25 and 4, respectively. The amount of methane efficiently converts to other hydrocarbons (e.g., C$_2$H$_2$ and C$_6$H$_6$) and HCN, especially in the photochemically active region above 1 mbar. For high internal heating, CH$_4$ abundance is significantly reduced compared to that with low internal heating, regardless of vertical mixing. The photospheric CO/CH$_4$ ratio for weak and strong mixing is about 2000 and 7000. C$_2$H$_2$ and HCN are also diminished with CH$_4$, except CH$_4$ can still be transported to the upper atmosphere in the strong mixing scenario.

For nitrogen species, N$_2$ predominants under high metallicity and quenched NH$_3$ exhibits greater abundances than equilibrium in all cases. The NH$_3$–N$_2$ conversion is slower than CH$_4$–CO, and hence NH$_3$ is quenched deeper than CH$_4$. Photochemically

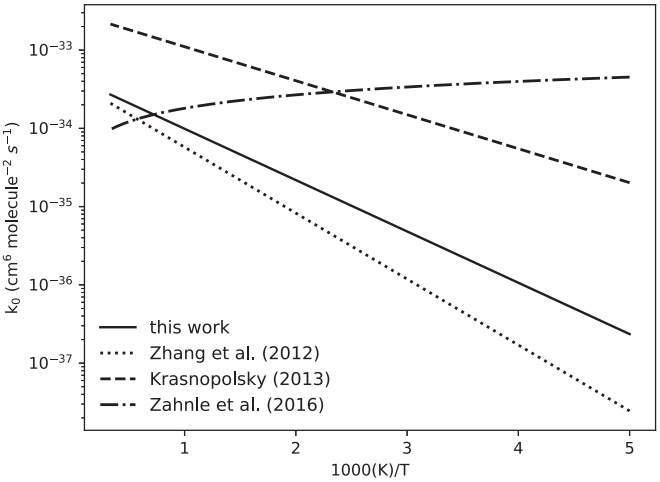

Figure 33. The low-pressure limit rate coefficient of S + CO $\overset{M}{\rightarrow}$OCS estimated in this work (Equation (36)), compared to those in the literature.

produced HCN can take over NH$_3$ and CH$_4$ in the upper atmosphere, but at higher altitude compared to HD 189733b owing to the weaker UV flux of GJ 436. Interestingly, the quench level of NH$_3$ appears to vary little with vertical mixing and mainly responds to the change of internal heating (see the pressure and temperature dependence of NH$_3$–N$_2$ conversion in Tsai et al. 2018). The insensitivity of NH$_3$ to vertical mixing could provide additional constraints to the deep thermal property.

4.3.3. Effects of Sulfur Species

Figure 24 shows the distribution of main sulfur species for each scenario. H$_2$S still remains the major sulfur-bearing molecule. The region where H$_2$S is stable extends to a lower pressure of about 0.1 mbar compared to HD 189733b because of less photochemically produced atomic H on GJ 436b. Above the H$_2$S-stable region, the sulfur species is more diverse than the S/H$_2$S dichotomy in a hot Jupiter. The stratospheric temperature of GJ 436b is too warm for elemental sulfur to grow into large allotropes but allows rich interaction of sulfur and oxygen species in the upper stratosphere. The distribution is sensitive to mixing processes: SO$_2$ takes over H$_2$S for weak vertical mixing, while S, S$_2$, and SO are in turn the leading

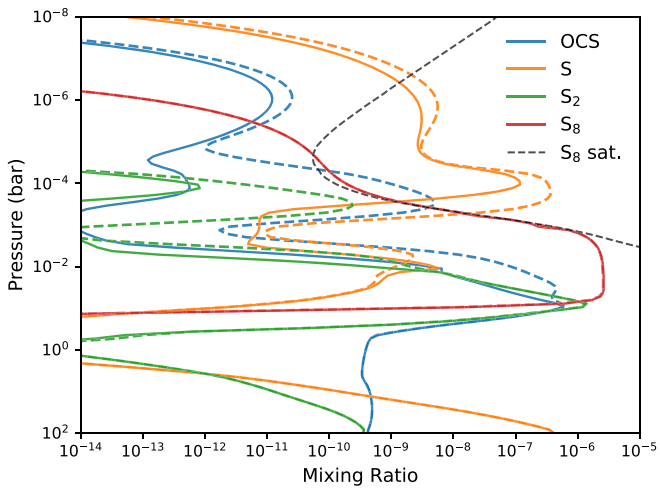

Figure 34. Main sulfur species from our nominal model with solar metallicity (solid) compared to those adopting the faster rate of Equation (35) from Zahnle et al. (2016) (dashed).

sulfur species for strong vertical mixing. Since sulfur species *do not* quench in the deep region like CH_4 and NH_3, they are not affected by internal heating. Instead, sulfur species are more sensitive to photochemical products transported from the upper atmosphere.

Sulfur also impacts other nonsulfur species. Figure 25 compares our models of GJ 436b that include and exclude sulfur chemistry. H is considerably reduced between 0.1 and 10^{-4} bar in the presence of sulfur, opposite to what is seen on HD 189733b. This is because the photolysis of SH that provides the catalytic H production on HD 189733b is absent, as SH is less favored on GJ 436b. Instead, hydrogen is recycled faster by $H + H_2S \rightarrow H_2 + SH$ in the H_2S-stable region of GJ 436b, as indicated in Figure 26. The reduction of H subsequently slows down the production of C_2H_2 and HCN, even when CH_4 abundance is almost unchanged. In the photochemically active region above ~0.1 mbar, atomic C preferably combines with sulfur into OCS or CS, which further lowers C_2H_2 and HCN in the upper atmosphere. As NH_3 being oxidized by atomic O into NO in this region, nitrogen sulfide (NS) accelerates NH_3 oxidization while coupling to sulfur, analogous to the role of HCS for destroying CH_4 on HD 189733b. The catalytic pathway for oxidizing NH_3 is

$$\begin{aligned} NH_3 + H &\rightarrow NH_2 + H_2 \\ NH_2 + S &\rightarrow NS + H_2 \\ NS + O &\rightarrow NO + S \\ \text{net: } NH_3 + H + O &\rightarrow NO + 2H_2. \end{aligned} \quad (31)$$

Similar to HD 189733b, sulfur species raise the UV photosphere longward of 200 nm, as shown in Figure 27. The absorption feature around 200–300 nm reflects the aforementioned sensitivity to vertical mixing, with SO_2 predominating in the weak mixing scenario and SO and S_2 in the strong mixing scenario.

4.3.4. Sensitivity to S_x Polymerization

Since the growth from S_2 to larger sulfur allotropes is suppressed in our GJ 436b model, we perform a sensitivity test to see whether S_x beyond S_2 can be produced with faster polysulfur recombination rates. The three-body recombination reactions that interconvert S_2–S_4–S_8 are the main

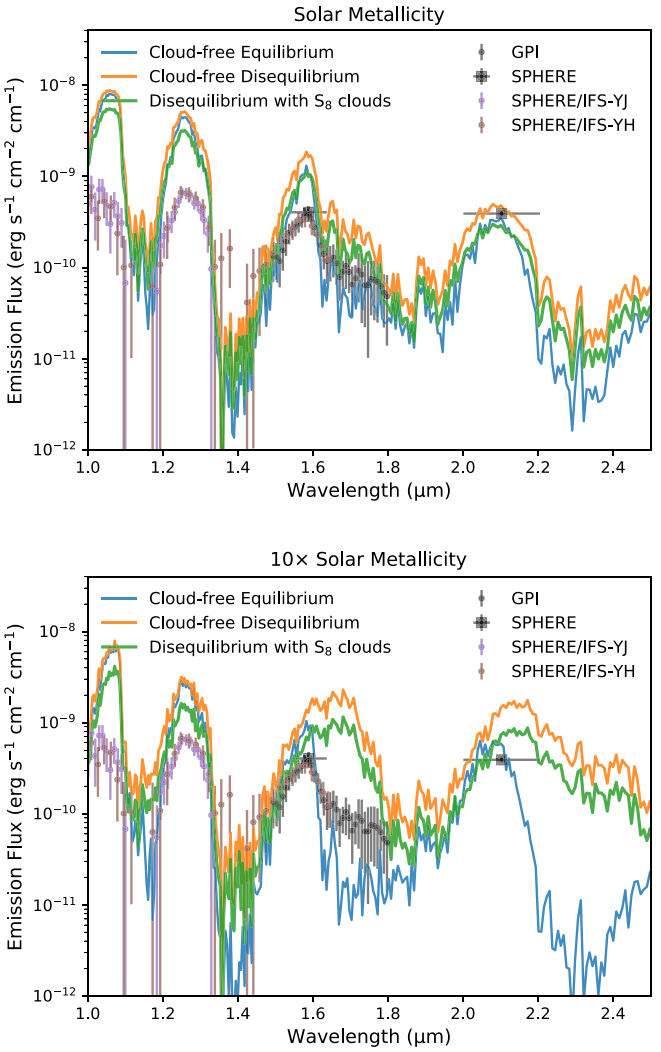

Figure 35. Synthetic emission spectra of 51 Eri b produced from equilibrium abundances, disequilibrium abundances, and with S_8 condensate layer. Data points show GPI observations from Macintosh et al. (2015) and SPHERE observations from Samland et al. (2017).

polymerization steps. We follow Zahnle et al. (2016) and raise the rate of S_4 recombination by 10 and that of S_8 recombination by 100 for a faster polysulfur forming test. We find that the abundances of S_4 and S_8 remain low and almost unchanged. We confirm that the stratosphere of GJ 436b is too warm for elemental sulfur to grow beyond S_2 into fair quantities, even after taking into account the uncertainties in the sulfur polymerization rates.

4.3.5. Transmission and Emission Spectra

The observational indication in transmission spectroscopy of varying vertical mixing and internal heating for GJ 436b is shown in Figure 28. The early analysis of Spitzer data (Knutson et al. 2011) has shown interepoch variability, which is reduced in the investigation of Lanotte et al. (2014) and Morello et al. (2015). Methane absorption at 2.1–2.5 μm and 3–4 μm and sulfur dioxide absorption at 7–10 μm are the most promising diagnostic features. For $T_{\rm int} = 100$ K, vertical mixing leads to higher CH_4 abundance, and the strong mixing scenario can be marginally ruled out by the Spitzer 3.6 μm data. For $T_{\rm int} = 400$ K, vertical mixing conversely reduces CH_4 abundances,

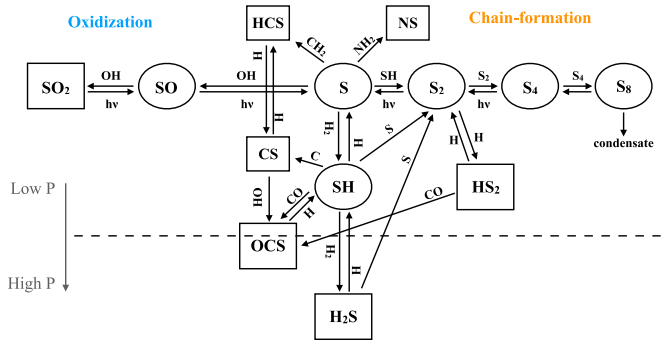

Figure 36. A schematic diagram illustrating the main pathways for sulfur kinetics in an H_2-dominated atmosphere. The dashed line represents the transition from the lower region where sulfur is predominantly locked in H_2S to the upper region where H_2S is subject to dissociation. Rectangles indicate stable species, whereas ellipses indicate active radical or intermediate species.

confirmed with previous work by Agúndez et al. (2014) and Morley et al. (2017). The 3.6 and 4.5 μm Spitzer data are consistent with our models under weak/strong vertical mixing or in chemical equilibrium. While CH_4 is not sensitive to the strength of vertical mixing at high internal heating scenario, SO_2 shows strong dependence on mixing processes and is favored in our weak mixing scenario, which can potentially be detectable by JWST/MIRI. In addition, S_2 is more favored with strong vertical mixing and provides strong absorption features in the UV.

Figure 29 shows the synthetic emission spectra for GJ 436b compared to Spitzer observations. While the 3.6 μm data prefer the $T_{\rm int} = 400$ K models, $T_{\rm int} = 100$ K models are favored by the 8 μm data. On the other hand, the already large column abundance of CO makes the thermal emission at 4.5 μm insensitive to internal heating or vertical mixing. The models somewhat overpredict the flux at 4.5 μm, as in the previous study (Morley et al. 2017).

We conclude that our models demonstrate and confirm that the combination of moderately high ($\gtrsim$100 times) solar metallicity and internal heating can explain the low CH_4/CO ratio loosely constrained by the Spitzer 3.6 and 4.5 μm observations, regardless of the strength of mixing. Sulfur species do not quench in the deep region like CH_4 or NH_3 but closely associate with photolysis and mixing processes in the upper stratosphere. The independence from the thermal property of the interior makes sulfur chemistry a complementary avenue for characterizing GJ 436b, in conjunction with the long-standing quest for constraining CH_4/CO.

4.4. 51 Eridani b

51 Eridani b (51 Eri b) is a young Jupiter-mass giant around an F-type star at a wide orbit. Unlike irradiated hot Jupiters, the residual heat from the formation predominates over the stellar flux. In the discovery work, Macintosh et al. (2015) suggest that 51 Eri b has an effective temperature of 550–750 K with vertically quenched CH_4 and CO. Water vapor should not condense owing to its heat at depth, in contrast to our colder Jupiter. The combination of the hot interior and photochemically active stratosphere makes 51 Eri b a unique test bed for atmospheric chemistry, as explored by Zahnle et al. (2016) and Moses et al. (2016).

4.4.1. Model Setup

We adopt $T_{\rm eff} = 760$ K as suggested by the retrieval work of Samland et al. (2017) for calculating the temperature profile of 51 Eri b (although we find little difference between setting $T_{\rm eff} = 760$ K and $T_{\rm eff} = 700$ K as assumed in previous work; Moses et al. 2016; Zahnle et al. 2016). Samland et al. (2017) also derive a 10 times supersolar metallicity based on the K-band emission. To explore the effects of metallicity, we construct one temperature profile with solar metallicity and one with 10 times solar metallicity. The resulting P–T profiles are shown in Figure 30. We did not include a thermosphere, as Moses et al. (2016) have added an arbitrary 1000 K inversion layer above 1 μbar but found little effects on the chemistry. The eddy diffusion takes the same form as Equation (28), with the radiative−convective transition $P_{\rm tran}$ and $K_{\rm deep}$ set to 0.1 bar and 10^5 cm^2 s^{-1}, respectively.

The stellar UV flux of 51 Eridani is assembled from various sources. The observations from the International Ultraviolet Explorer (IUE)[19] cover the wavelength range between 115 and 198 nm. The EUV flux ($\lambda < 115$ nm) is adopted from the synthetic spectrum of HR 8799 (Sanz-Forcada et al. 2011),[20] following Moses et al. (2016). For wavelengths greater than 198 nm, we use a theoretical stellar spectrum with a close temperature from ATLAS9 Model Atmosphere Database[21] by the BOSZ stellar atmosphere model (Bohlin et al. 2017), assuming $T_{\rm eff} = 7250$ K, $\log(g) = 4$, $\log[{\rm Fe/H}] = 0$, and radius $= 1.45\ M_\odot$. The stellar irradiation received by the planet in our 51 Eridani model is stronger by about 50% than in previous work, since the orbit has been updated from 13–14 au to 11.1 au according to De Rosa et al. (2020).

4.4.2. Disequilibrium Chemistry Compared with Previous Work

Zahnle et al. (2016) investigate sulfur hazes in the atmosphere of 51 Eri b. Moses et al. (2016) use an extensive N–C–H–O chemical network (~1650 reactions), which include more complex hydrocarbons, to study the quenching and photochemical effects. The mixing ratios of the main species in our 51 Eri b model for solar and 10 times solar metallicity are displayed in the top left panel of Figure 31. The main C, H, N, and O chemical species in our model are overall consistent with both Zahnle et al. (2016) and Moses et al. (2016), which we summarize in the following paragraph.

The top row of Figure 31 shows how disequilibrium processes control the composition distribution. First, CH_4–CO conversion is quenched at about 1 bar; thus, CO predominates over CH_4. Likewise, N_2 is the predominant nitrogen-bearing species over NH_3. Second, without a fast recycling mechanism like that on a hot Jupiter, strong photolysis of water makes the upper atmosphere oxidizing and produces considerable CO_2 and O_2. Third, C_2H_2 and HCN are photochemically generated in the upper atmosphere, similar to hot Jupiters. While C_6H_6 is produced to about the 10 ppb level in Moses et al. (2016), C_6H_6 is greatly reduced in our model including sulfur, as seen for GJ 436b.

The most outstanding difference between Zahnle et al. (2016) and our model in terms of sulfur chemistry is that S_8 reaches a condensable level in our atmosphere. Although produced at about the same level, S_8 is close to saturation but

[19] https://archive.stsci.edu/iue/
[20] http://sdc.cab.inta-csic.es/xexoplanets
[21] https://archive.stsci.edu/prepds/bosz/

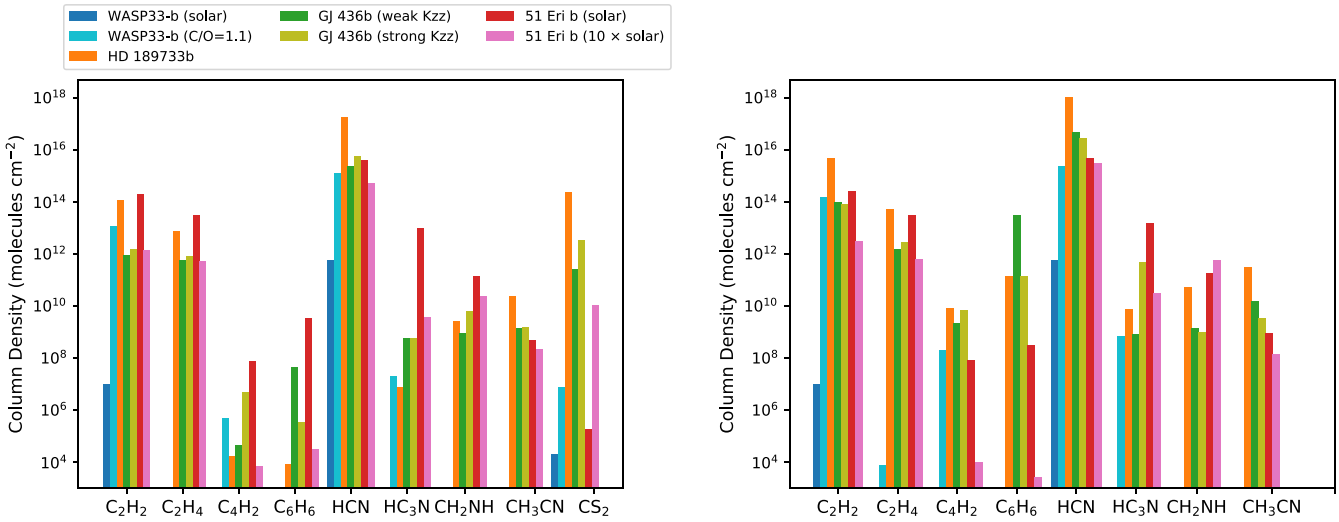

Figure 37. The column number densities (molecules cm^{-2}) above 1 mbar of haze precursors for the simulated atmospheres in Section 4, including sulfur (left) and without sulfur (right). Some molecule abundances are negligible and not shown for WASP-33b. For GJ 436b, the models with $T_{\rm int} = 400$ K and weak/strong vertical mixing are used.

does not condense in the nominal model of Zahnle et al. (2016). Since we adopt the same saturation vapor pressure of sulfur allotropes (Lyons 2008) as Zahnle et al. (2016), the different condensation behavior should be due to a warmer upper stratosphere in Zahnle et al. (2016). Zahnle et al. (2016) indeed noted that S_8 would condense if the temperature were just a few degrees lower.

4.4.3. Effects of Supersolar Metallicity

The left and right columns of Figure 31 compare the results of solar and 10 times solar metallicity. The model with 10 times solar metallicity has slightly hotter troposphere (Figure 30), which favored CO over CH_4. Although the equilibrium abundance of CH_4 in the stratosphere is increased in the 10× solar metallicity model, CH_4 is in fact decreased with a lower CH_4/CO ratio at the quench level. In the end, the 10× solar metallicity model shows higher CO, CO_2, and H_2O and lower CH_4 abundances, which in turn reduces other hydrocarbons as well. The mixing ratio of CO_2 exceeds CH_4 for 10× solar metallicity and can reach ∼0.1% in the upper atmosphere. The production of O_2 also rises with metallicity following the increase of water.

4.4.4. Effects of Sulfur

Compared to HD 189733b and GJ 436b, H_2S can only remain stable against hydrogen abstraction (29) at higher pressure of about 0.05 bar. The reverse rate of Equation (29) significantly drops in the cooler stratosphere of 51 Eri b and prohibits the reformation of H_2S. The active SH radical produced by H_2S leads to a rich variety of sulfur species, as illustrated in the middle row of Figure 31. Compared to Zahnle et al. (2016), our model exhibits a more oxidized upper stratosphere due to stronger UV irradiation from the closer orbit in our setting (11.1 au compared to 13.2 au). Nonetheless, both models predict efficient polymerization forming a great abundance of S_8. Since S_8 is the end pool of sulfur chain reactions, we find that the condensation of S_8 does not affect other sulfur species. Elemental S is still the leading sulfur species above the S_8 condensing layers until being oxidized into SO and SO_2 in the upper stratosphere.

The equilibrium abundance of H_2S scales with metallicity, which leads to more production of S_8 vapor as metallicity increased. The 10 times solar metallicity model has slightly warmer temperature, which allows higher saturation pressure of sulfur as well. In the end, both the gas and condensates of S_2 and S_8 increase with metallicity.

The effects of coupling to sulfur on other species are highlighted in Figure 32. The most remarkable feature is the enhanced oxygen abundances in the upper atmosphere with sulfur. In the absence of sulfur, atomic O can be released from H_2O with the aid of CO_2:

$$\begin{aligned} H_2O &\xrightarrow{h\nu} OH + H \\ CO + OH &\rightarrow CO2 + H \\ CO_2 &\xrightarrow{h\nu} CO + O \\ \text{net: } H_2O &\xrightarrow{2h\nu} H + O. \end{aligned} \tag{32}$$

While sulfur is present, SO and SO_2 dissociate more than CO_2 around Lyα and provide a faster channel to liberate O from H_2O:

$$\begin{aligned} H_2O &\xrightarrow{h\nu} OH + H \\ SO + OH &\rightarrow SO2 + H \\ SO_2 &\xrightarrow{h\nu} SO + O \\ \text{net: } H_2O &\xrightarrow{2h\nu} H + O \end{aligned} \tag{33}$$

or

$$\begin{aligned} H_2O &\xrightarrow{h\nu} OH + H \\ S + OH &\rightarrow SO + H \\ SO &\xrightarrow{h\nu} S + O \\ \text{net: } H_2O &\xrightarrow{2h\nu} H + O. \end{aligned} \tag{34}$$

The excess atomic O readily reacts with OH to form O_2. This enhanced oxidized region along with NS accelerates the

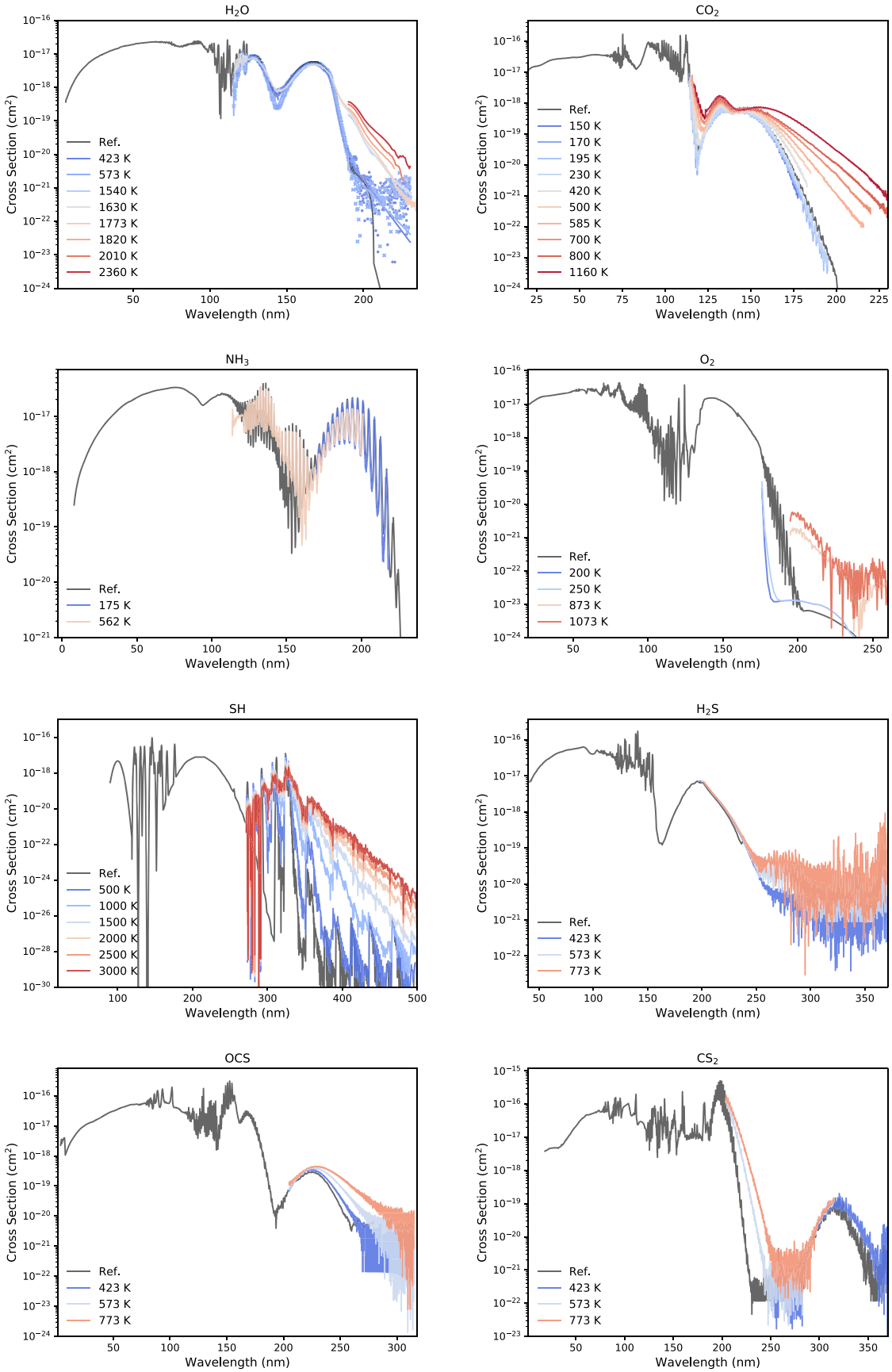

Figure 38. Photoabsorption cross sections of H_2O, CO_2, and NH_3 across various temperatures, with Ref. denoting the cross sections measured at room temperature. The measured cross sections of H_2O at 423 K (circle) and 573 K (cross) are noisy beyond 216 nm, and we use linear fit for conservative estimate. The references of the cross sections are described in Section 2.5

oxidization of NH_3, via the same pathway (31) but more pronounced than that on GJ 436b. On the other hand, CH_4 is unaffected because the intermediates HCS and CS are deficient in the colder stratosphere of 51 Eri b. Lastly, the coupling to H_2S also helps atomic H recycle back to H_2 faster, as seen on GJ 436b.

4.4.5. Sensitivity to OCS Recombination

The fate of elemental S after being released from H_2S is critical in sulfur kinetics. Several reactions potentially control whether S proceeds to chain formation into larger polysulfur (S_x), forming OCS, or being oxidized to SO, SO_2. To address the effects of kinetics uncertainties, Zahnle et al. (2016) explore the sensitivity to H_2S recombination and S_x polymerization. The authors found that a faster H_2S recombination counteracts the destruction of H_2S and reduces the production of S_8, while their results are not sensitive to the polymerizing rates of forming S_4 and S_8 within the tested ranges. We have tested the polymerization rates for GJ 436b and confirmed its general insensitivity to S_8 formation. For 51 Eri b, we recognize that the recombination of OCS

$$S + CO \xrightarrow{M} OCS \tag{35}$$

could be important in determining the oxidizing rate of sulfur. The rate coefficient of reaction (35) has in fact not been measured. Only the reverse step of reaction (35), the dissociation of OCS, has available data at high temperatures. Recently, Ranjan et al. (2020) have also identified this reaction to modestly alter the CO abundance in a CO_2–N_2 atmosphere and advocate laboratory investigation. Here, we will explain how the rate coefficient of reaction (35) is estimated in our nominal model and then explore the sensitivity to the uncertainty for 51 Eri b.

Reaction (35) is a spin-forbidden reaction and usually many orders of magnitude slower than a typical three-body reaction. Since the measured high-temperature dissociation reaction has a high activation energy, extrapolating the dissociation reaction (the reversal of reaction (35)) to low temperatures will result in unrealistic rates. Instead, we estimate the activation energy from the well-studied analogous reaction, $O + CO \xrightarrow{M} CO_2$. The pre-exponential factor is then determined by matching the reverse of dissociation reaction at 2000 K from Oya et al. (1994). The low-pressure limit rate of reaction (35) we estimate is

$$k_0 = 4.47 \times 10^{-34} \exp(-1510/T). \tag{36}$$

We compare the rate coefficient (36) with those assumed in Zahnle et al. (2016) and Venus literature (Zhang et al. 2012; Krasnopolsky 2013) in Figure 33. The reaction rates show diverse values especially toward lower temperatures, the relevant temperature range for the stratosphere of 51 Eri b. Taking into account the uncertainty of the reaction rate adopted in each model, the rate constants in Zhang et al. (2012), Krasnopolsky (2013), and this work exhibit consistent temperature dependence from 1000 to 200 K, whereas that in Zahnle et al. (2016) has surprisingly almost no temperature dependence. Since the rate constant of reaction (35) from Zahnle et al. (2016) is the most different from the literature and yields the fastest OCS forming rate, we will use the rate from Zahnle et al. (2016) as the upper limit to test the sensitivity.

We run our nominal model with solar metallicity but adopt the rate constant of Equation (35) from Zahnle et al. (2016). The effects of faster OCS recombination are illustrated in Figure 34. With the OCS recombination rate from Zahnle et al. (2016), OCS mixing ratio is significantly increased above 0.1 bar. S_8 is slightly reduced but remains the major sulfur carrier between 10^{-2} and 10^{-4} bar, consistent with the model results in Zahnle et al. (2016). The abundances of S and S_2 are subsequently affected by more ample OCS photodissociation, but that of S_8 remains the same as set by condensation. Given these differences, we reiterate further investigation to pin down the reaction rate of OCS recombination.

4.4.6. Emission Spectra

Figure 35 demonstrates the effects of disequilibrium chemistry and S_8 clouds on the planetary emission spectra. For both metallicities, quenched CH_4 and H_2O have lower abundances than equilibrium, leading to higher emission in the *H* and *J* bands from the deeper region. The 10 times solar metallicity further reduces CH_4 and prompts the flux at 1.6–1.8 μm. We assume 1 μm particle size for S_8 condensates, which scatter strongly and reduce the emission in this wavelength range. However, using the higher effective temperature and metallicity from Samland et al. (2017), our models generate emission that is too high in the *H* and *J* bands and fail to reproduce the observed spectra. We conclude that $T_{\rm eff}$ is lower than that determined by Samland et al. (2017) and/or additional cloud layers (e.g., Moses et al. 2016) are required to match the lower observed emission.

4.5. Sulfur Mechanism

Figure 36 summarizes the important pathways for sulfur species in the irradiated H_2-dominated atmospheres we explored in this section. H_2S is the dominant molecule, which is thermochemically stable for a wide range of temperatures in the lower atmosphere followed by OCS. The photochemistry of sulfur is initiated from SH and S produced by H_2S dissociation, leading to multiple channels including chain formation and oxidization depending on the atmospheric condition. Sulfur chain formation is highly temperature sensitive where S_2 is favored at about 600–800 K and S_8 can only form below ~500 K (e.g., the stratosphere of 51 Eri b). When OH is sufficiently produced by H_2O photolysis, S will most likely be oxidized into SO and SO_2 in the upper atmosphere. S also participates in accelerating CH_4 and NH_3 destruction via the coupling to CH_2 or NH_2, as seen in our HD 189733b and GJ 436b models.

4.6. Trends of Photochemical Hazy Precursors

Figure 37 summarizes the column densities of haze precursors above 1 mbar for the simulated atmospheres in Section 4. Across the various irradiated H_2-dominated atmospheres we explored, we find HCN consistently to be the most prevailing precursor. This is not surprising, as HCN is a robust photochemical product of CH_4 and NH_3 and also has recently been detected on HD 209458b (Giacobbe et al. 2021). Nonetheless, it does not necessarily imply that HCN will lead to complex nitrile formation, since HCN is not the limiting factor as we discussed in Section 2.8. A more careful assessment at high temperatures is required before extrapolating the haze-forming mechanism below

200 K on Titan. We observe a general increasing trend with decreasing temperature for the more indicative nitrile precursors HC_3N but the opposite for CH_3CN. The same trend is seen for the hydrocarbon precursors C_4H_2 and C_6H_6.

Only HCN and C_2H_2 can reach appreciable levels on WASP-33b, even as photochemical hazes are not expected on WASP-33b. For GJ 436b, most of the precursors are not too sensitive to eddy diffusion. For 51 Eri b, almost all precursors are reduced with increasing metallicity, except for CS_2, since it contains no H. In fact, CS_2 is most favored on HD 189733b, which suggests that sulfur-containing hazes in the hot Jupiter condition as carbon and sulfur can couple closely. In addition to sulfur condensates, 51 Eri b might also be covered by nitrile-type hazes according to the precursor distribution.

5. Discussion

5.1. High-temperature UV Cross Sections

We have implemented layer-by-layer UV cross sections according to the temperature at each atmospheric level in VULCAN. Due to the sparsely available data, we did not perform systematic study in this work. Nonetheless, we have gained some insights through the case studies in Section 4.

We found that the effects of temperature dependence for H_2O are mostly negligible in an H_2-dominated atmosphere. However, this is solely based on the limited wavelength range measurements we assembled. For the high-temperature ($T > 1000$ K) cross sections, only wavelengths longer than about 190 nm are included (Figure 38). The high-temperature cross sections in the FUV could have larger effects.

We confirm the analysis in Venot et al. (2013) that although the CO_2 abundance is not directly influenced by the temperature dependence of CO_2 photolysis, the shielding effects can impact other species. As CO_2 absorbs more strongly with increasing temperature, the UV photosphere is lifted to lower pressure. The production of radicals, such as H and OH, is reduced and subsequently alters other species. However, we also find that the shielding effects of CO_2 are completely shadowed when sulfur species are included (e.g., see the right panel of Figure 18). The temperature dependence of CO_2 photolysis should be more amplified in CO_2-dominated atmospheres.

5.2. Implication of Ionization

Ions are not included in this work. We are working on including ion chemistry in the next update of VULCAN. Photoionization is known to be critical in initiating the haze formation (Wong et al. 2003; Krasnopolsky 2009; Plessis et al. 2012; Lavvas et al. 2013). Even thermoionization can be important for ultrahot Jupiters. In our study about WASP-33b, atomic Ti and V in the upper atmosphere are expected to be partly ionized and contribute to free electrons. Since Ti has an ionization threshold of 180 nm, compared to about 240 nm for Na, the effects of photoionization on Ti and V should be similar to and probably smaller than those on the alkali atoms, as investigated in Lavvas & Koskinen (2017). An important outcome of photoionization is that the increased electrons can lead to more hydrogen anions (H-) than predicted by thermal equilibrium, which are found to be important opacity sources in some hot Jupiter atmospheres (Lewis et al. 2020). In terms of sulfur chemistry, several sulfur species have relatively lower energy threshold of ionization and can be subject to photoionization. For example, atomic S starts to ionize from Lyα. Since S is likely the dominant sulfur species in the hot Jupiter's stratosphere (Section 4.2.2), S can be photoionized and ramify into various organic molecules through ion-exchange reactions.

5.3. More Intriguing Questions about Sulfur

In Section 4, we find that the coupling to sulfur chemistry impacts the core C–H–N–O kinetics in several ways for H_2-dominated atmospheres. The coupling effects essentially depend on whether the sulfur-containing intermediates are active, which is not well understood in general, as it can vary with atmospheric conditions such as temperature and bulk compositions. Gersen et al. (2017) find that CH_3S and CH_3SH provide more efficient pathways for methane oxidization in the combustion (oxidizing) environment. He et al. (2020a) also observe the photochemical formation of CH_3S and CH_3SH in a CO_2-rich gas mixture in the experiments. Although we have included reactions involving CH_3S and CH_3SH in our sulfur mechanism, they are not identified to be important in the pathway analysis for all of the H_2-dominated atmospheres we investigated. The chemical role of CH_3SH is worth further study in the broad context of biologically produced sulfur.

The temperature profiles are fixed without considering the radiative feedback in this whole work. The radiative effects might be more prominent in the presence of sulfur, such as the absorption of SH and S_2 in the optical and NUV. 51 Eri b or other directly imaged planets with a relatively cold stratosphere ($\lesssim$500 K) and under sufficient UV irradiation sit in the sweet spot for testing the radiative feedback on sulfur condensates.

6. Summary

In this paper, we present a thorough theoretical framework of the updated photochemical code VULCAN. We validate our models for the atmospheres of hot Jupiters, Jupiter, and modern Earth and carry out comparative studies on representative cases of extrasolar giant planets: WASP-33b, HD 189733b, GJ 436b, and 51 Eridani b. The highlights of our results are as follows:

1. We have carefully validated the model of HD 189733b. The updated methanol scheme in Venot et al. (2020) is found to bring the quenching behavior of methane close to Moses et al. (2011) and VULCAN. We pointed out that the photochemical source plays a nontrivial part in the model differences between Moses et al. (2011), Venot et al. (2012), and VULCAN.
2. We demonstrate that advection transport in the downdraft can qualitatively explain the deep ammonia distribution in Jupiter, which cannot be explained by eddy diffusion alone.
3. The implementation of surface boundary conditions and condensation in an oxygen-rich atmosphere is validated in the present-day Earth model. A general oxidation timescale analysis is provided for assessing the chemical lifetime of biosignature gases.
4. The atmosphere of WASP-33b is not affected by vertical quenching but consisted of an upper photolytic region and a thermochemical equilibrium region below. For GJ 436b, we find that NH_3 is insensitive to vertical mixing and the sulfur species governed by photolysis and mixing in the upper stratosphere are independent of the deep

thermal structure, which can be complementary to the CH_4/CO metric for breaking degeneracies. The quenched CO always predominates over CH_4 on 51 Eri b, and sulfur aerosols (chiefly S_8) condense out in the stratosphere.

5. We find that the coupling to sulfur chemistry impacts C–H–N–O kinetics. Sulfur can provide catalytic paths to destroy CH_4 and NH_3 and generally lower the hydrocarbon abundances. H_2S makes H recycled back to H_2 faster on the cooler GJ 436b and 51 Eri b. The dissociation of SO and SO_2 also makes the upper atmosphere of 51 Eri b more oxidizing.
6. We suggest including several photochemical haze precursors such as C_6H_6 and HC_3N, which are more indicative than the commonly considered HCN and C_2H_2. We observe a general increasing trend with decreasing temperature for C_4H_2, C_6H_6, and HC_3N but the opposite for CH_3CN.

S.-M.T. gratefully thanks M. Zhang for customizing PLATON to read nonequilibrium compositions. S.-M.T. also thanks O. Venot and J. Moses for sharing the output of HD 189733b for model comparison, C. Li for providing the retrieved ammonia results from Juno measurements, L. M. Lara for fruitful discussions about setting up photochemistry, P. Rimmer for the compiled observational data of Jupiter, and N. Wogan for pointing out a typo in Equation (14) in an earlier version of this paper. S.-M.T. acknowledges support from PlanetS National Center of Competence in Research (NCCR) and University of Oxford. M.M. acknowledges support from NASA under XRP grant No. 18-2XRP18_2-0076. E.K.L. acknowledges support from the University of Oxford and CSH Bern through the Bernoulli fellowship. K.H. acknowledges support from the PlanetS National Center of Competence in Research (NCCR) of the Swiss National Science Foundation and the European Research Council Consolidator grant EXOKLEIN (No. 771620). This work was supported by the European Research Council Advanced grant EXOCONDENSE (No. 740963).

Software: Python; Numpy (van der Walt et al. 2011); Scipy (Oliphant 2007); Matplotlib (Hunter 2007).

Model availability

In addition to the public code, the configuration files used for the models in Section 3 are available at https://github.com/exoclime/VULCAN, and the main model output in Sections 3 and 4 can be found in the supplementary material.

Appendix A
Molecular Diffusion and Thermal Diffusion Factor

For H_2-based atmospheres, we take

$$D_{H_2-CH_4} = 2.2965 \times 10^{17} T^{0.765}/N \quad \text{(A1)}$$

from Marrero & Mason (1972) as the reference and scale the molecular diffusion coefficient of H_2 with other species according to Equation (3). The thermal diffusion factors for H and He are approximately $\alpha_H \approx -0.1$ and $\alpha_{He} \approx 0.145$ (Moses et al. 2000). We assume $\alpha_i = -0.25$ for the rest of the species based on rigid sphere approximation (Banks & Kockarts 1973).

For N_2-based atmospheres, we take

$$D_{N_2} - CH_4 = 7.34 \times 10^{16} T^{0.75}/N \quad \text{(A2)}$$

from Banks & Kockarts (1973) as the reference and scale the molecular diffusion coefficient of N_2 with other species according to Equation (3). The thermal diffusion factor of Ar is $\alpha_{Ar} \approx 0.17$, and $\alpha_i = -0.25$ for the rest of the species.

For CO_2-based atmospheres, we take

$$D_{CO_2} - H_2 = 7.51 \times 10^{16} T^{0.759}/N \quad \text{(A3)}$$

from Banks & Kockarts (1973) as the reference and scale the molecular diffusion coefficient of CO_2 with other species according to Equation (3). The thermal diffusion factor of Ar is $\alpha_{Ar} \approx 0.17$, and $\alpha_i = -0.25$ for the rest of the species.

Table A1
Full List of Photolysis Reactions in VULCAN

Photolysis	Reaction	Threshold (nm)	Temp. Dependence (K)	Reference Cross Sections/Quantum Yields (λ in nm)
H_2O	$\rightarrow H + OH$	207	300, 423, 573, 1230, 1540, 1630, 1820, 2010, 2360	a, b, e/d, Stief et al. (1975); Slanger & Black (1982)
	$\rightarrow H_2 + O(^1D)$			
	$\rightarrow O + H + H$			
CH_4	$\rightarrow CH3 + H$	145	···	a/d ($\lambda < 97.7$), Gans et al. (2011) ($\lambda \geqslant 118.2$)
	$\rightarrow {}^1CH_2 + H_2$			
	$\rightarrow {}^1CH_2 + H + H$			
	$\rightarrow CH + H_2 + H$			
CH_3	$\rightarrow CH + H_2$	220	···	a/Lavvas et al. (2008); Kassner & Stuhl (1994)
	$\rightarrow CH2 + H$			
CH_2	$\rightarrow CH + H$	275	···	a/a
CO	$\rightarrow C + O$	166	···	a, b/a
H_2	$\rightarrow H + H$	120	···	a/a
C_2H_2	$\rightarrow C2H + H$	217	···	a/a, Okabe (1983)
CO_2	$\rightarrow CO + O$	202	150, 170, 195, 230, 300, 420, 500, 585, 700, 800, 1160	a, Venot et al. (2018) , e/b
	$\rightarrow CO + O(^1D)$			
C_2H_4	$\rightarrow C_2H_2 + H_2$	195	···	a/Lavvas et al. (2008) and references therein
	$\rightarrow C_2H_2 + H + H$			
	$\rightarrow C_2H_3 + H$			
C_2H_6	$\rightarrow C2H4 + H_2$	165	···	a/b, Lias et al. (1970) ($104 < \lambda < 105$)
	$\rightarrow C_2H_4 + H + H$			
	$\rightarrow C_2H_2 + H_2 + H_2$			
	$\rightarrow CH_4 + {}^1CH_2$			
	$\rightarrow CH_3 + CH_3$			
C_4H_2	$\rightarrow C_2H_2 + C_2$	197	···	a/Lavvas et al. (2008)
C_6H_6	$\rightarrow C6H5 + H$	206	···	a/Est. from Kislov et al. (2004)
	$\rightarrow C_3H_3 + C_3H_3$			
OH	$\rightarrow O + H$	265	···	a/a, b ($\lambda < 91$)
HCO	$\rightarrow H + CO$	656	···	a/a
H_2CO	$\rightarrow H_2 + CO$	360	···	a/b ($\lambda < 250$), d
	$\rightarrow H + HCO$			
CH_3OH	$\rightarrow CH_3 + OH$	220	···	a/b, Hagege et al. (1968)
	$\rightarrow H_2CO + H_2$			
	$\rightarrow CH_3 + H$			
CH_3CHO	$\rightarrow CH4 + CO$	350	···	a/b
	$\rightarrow CH_3 + HCO$			
N_2	$\rightarrow N + N$	150	···	a ($\lambda < 100$), c ($\lambda > 120$)/a
NH_3	$\rightarrow NH2 + H$	226	175, 300, 562	a/b
	$\rightarrow NH + H + H$			
HCN	$\rightarrow H + CN$	179	···	a/Nuth & Glicker (1982)
NO	$\rightarrow N + O$	20_2		a/a
NO_2	$\rightarrow NO + O$	398		b, Voigt et al. (2002)/b, d
NO_3	$\rightarrow NO2 + O$	703	···	b/b, Sander et al. (2015)
	$\rightarrow NO + O2$			
N_2O	$\rightarrow NO + O(^1D)$	340	300, 714, 833, 1000, 1250, 1667, 2000	a,c (Zuev & Starikovskii 1990))/b
HNO_2	$\rightarrow NO + OH$	591	···	b/b
HNO_3	$\rightarrow NO_2 + OH$	598	···	b/b
N_2O_5	$\rightarrow NO3 + NO2$	500	···	b/b (from here)
	$\rightarrow NO_3 + NO + O$			
N_2H_4	$\rightarrow N_2H_3 + H$	291	···	c (BiehlStuhl(1991) and Vaghjiani(1993) 296K 191-291n)/Lavvas et al. (2008)
O_2	$\rightarrow O + O$	240	200, 250, 300, 873, 1073	a/b,d
	$\rightarrow O + O(^1D)$			
O_3	$\rightarrow O_2 + O$	900	···	a/Matsumi(2002)
	$\rightarrow O2 + O(^1D)$			
HO_2	$\rightarrow O + OH$	275	···	a/a
H_2O_2	$\rightarrow OH + OH$	350	···	a/a
HNCO	$\rightarrow NH + CO$	354	···	b/b
	$\rightarrow H + NCO$			
SH	$\rightarrow S + H$	345	300, 500, 750, 1000, 1250, 1500, 1750, 2000, 2250, 2500, 3000	a, Gorman et al. (2019) for $\lambda \geqslant 314$ nm/a
H_2S	$\rightarrow SH + H$	238	423, 573, 773	a, e/a

Table A1
(Continued)

Photolysis	Reaction	Threshold (nm)	Temp. Dependence (K)	Reference Cross Sections/Quantum Yields (λ in nm)
SO	$\rightarrow S + O$	235	⋯	a/a
SO_2	$\rightarrow SO + O$	220	⋯	a/a
	$\rightarrow S + O_2$		⋯	a/a
S_2	$\rightarrow S + S$	283	⋯	a/a
S_4	$\rightarrow S + S$	575	⋯	a/a
OCS	$\rightarrow CO + S$	280	⋯	a/a
CS	$\rightarrow C + S$	160	⋯	a/a
CS_2	$\rightarrow CS + S$	278	300, 423, 573, 773	a/a
CH_3SH	$\rightarrow CH3S + H$	310	⋯	a/b
	$\rightarrow CH3 + SH$			

Note. a: Leiden Observatory database http://home.strw.leidenuniv.nl/~ewine/photo (Heays et al. 2017); b: PHIDRATES database http://phidrates.space.swri.edu (Huebner et al. 1992); c: MPI-Mainz UV/VIS Spectral Atlas http://satellite.mpic.de/spectral_atlas/index.html (Keller-Rudek et al. 2013); d: Sander et al. (2015); e: ExoMol database http://www.exomol.com/data/data-types/xsec_VUV.

Appendix B
Resolution Errors of Photolysis Rates

Equation (11) is numerically computed in the form of finite sum. The wavelength grid in the code needs to properly resolve the line structures in the stellar flux and cross sections. This is especially important in the XUV, where there are more fine structures from the band transition (Rimmer & Helling 2016).

We demonstrate the errors of computing Equation (11) with the GJ 436b model in Section 4.3. The effects are emphasized with its host M star showing more emission lines. Figure 39 shows the stellar flux overplotted with the UV cross sections of H_2 and H_2O. The stellar flux is adopted from the MUSCLES survey with a constant 0.1 nm resolution, and the UV cross sections from the Lieden database have the same resolution of 0.1 nm. Therefore, we consider constant resolution of 0.1 nm as the reference for this test. The resolution for computing Equation (11) is varied from 0.2 to 10 nm, where the trapezoidal rule is applied for the integral. The errors with respect to summing up the total stellar flux and the resultant photolysis rate of H_2 and H_2O at the top of atmosphere (10^{-8} bar) are summarized in Table B1. Starting from the bin size of 0.5 nm, which is five times the native resolution of the flux and cross-section data, the errors become comparable to the absolute value of the photolysis rate. The errors do not behave linearly with the bin size since the overestimate from the peak can offset the underestimate from the trough. The test shows the importance of using matching spectral resolution to attain accurate photolysis rates.

Table B1
Errors from Low Spectral Resolution

Bin (nm)	Stellar Flux (in %)	ΔJ_{H_2} [a]	ΔJ_{H_2O}
0.2	0	0.0004	0.003
0.5	0.08	0.18	1.13
1	0.08	0.44	0.87
10	2.65	0.22	0.87

Note.
[a] $\Delta J = |J - J_0|/J_0$, where J_0 is the reference photolysis rate calculated with constant 0.1 nm resolution.

Appendix C
The Choice of Zenith Angle

A global or hemispheric average one-dimensional photochemical model requires specifying an effective zenith angle ($\bar{\theta}$) of the stellar beam to represent the planetary-mean actinic flux. The zenith angle of 48°–60° has been used for the hemispheric average in various photochemical models (e.g., Moses et al. 2011; Hu et al. 2012). For instance, a common choice in radiative transfer calculation is to take the flux-weighted cosine of the zenith angle (Cronin 2014):

$$\overline{\mu_{\rm I}} = \frac{\int_0^{2\pi}\int_0^1 \mu F_0 \mu d\mu d\phi}{\int_0^{2\pi}\int_0^1 F_0 \mu d\mu d\phi}, \tag{C1}$$

where ϕ is the azimuth angle and F_0 is the stellar flux at the top of the atmosphere. Equation (C1) yields $\overline{\mu_{\rm I}} = 2/3$ or $\overline{\theta_{\rm I}} \approx 48°$. For photochemistry calculation, actinic-flux-weighted cosine should be considered, and Equation ((C1)) becomes

$$\overline{\mu_{\rm II}} = \frac{\int_0^1 \mu J_0 d\mu}{\int_0^1 J_0 d\mu}, \tag{C2}$$

where J_0 is the actinic flux at the top of the atmosphere (i.e., total intensity) and the azimuth term is dropped. Equation (C2) now yields $\overline{\mu_{\rm II}} = 1/2$ or $\overline{\theta_{\rm II}} = 60°$.

Hu et al. (2012) discuss this choice of mean zenith angle by further considering the optical depth of the level where the hemispheric average of the attenuated actinic flux is evaluated, e.g., the authors find that mean zenith angles of 57° and 48° correspond to optical depths 0.1 and 1, respectively. We will revisit the discussion of Hu et al. (2012), but with a different approach here.

Instead of taking the average of μ, we consider an effective zenith angle such that the resulting mean actinic flux matches

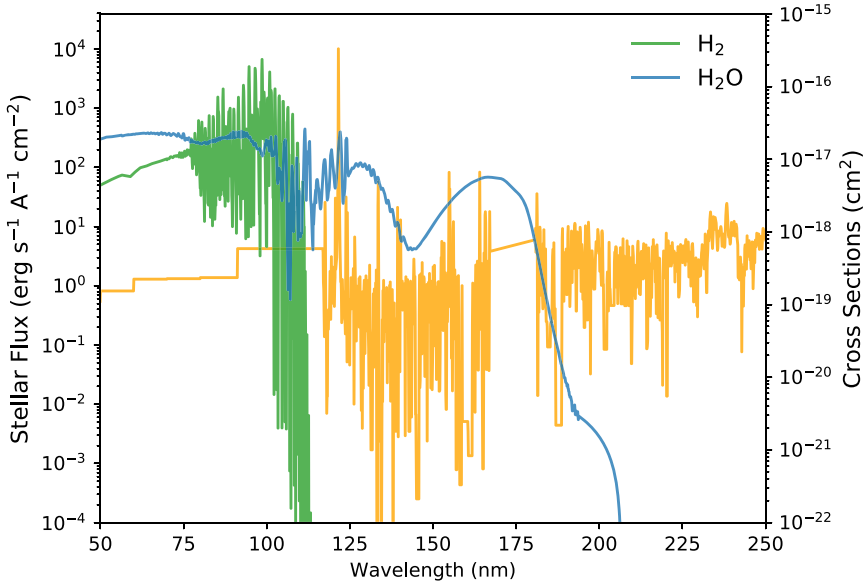

Figure 39. The stellar UV flux of GJ 436 and cross sections of H_2 and H_2O, showing the native resolution of 0.1 nm adopted in the model.

Table B2
List of Forward Reactions (Backward Reactions with Even Indexes Are Reversed Numerically with Thermodynamic Data) and Rate Coefficients ($cm^3\ s^{-1}$ for Bimolecular Reactions and s^{-1} for k_0) of Titanium and Vanadium Species

Reaction	Rate Coefficient	Reference
$TiO + O \rightarrow Ti + O_2$	$5.42 \times 10^{-13} \exp(-20794/T)$	E_a est. with A[5] from matching NIST 1994LIA/MIT (at room temperature)
$TiO + N \rightarrow Ti + NO$	$4.76 \times 10^{-12} \exp(-4772/T)$	E_a est. with A from matching NIST1993CLE/HON (at room temperature)
$TiO + N_2 \rightarrow Ti + N_2O$	$5.9 \times 10^{-12} \exp(-62193/T)$	E_a est. with A from matching NIST 1994LIA/MIT (at room temperature)
$TiO + H \rightarrow Ti + OH$	$2.0 \times 10^{-10} \exp(-28418/T)$	E_a est. with A based on $FeO + H \rightarrow Fe + OH$ from Rumminger et al. (1999)
$TiO + H_2 \rightarrow Ti + H_2O$	$2.0 \times 10^{-11} \exp(-21270/T)$	E_a est. with A based on $FeO + H_2 \rightarrow Fe + OH$ from Decin et al. (2018)
$Ti + CO_2 \rightarrow TiO + CO$	$7.01 \times 10^{-11} \exp(-1790/T)$	NIST 1993CAM/MCC7942-7946
$TiO_2 + H \rightarrow TiO + OH$	$1.0 \times 10^{-10} \exp(-19500/T)$	E_a est. with A based on $FeO_2 + H \rightarrow FeO + OH$ from Rumminger et al. (1999)
$TiO_2 + O \rightarrow TiO + O_2$	$1.0 \times 10^{-10} \exp(-11877/T)$	E_a est.
$TiO_2 + CO \rightarrow TiO + CO_2$	$1.0 \times 10^{-10} \exp(-9160/T)$	E_a est. with A based on $FeO_2 + O \rightarrow FeO + O_2$ from Rumminger et al. (1999)
$TiH + H \rightarrow Ti + H_2$	8.3×10^{-11}	Est. from $FeH + H \rightarrow Fe + H_2$ (Rumminger et al. 1999)
$TiH + O \rightarrow Ti + OH$	1.66×10^{-10}	Est. from $FeH + O \rightarrow Fe + OH$ (Rumminger et al. 1999)
$TiH + CH_3 \rightarrow Ti + CH_4$	1.0×10^{-10}	Est. from $FeH + CH3 \rightarrow Fe + CH_4$ (Rumminger et al. 1999)
$TiC + H \rightarrow Ti + CH$	$1.0 \times 10^{-10} \exp(-20109/T)$	E_a est.
$Ti + CO \rightarrow TiC + O$	$8.0 \times 10^{-10} \exp(-68842/T)$	E_a est.
$Ti + CN \rightarrow TiC + N$	$5.0 \times 10^{-10} \exp(-29543/T)$	$E_a$est.
$Ti + NO \rightarrow TiN + O$	$5.0 \times 10^{-11} \exp(-19706/T)$	E_a est. with A from matching Campbell & McClean 1993
$TiN + H \rightarrow Ti + NH$	$10^{-10} \exp(-15655/T)$	E_a est.
$VO + O \rightarrow V + O_2$	$6.19 \times 10^{-12} \exp(-14763/T)$	E_a est. with A from matching NIST 1990RIT/WEI (at room temperature)
$V + N_2O \rightarrow VO + N_2$	$4.7 \times 10^{-11} \exp(-1299/T)$	NIST 2000CAM/KOL
$VO + H \rightarrow V + OH$	$1.66 \times 10^{-10} \exp(-22386/T)$	E_a est. with A based on $FeO + H \rightarrow Fe + OH$ from Rumminger et al. (1999)
$VO + H_2 \rightarrow V + H_2O$	$1.0 \times 10^{-11} \exp(-15239/T)$	E_a est. with A based on $FeO + H_2 \rightarrow Fe + H2O$ from Decin et al. (2018)
$TiO_2 \overset{M}{\rightarrow} Ti + O_2$	$k_0 = 1.38 \times T^{-1.8} \exp(-94079/T)\ k_\infty = 2 \times 10^{17}\ T^{-0.91} \exp(-94079/T)$	E_a est. A based on $FeO2 \overset{M}{\rightarrow} Fe + O_2$ from Rumminger et al. (1999)
$TiO \overset{M}{\rightarrow} Ti + O$	$k_0 = 1.38 \times T^{-1.8} \exp(-82202/T) k_\infty = 2 \times 10^{17}\ T^{-0.91} \exp(-76171/T)$	E_a est. A based on $FeO \overset{M}{\rightarrow} Fe + O$ from Rumminger et al. (1999)
$VO \overset{M}{\rightarrow} V + O$	$k_0 = 1.38 \times T^{-1.8} \exp(-76171/T) k_\infty = 2 \times 10^{17}\ T^{-0.91} \exp(-76171/T)$	E_a est. A based on $FeO \overset{M}{\rightarrow}] Fe + O$ from Rumminger et al. (1999)

Notes. E_a est. means that the activation energy is estimated by the enthalpy difference as described in Section 2.7.
[a] The pre-exponential factor.

the hemispheric-mean actinic flux, viz.,

$$J_0 \exp\left(-\frac{\tau}{\overline{\mu}}\right) = \frac{\int_0^1 J_0 \exp\left(-\frac{\tau}{\mu}\right) d\mu}{\int_0^1 d\mu} = J_0 \int_0^1 \exp\left(-\frac{\tau}{\mu}\right) d\mu. \quad \text{(C3)}$$

Equation (C3) can be evaluated numerically at the given optical depth, as illustrated in Figure 40. We find that optical depth unity (i.e., where UV photons are mostly utilized for photochemistry) corresponds to $\overline{\theta} \approx 58°$. Note that the evaluation in Hu et al. (2012) is similar to Equation (C3) but weighted by μ within the integral, which is effectively the mean stellar flux instead of the actinic flux. Evaluating Equation (C3) at $\tau = 1$, we find $\overline{\theta} \approx 58°$ for a dayside-average model. For a terminator-average model, the denominator in Equation (C3) is integrated from -1 to 1 and we have $\overline{\theta} \approx 67°$.

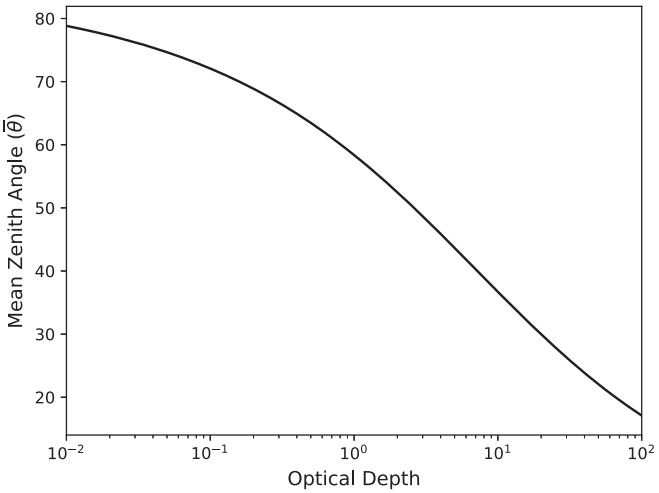

Figure 40. Dayside mean zenith angle for photochemical calculation as a function of optical depth from Equation (C3).

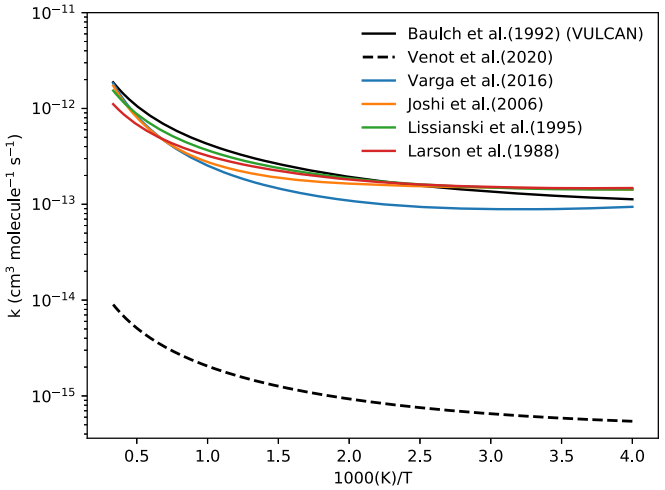

Figure 41. Comparisons of selective rate constants of Reaction (19): CO + OH → CO2 + H, with wide temperature ranges available on NIST.

ORCID iDs

Shang-Min Tsai https://orcid.org/0000-0002-8163-4608
Matej Malik https://orcid.org/0000-0002-2110-6694
Daniel Kitzmann https://orcid.org/0000-0003-4269-3311
Alexander Fateev https://orcid.org/0000-0003-2863-2707
Elspeth Lee https://orcid.org/0000-0002-3052-7116
Kevin Heng https://orcid.org/0000-0003-1907-5910

References

Agúndez, M., Venot, O., Selsis, F., & Iro, N. 2014, ApJ, 781, 68
Allen, M., Yung, Y. L., & Waters, J. W. 1981, JGRA, 86, 3617
Arney, G. N. 2019, ApJL, 873, L7
Atkinson, D. H., Ingersoll, A. P., & Seiff, A. 1997, Natur, 388, 649
Atreya, S. K., Hofstadter, M. H., In, J. H., et al. 2020, SSRv, 216, 18
Atreya, S. K., Wong, A. S., Baines, K. H., Wong, M. H., & Owen, T. C. 2005, P&SS, 53, 498
Ayres, T. R. 2010, ApJS, 187, 149
Banks, P. M., & Kockarts, G. 1973, Aeronomy (New York: Academic Press), 32
Barkley, M. P., Palmer, P. I., Boone, C. D., Bernath, P. F., & Suntharalingam, P. 2008, GeoRLIn, 35, L14810
Baxter, C., Désert, J.-M., Tsai, S.-M., et al. 2021, A&A, 648, A127
Birkby, J. L., de Kok, R. J., Brogi, M., et al. 2013, MNRAS: Letters, 436, L35
Boechat-Roberty, H. M., Rocco, M. L. M., Lucas, C. A., & de Souza, G. G. B. 2004, JPhB, 37, 1467
Bohlin, R. C., Mészáros, S., Fleming, S. W., et al. 2017, AJ, 153, 234
Bolton, S. J., Adriani, A., Adumitroaie, V., et al. 2017, Sci, 356, 821
Bordwell, B., Brown, B. P., & Oishi, J. S. 2018, ApJ, 854, 8
Bourrier, V., Wheatley, P. J., Lecavelier des Etangs, A., et al. 2020, MNRAS, 493, 559
Brasseur, G. P., & Jacob, D. J. 2017, Numerical Methods for Advection (Cambridge: Cambridge Univ. Press), 275
Brogi, M., de Kok, R. J., Birkby, J. L., Schwarz, H., & Snellen, I. A. G. 2014, A&A, 565, A124
Burke, U., Metcalfe, W. K., Burke, S. M., et al. 2016, CoFl, 165, 125
Burrows, A., Dulick, M., Bauschlicher, C. W., et al. 2005, ApJ, 624, 988
Butler, R. P., Vogt, S. S., Marcy, G. W., et al. 2004, ApJ, 617, 580
Campbell, M. L., & McClean, R. E. 1993, JPhCh, 97, 7942
Capalbo, F. J., Bénilan, Y., Fray, N., et al. 2016, Icar, 265, 95
Chachan, Y., Knutson, H. A., Gao, P., et al. 2019, AJ, 158, 244
Chamberlain, J. W., & Hunten, D. M. 1987, in Int. Geophysics, Theory of Planetary Atmospheres, ed. J. W. Chamberlain & D. M. Hunten, Vol. 36 (New York: Academic Press), 330
Charnay, B., Meadows, V., & Leconte, J. 2015, ApJ, 813, 15
Chauvin, G. 2018, arXiv:1810.02031
Chestakov, D. A., Parker, D. H., & Baklanov, A. V. 2005, JChPh, 122, 084302
Chiou, E. W., McCormick, M. P., & Chu, W. P. 1997, JGRD, 102, 19105
Cloutman, L. 2000, Lawrence Livermore National Laboratory report, UCRL-ID-139893
Cronin, T. W. 2014, J. Atmos. Sci., 71, 2994
Crossfield, I. J. M. 2015, PASP, 127, 941
Davidson, D. F., Chang, A. Y., & Hanson, R. K. 1989, Symp. (Int.) on Combustion, 22, 1877
De Rosa, R. J., Nielsen, E. L., Wang, J. J., et al. 2020, AJ, 159, 1
Dean, A. M., & Bozzelli, J. W. 2000, Combustion Chemistry of Nitrogen (Berlin: Springer), 125
Dean, A. M., Chou, M.-S., & Stern, D. 1984, Int. J. of Chem. Kinetics, 16, 633
Decin, L., Danilovich, T., Gobrecht, D., et al. 2018, ApJ, 855, 113
Demory, B. O., Gillon, M., Barman, T., et al. 2007, A&A, 475, 1125
Drossart, P., Fouchet, T., Crovisier, J., et al. 1999, in ESA Special Publication, The Universe as Seen by ISO, 427 ed. P. Cox & M. Kessler, 169
Drummond, B., Tremblin, P., Baraffe, I., et al. 2016, A&A, 594, A69
Du, S., Francisco, J. S., Shepler, B. C., & Peterson, K. A. 2008, JChPh, 128, 204306
Ehhalt, D. H., & Heidt, L. E. 1973, JGR, 78, 5265
Fair, R. W., & Thrush, B. A. 1969, Trans. Faraday Soc, 65, 1208
Fischer, H., Birk, M., Blom, C., et al. 2008, ACP, 8, 2151
Fortney, J., Lodders, K., Marley, M., & Freedman, R. 2008, ApJ, 678, 1419
France, K., Loyd, R. O. P., Youngblood, A., et al. 2016, ApJ, 820, 89
Frederick, J. E., & Mentall, J. E. 1982, GeoRL, 9, 461
Frenklach, M. 2002, PCCP, 4, 2028
Frenklach, M., & Mebel, A. M. 2020, PCCP, 22, 5314
Funke, B., López-Puertas, M., García-Comas, M., et al. 2009, ACP, 9, 2387
Gans, B., Boyé-Péronne, S., Broquier, M., et al. 2011, PCCP, 13, 8140
Gao, P., & Benneke, B. 2018, ApJ, 863, 165
Gao, P., Marley, M. S., Zahnle, K., Robinson, T. D., & Lewis, N. K. 2017, AJ, 153, 139
Gao, P., Thorngren, D. P., Lee, G. K. H., et al. 2020, NatAs, 4, 951
Georgii, H.-W., & Meixner, F. X. 1980, JGRC, 85, 7433
Gersen, S., van Essen, M., Darmeveil, H., et al. 2017, Energy and Fuels, 31, 2175
Giacobbe, P., Brogi, M., Gandhi, S., et al. 2021, Natur, 592, 205
Gorman, M. N., Yurchenko, S. N., & Tennyson, J. 2019, MNRAS, 490, 1652
Gueymard, C. A. 2018, SoEn, 169, 434
Hagege, J., Roberge, P. C., & Vermeil, C. 1968, Trans. Faraday Soc., 64, 3288
Hauglustaine, D. A., Granier, C., Brasseur, G. P., & MéGie, G. 1994, JGR, 99, 1173
He, C., Hörst, S. M., Lewis, N. K., et al. 2020a, NatAs, 4, 986
He, C., Hörst, S. M., Lewis, N. K., et al. 2020b, PSJ, 1, 51
Heays, A. N., Bosman, A. D., & van Dishoeck, E. F. 2017, A&A, 602, A105
Helling, C., & Woitke, P. 2006, A&A, 455, 325
Heng, K., Malik, M., & Kitzmann, D. 2018, ApJS, 237, 29
Hidaka, Y., Oki, T., Kawano, H., & Higashihara, T. 1989, JPhCh, 93, 20
Hobbs, R., Rimmer, P. B., Shorttle, O., & Madhusudhan, N. 2021, MNRAS, 506, 3186
Hobbs, R., Shorttle, O., Madhusudhan, N., & Rimmer, P. 2019, MNRAS, 487, 2242
Hoeijmakers, H. J., Ehrenreich, D., Heng, K., et al. 2018, Natur, 560, 453
Höpfner, M., Volkamer, R., Grabowski, U., et al. 2016, ACP, 16, 14357
Hu, R., Seager, S., & Bains, W. 2012, ApJ, 761, 166
Hu, R., Seager, S., & Bains, W. 2013, ApJ, 769, 6
Hu, R., Seager, S., & Yung, Y. L. 2015, ApJ, 807, 8
Hubeny, I., Burrows, A., & Sudarsky, D. 2003, ApJ, 594, 1011
Hudson, R. D., & Reed, E. I. 1979, The Stratosphere: Present and Future, Technical Report 1049, NASA
Hue, V., Cavalié, T., Dobrijevic, M., Hersant, F., & Greathouse, T. 2015, Icar, 257, 163
Hue, V., Hersant, F., Cavalié, T., Dobrijevic, M., & Sinclair, J. A. 2018, Icar, 307, 106
Huebner, W., & Mukherjee, J. 2015, P&SS, 106, 11
Huebner, W. F., Keady, J. J., & Lyon, S. P. 1992, Ap&SS, 195, 1
Hunter, J. D. 2007, CSE, 9, 90
Inn, E. C. Y., Vedder, J. F., Tyson, B. J., & O'Hara, D. 1979, GeoRL, 6, 191
Jacob, D. J. 2011, Introduction to Atmospheric Chemistry (Princeton, NJ: Princeton Univ. Press)
Joshi, A. V., & Wang, H. 2006, Int. Journal of Chemical Kinetics, 38, 57
Kassner, C., & Stuhl, F. 1994, CPL, 222, 425
Kasting, J. F., & Donahue, T. M. 1980, JGRC, 85, 3255
Kasting, J. F., Liu, S. C., & Donahue, T. M. 1979, JGRC, 84, 3097
Kawashima, Y., & Ikoma, M. 2018, ApJ, 853, 7
Kawashima, Y., & Ikoma, M. 2019, ApJ, 877, 109
Keller-Rudek, H., Moortgat, G. K., Sander, R., & Sörensen, R. 2013, ESSD, 5, 365

Khodachenko, M. L., Shaikhislamov, I. F., Lammer, H., et al. 2019, ApJ, 885, 67
Kislov, V. V., Nguyen, T. L., Mebel, A. M., Lin, S. H., & Smith, S. C. 2004, JChPh, 120, 7008
Kitzmann, D., Heng, K., Rimmer, P. B., et al. 2018, ApJ, 863, 183
Klippenstein, S. J., Harding, L. B., Ruscic, B., et al. 2009, JPCA, 113, 10241
Knutson, H. A., Benneke, B., Deming, D., & Homeier, D. 2014, Natur, 505, 66
Knutson, H. A., Madhusudhan, N., Cowan, N. B., et al. 2011, ApJ, 735, 27
Komacek, T. D., Showman, A. P., & Parmentier, V. 2019, ApJ, 881, 152
Konnov, A., & De Ruyck, J. 2001, CoFl, 124, 106
Krasnopolsky, V. A. 2009, Icar, 201, 226
Krasnopolsky, V. A. 2012, Icar, 218, 230
Krasnopolsky, V. A. 2013, Icar, 225, 570
Kreidberg, L. 2018, in Exoplanet Atmosphere Measurements from Transmission Spectroscopy and Other Planet Star Combined Light Observations, ed. H. J. Deeg & J. A. Belmonte (New York: Springer International), 100
Kreidberg, L., Bean, J. L., Désert, J.-M., et al. 2014, Natur, 505, 69
Lanotte, A. A., Gillon, M., Demory, B. O., et al. 2014, A&A, 572, A73
Lavvas, P., & Koskinen, T. 2017, ApJ, 847, 32
Lavvas, P., Yelle, R. V., Koskinen, T., et al. 2013, PNAS, 110, 2729
Lavvas, P. P., Coustenis, A., & Vardavas, I. M. 2008, P&SS, 56, 27
Lebonnois, S. 2005, P&SS, 53, 486
Lewis, N. K., Showman, A. P., Fortney, J. J., et al. 2010, ApJ, 720, 344
Lewis, N. K., Wakeford, H. R., MacDonald, R. J., et al. 2020, ApJL, 902, L19
Li, C., Ingersoll, A., Bolton, S., et al. 2020, NatAs, 4, 609
Li, C., Ingersoll, A., Janssen, M., et al. 2017, GeoRL, 44, 5317
Li, Q., Jacob, D. J., Yantosca, R. M., et al. 2003, JGRD, 108, 8827
Liang, M.-C., Parkinson, C. D., Lee, A. Y.-T., Yung, Y. L., & Seager, S. 2003, ApJL, 596, L247
Lias, S. G., Collin, G. J., Rebbert, R. E., & Ausloos, P. 1970, JChPh, 52, 1841
Lincowski, A. P., Meadows, V. S., Crisp, D., et al. 2018, ApJ, 867, 76
Lindzen, R. S. 1981, JGRC, 86, 9707
Line, M. R., Liang, M. C., & Yung, Y. L. 2010, ApJ, 717, 496
Loftus, K., Wordsworth, R. D., & Morley, C. V. 2019, ApJ, 887, 231
Lothringer, J. D., Benneke, B., Crossfield, I. J. M., et al. 2018, AJ, 155, 66
Loyd, R. O. P., France, K., Youngblood, A., et al. 2016, ApJ, 824, 102
Lyons, J. R. 2008, J. Sulfur Chem., 29, 269
Macintosh, B., Graham, J. R., Barman, T., et al. 2015, Sci, 350, 64
Madhusudhan, N. 2012, ApJ, 758, 36
Madhusudhan, N., & Seager, S. 2011, ApJ, 729, 41
Malik, M., Kitzmann, D., Mendonça, J. M., et al. 2019, AJ, 157, 170
Marrero, T. R., & Mason, E. A. 1972, JPCRD, 1, 3
Massie, S. T., & Hunten, D. M. 1981, JGR, 86, 9859
McCullough, P. R., Crouzet, N., Deming, D., & Madhusudhan, N. 2014, ApJ, 791, 55
Miguel, Y., & Kaltenegger, L. 2014, ApJ, 780, 166
Misra, A., Krissansen-Totton, J., Koehler, M. C., & Sholes, S. 2015, AsBio, 15, 462
Molaverdikhani, K., Henning, T., & Mollière, P. 2019, ApJ, 883, 194
Morello, G., Waldmann, I. P., Tinetti, G., et al. 2015, ApJ, 802, 117
Morley, C. V., Fortney, J. J., Kempton, E. M.-R., et al. 2013, ApJ, 775, 33
Morley, C. V., Knutson, H., Line, M., et al. 2017, AJ, 153, 86
Moses, J. 2014, RSPTA, 372, 20130073
Moses, J. I., Bruno, B., Lellouch, E., & Allen, M. 2000, Icar, 143, 244
Moses, J. I., Fouchet, T., Bézard, B., et al. 2005, JGRE, 110, E08001
Moses, J. I., Line, M. R., Visscher, C., et al. 2013, ApJ, 777, 34
Moses, J. I., Marley, M. S., Zahnle, K., et al. 2016, ApJ, 829, 66
Moses, J. I., Visscher, C., Fortney, J. J., et al. 2011, ApJ, 737, 15
Nair, H., Allen, M., Anbar, A., Yung, Y., & Clancy, R. 1994, Icar, 111, 124
Nicholas, J. E., Amodio, C. A., & Baker, M. J. 1979, J. Chem. Soc., Faraday Trans, 1, 1868
Nicolet, M. 1968, GeoJI, 15, 157
Noël, S., Weigel, K., Bramstedt, K., et al. 2018, ACP, 18, 4463
Nuth, J. A., & Glicker, S. 1982, JQSRT, 28, 223
Ohno, K., Okuzumi, S., & Tazaki, R. 2020, ApJ, 891, 131
Okabe, H. 1983, JChPh, 78, 1312
Oliphant, T. E. 2007, CSE, 9, 10
Oya, M., Shiina, H., Tsuchiya, K., & Matsui, H. 1994, BCSJ, 67, 2311
Parmentier, V., Line, M. R., Bean, J. L., et al. 2018, A&A, 617, A110
Parmentier, V., Showman, A. P., & Lian, Y. 2013, A&A, 558, A91
Parviainen, H., Pallé, E., Chen, G., et al. 2018, A&A, 609, A33
Pearce, B. K. D., Ayers, P. W., & Pudritz, R. E. 2019, JPCA, 123, 1861
Pinto, J. P., Li, J., Mills, F. P., et al. 2021, NatCo, 12, 175
Plessis, S., Carrasco, N., Dobrijevic, M., & Pernot, P. 2012, Icar, 219, 254
Pont, F., Sing, D. K., Gibson, N. P., et al. 2013, MNRAS, 432, 2917
Pueyo, L. 2018, in Direct Imaging as a Detection Technique for Exoplanets, ed. H. J. Deeg & J. A. Belmonte (Cham: Springer Int. Publishing), 1
Ranjan, S., Schwieterman, E. W., Harman, C., et al. 2020, ApJ, 896, 148
Rees, D. 1988, AdSpR, 333, 523
Rees, D., Barnett, J. J., & Labitzke, K. 1990, AdSpR, 10, 12
Rimmer, P. B., & Helling, C. 2016, ApJS, 224, 9
Rimmer, P. B., & Rugheimer, S. 2019, Icar, 329, 124
Rugheimer, S., Kaltenegger, L., Zsom, A., Segura, A., & Sasselov, D. 2013, AsBio, 13, 251
Rumminger, M. D., Reinelt, D., Babushok, V., & Linteris, G. T. 1999, Combust. Flame, 116, 207
Samland, M., Mollière, P., Bonnefoy, M., et al. 2017, A&A, 603, A57
Sander, S. P., Friedl, R. R., Abbatt, D. J. P., et al. 2015, JPL Publication, 15-10, 27
Sanz-Forcada, J., Micela, G., Ribas, I., et al. 2011, A&A, 532, A6
Schulz, C., Koch, J., Davidson, D., Jeffries, J., & Hanson, R. 2002, CPL, 355, 82
Schwieterman, E. W., Kiang, N. Y., Parenteau, M. N., et al. 2018, AsBio, 18, 663
Seinfeld, J. H., & Pandis, S. N. 2016, Atmospheric Chemistry and Physics: From Air Pollution to Climate Change (Hoboken, NJ: John Wiley & Sons)
Serindag, D. B., Nugroho, S. K., Mollière, P., et al. 2021, A&A, 645, A90
Shulyak, D., Lara, L. M., Rengel, M., & Nèmec, N. E. 2020, A&A, 639, A48
Slanger, T. G., & Black, G. 1982, JChPh, 77, 2432
Smith, M. D. 1998, Icar, 132, 176
Smithson, P. A. 2001, IJCli, 22, 1144
Stevenson, D. J. 2020, AREPS, 48, 465
Stevenson, K. B., Harrington, J., Nymeyer, S., et al. 2010, Natur, 464, 1161
Stief, L. J., Payne, W. A., & Klemm, R. B. 1975, JChPh, 62, 4000
Suto, M., Wang, X., Shan, J., & Lee, L. 1992, JQSRT, 48, 79
Tan, X., & Komacek, T. D. 2019, ApJ, 886, 26
Tsai, S.-M., Kitzmann, D., Lyons, J. R., et al. 2018, ApJ, 862, 31
Tsai, S.-M., Lyons, J. R., Grosheintz, L., et al. 2017, ApJS, 228, 1
Tsang, W., & Hampson, R. F. 1986, JPCRD, 15, 1087
Tsuji, T. 1973, A&A, 23, 411
van der Walt, S., Colbert, S. C., & Varoquaux, G. 2011, CSE, 13, 22
Vattulainen, J., Wallenius, L., Stenberg, J., Hernberg, R., & Linna, V. 1997, ApSpe, 51, 1311
Venot, H., Eric, A., Marcelino, D., & Leen, B. R. 2015, A&A, 577, A33
Venot, O., Bénilan, Y., Fray, N., et al. 2018, A&A, 609, A34
Venot, O., Bounaceur, R., Dobrijevic, M., et al. 2019, A&A, 624, A58
Venot, O., Cavalié, T., Bounaceur, R., et al. 2020, A&A, 634, A78
Venot, O., Fray, N., Bénilan, Y., et al. 2013, A&A, 551, A131
Venot, O., Hébrard, E., Agúndez, M., et al. 2012, A&A, 546, A43
Visscher, C., Moses, J. I., & Saslow, S. A. 2010, Icar, 209, 602
Voigt, S., Orphal, J., & Burrows, J. 2002, J. Photochem. Photobiol. A: Chem., 149, 1
von Essen, C., Mallonn, M., Borre, C. C., et al. 2020, A&A, 639, A34
Wakeford, H. R., Sing, D. K., Kataria, T., et al. 2017, Sci, 356, 628
Wang, D., Lunine, J. I., & Mousis, O. 2016, Icar, 276, 21
Wang, H. 2011, Proc. of the Combustion Institute, 33, 41
Weidenschilling, S. J., & Lewis, J. S. 1973, Icar, 20, 465
Wilson, E. H., & Atreya, S. K. 2004, JGRA, 109, E06002
Woitke, P., Helling, C., Hunter, G. H., et al. 2018, A&A, 614, A1
Wong, A. S., Yung, Y. L., & Friedson, A. J. 2003, GeoRL, 30, 2001
Wordsworth, R. D., Schaefer, L. K., & Fischer, R. A. 2018, AJ, 155, 195
Youngblood, A., France, K., Loyd, R. O. P., et al. 2016, ApJ, 824, 101
Yung, Y. L., Allen, M., & Pinto, J. P. 1984, ApJS, 55, 465
Yung, Y. L., & DeMore, W. B. 1999, Photochemistry of Planetary Atmospheres (Oxford: Oxford Univ. Press)
Yung, Y. L., & Strobel, D. F. 1980, ApJ, 239, 395
Zahnle, K., Marley, M. S., Freedman, R. S., Lodders, K., & Fortney, J. J. 2009, ApJL, 701, L20
Zahnle, K., Marley, M. S., Morley, C. V., & Moses, J. I. 2016, ApJ, 824, 137
Zhang, M., Chachan, Y., Kempton, E. M. R., & Knutson, H. A. 2019, PASP, 131, 034501
Zhang, M., Chachan, Y., Kempton, E. M. R., Knutson, H. A., & Chang, W. H. 2020, ApJ, 899, 27
Zhang, M., Knutson, H. A., Kataria, T., et al. 2018, AJ, 155, 83
Zhang, X., Liang, M. C., Mills, F. P., Belyaev, D. A., & Yung, Y. L. 2012, Icar, 217, 714
Zhang, X., Shia, R.-L., & Yung, Y. L. 2013, ApJ, 767, 172
Zhao, L., Kaiser, R. I., Xu, B., et al. 2018, NatAs, 2, 973
Zilinskas, M., Miguel, Y., Mollière, P., & Tsai, S.-M. 2020, MNRAS, 494, 1490
Zuev, A. P., & Starikovskii, A. Y. 1990, JApSp, 52, 304